Controlling dust charge in complex plasmas

by

Michael McKinlay

A dissertation submitted to the Graduate Faculty of
Auburn University
in partial fulfillment of the
requirements for the Degree of
Doctor of Philosophy

Auburn, Alabama
August 6, 2022

Keywords: dust, plasma, charging, physics, laboratory, experimental

Approved by

Dr. Edward Thomas Jr., Chair, Interim Dean and Professor of Physics
Dr. Mike Fogle Jr. Associate Professor of Physics
Dr. Dennis Bodewits, Associate Professor of Physics
Dr. Saikat Chakraborty Thakur, Assistant Professor of Physics
Dr. Christopher Grieco, Assistant Professor of Chemistry and Biochemistry

Abstract

A dusty plasma is a four-component plasma consisting of electrons, ions, neutral gas, and microparticles (dust) which collect charge from the surrounding plasma environment. They can be found in every regime of plasma physics - from ice in planetary rings to eroded materials in fusion devices. Academics view dust as a potential tool; the coupling between the equilibrium properties of the dust and the properties of the background plasma gives isolated particles potential as a minimally-perturbative plasma diagnostic, while the ability to measure individual and collective particle behavior through direct observation instead of instrumental inference makes them extremely appealing as an analog for studying the behavior of soft-body systems or as a tool for investigating statistical mechanics. Conversely, most practical plasma applications view dust as a nuisance that needs to be avoided or removed. Both sets of interest are ultimately hindered by our lack of direct and independent control over the most fundamental property of the dust - the charge.

The research presented in this dissertation focuses on investigating and developing techniques to exert control over the equilibrium charge of dust suspended in a plasma, specifically whether it can be accomplished with minimal perturbation of the background plasma. The details and results of two experiments are presented: In the first, an electric field oscillating at a frequency greater than the dust response, but less than the ion-neutral collision rate is applied in an attempt to generate a net increase in ion collection. In the second, an ultraviolet (UV) source is used to generate photoelectric currents from the particles to shed excess negative charge. A computational project examining the role of particle geometry in photoelectric charging is also presented.

Acknowledgments

To the members of my committee, Dr. Mike Fogle Jr., Dr. Dennis Bodewits, and our University Reader, Dr. Christopher Grieco, thank you all so much for participating in this process. I would especially like to thank Dr. Saikat Chakraborty Thakur, for his invaluable feedback on the subject of nonlinear dynamics.

To the members of my graduate class, including Ben Schoenek, James Kring, Paul Sanders, and Omar Ortiz, and to the members of the MPRL team, past and present, especially Taylor Hall, Spencer LeBlanc, Brandon Doyle, and Lori McCabe, thank you all for your friendship and support over the years. I would also like to thank Dr. Uwe Konopka for his constant experimental and analytical insights; Darrick Artis for his incredible work as the MPRL engineering technician during my time at Auburn; and Dr. James Hanson for giving me the opportunity to push through my struggles at the start of my graduate career.

To Dr. Robert Merlino, thank you for introducing me to new worlds. You exposed me to a subject I had scarcely heard of, much less one I could have imagined would define the last decade of my life. You taught me to appreciate the challenge of investigation and to find joy in the pursuit. Thank you for setting me on this path.

To Dr. Edward Thomas, Jr., you have been a teacher, a mentor, and a constant source of inspiration. You helped me to keep focused and objective through some of the most challenging parts of my research, and helped me to persevere through some of the most challenging personal obstacles in my life. I cannot possibly thank you enough for everything you have been and done for me during my time at Auburn. I only hope I can live up to the example you have set for me.

To my dear friends, Tyler and Rebekah Kent, I cannot imagine making it through this experience without you guys in my life. You kept me sane and kept me grounded. Thank you so much for your friendship, your optimism, and your kindness.

Finally, and most importantly, to my family; my mother Michele, my father Mike, and my sisters Daisy and Lily; you guys have been my rock. Through every struggle and setback you have been there; encouraging me, believing in me, and helping me to keep going. Thank you for all of your love, support, and patience with me during this unexpected journey.

Table of Contents

List of Figures

List of Tables

List of Constants, Parameters, and Symbols

This list contains **some** of the more common abbreviations and physical parameters and constants that will appear in this dissertation.

Abbreviations

FPS	Frames Per Second
LTP	Low Temperature Plasma
MF	Melamine Formaldehyde (a common dust material)
OML	Orbital Motion-Limited Charging Model
PIV	Particle Image Velocimetry
PTV	Particle Tracking Velocimetry
SEM	Scanning Electron Microscope
UV	Ultraviolet

Constants

ϵ_0	Vacuum Permittivity
e	Electron Charge
k_B	Boltzmann Constant
m_e	Electron Mass

Parameters

I_{is}	Ion Saturation Current
M_{Ds}	Thermal drift Mach number
P_n	Neutral Pressure
Q_d	Dust charge
r_d	Dust radius
T_e	Electron Temperature
V_f	Floating Potential
V_s	Space/Plasma Potential
v_{ts}	Thermal velocity

Chapter 1

Introduction

1.1 What is a Dusty Plasma?

A dusty plasma, also sometimes referred to as a complex plasma, is a four-component plasma system which consists of electrons, ions, neutral gas, and charged particulate matter (dust). In a plasma environment, these particles collect charge from their surroundings and become a third, charged species coupled to the rest of the plasma. Dusty plasmas can be found in virtually every regime of plasma physics, and the dust particles themselves can range from the nanometer to micrometer scale and be composed of any number of materials: Laboratory-scale experiments may employ highly monodisperse microspheres comprised of silica or melamine formaldehyde (MF), charged ice crystals can be observed in planetary ring formations or near frozen moons (Horanyi 2004[11]; Morooka et al. 2011[25]; Shafiq et al. 2011[31]) or noctilucent clouds in the upper atmosphere, fusion devices can be contaminated by material ablated from shielding or other plasma-facing components (Winter 2000[45]; Brochard et al. 2016[2]; Rubel et al. 2018[28]), and particles sputtered by instrumentation or electrodes or grown in-situ from chemical reactions are frequently found in the industrial plasmas used for device fabrication (Watanabe 1997[44]; Kersten et al. 2003[18]; Shumova et al. 2019[34]) and plasma processing (the environments and scaling of these systems is elaborated on in Table 1.1).

What sets dusty plasmas apart from conventional plasma systems is the incredibly low charge-to-mass ratio of the dust particles. As shown in Table 1.2, the charge-to-mass ratio of dust particles is many orders of magnitude lower than that of the ions or electrons. This has the consequence of slowing the dynamics of the dust to a macroscopic scale; whereas electron response in a plasma is generally measured in nanoseconds, and the ion response

Examples of Dusty Plasmas		
Environment	**Type of Dust**	**Scale (m)**
Processing Plasmas	Contaminants	10^{-2} - 10^{-1}
Fusion Experiments	Ablated Shielding	10^{0} - 10^{1}
Upper Atmosphere	Noctilucent Clouds	10^{2} - 10^{4}
Interplanetary	Planetary Rings	10^{6} - 10^{8}
Interstellar	Dusty Nebulae	10^{12} - 10^{16}

Table 1.1: Examples of environments where dusty plasmas can be found, the nature of the dust, and the typical range of length scales of the systems. Dusty plasmas can be found on every scale and in every environment that we find plasmas in nature and in industry.

in microseconds, the dynamic timescale of dust particles in laboratory experiments is often measured in milliseconds or even seconds. This means that most of the physical phenomena that take place in a dusty plasma - like particle motion, collisions, and collective behavior - all occur on time and length scales that can be resolved with either the naked eye or a moderately high framerate camera ($\sim$100 FPS). Unlike conventional plasmas where all of the information we may be interested in knowing must be inferred 'second-hand' from instruments like plasma probes or spectrographic measurements, dusty plasmas present researchers with the unique opportunity to make measurements of important physical and statistical properties through direct observation of particle motion (Fisher 2010[5]). Particle Tracking Velocimetry (PTV) or Particle Image Velocimetry (PIV) (Lynch 2016[22] and Thomas 1999[38], respectively) can directly measure the kinematics of individual particles, the velocity distribution functions of dust clouds, the dispersion relations of density waves, or the pair-correlation functions of self-organized dust crystals.

1.2 Interest in Dusty Plasmas

Academic interest in dusty plasmas can be divided into three broad categories: the study of the unique physics of dusty plasmas and their occurrence in nature, the treatment of the dust as a diagnostic tool, and the use of the dust as an analog for studying the behavior of other systems. Examples of some of these can be seen in Figure 1.1.

Charge-to-Mass Ratios of Plasma Species*		
Species	Charge-to-Mass Ratio (C/kg)	Dynamic Response (Hz)
Electrons	$\sim 10^{11}$	$\sim 10^{7} - 10^{8}$
Ions	$\sim 10^{6}$	$\sim 10^{5} - 10^{6}$
Dust	$\sim 10^{-2} - 10^{1}$	$\sim 10^{0} - 10^{1}$
*For plasma conditions typical of the experiments discussed in this dissertation.		

Table 1.2: Approximate orders of magnitude of the charge-to-mass ratios and dynamic responses of the different charge species in a dusty plasma. The high mass of the dust when compared to the electrons or ions significantly slows its dynamic timescale. Most of the dynamics of the dust occur on macroscopic timescales and can be observed through direct observation.

The collection of electrons and ions from the background plasma by the dust as it moves or settles in the plasma can alter local plasma conditions - changing the charge density and electric fields of the background plasma. Coupling between the dust and the surrounding plasma environment can modify existing flows, circulation, and instabilities in the background plasma, and the collective behavior of the dust produces an entire class of dust waves. The coupled nature of the dust's charging process also means that the charge of dust particles is dependent on their location within the plasma and on the properties of the particles themselves.

This coupling between the dust and background plasma has led many experimenters to investigate the potential of utilizing isolated particles as a minimally perturbative diagnostic. The inherent dependence of the equilibrium and dynamic behavior of the dust on the background plasma profiles means researchers can examine the motion of the particles in the plasma to infer information about underlying potential structures, temperature gradients, density profiles, background flows, etc. Of course, inferring information about the plasma from the dust behavior necessitates a reliable and robust understanding of the charging mechanics.

The coupling strength between the dust particles is, itself, also a complex function of the properties of the background plasma and the properties of the dust. By varying dust and plasma conditions in laboratory experiments, experimenters can alter the strength of the

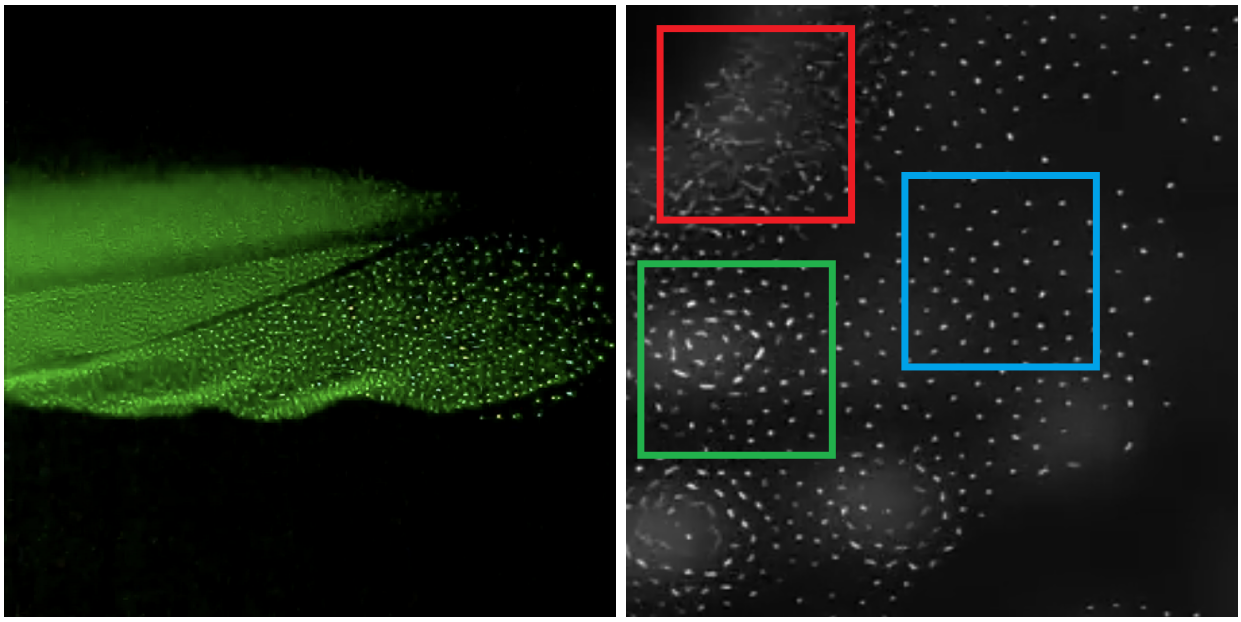

Figure 1.1: Coupling between the dust and the background plasma, and the collective behavior of the dust leads to unique phenomena like this Dust Acoustic Wave (*left*). The coupling strength of the dust can be adjusted by altering plasma conditions (*right*) to make the dust more gas-like (*red*), liquid-like (*green*), or solid-like (*blue*). Strongly-coupled particles can even self-organize into crystalline structures. (Source:MPRL)

coupling between particles to make the system behave more solid-like, liquid-like, or gas-like, or even transition between states. This, combined with the ease with which particle dynamics can be directly observed, makes dusty plasmas appealing to researchers as an analog for studying the mechanics of soft-body systems and the study of statistical mechanics. As previously mentioned - the ability to measure statistical parameters using PTV and PIV, like particle distribution functions, pair-correlation functions, and dispersion relations puts dusty plasmas in an especially advantageous position when it comes to studying statistical mechanics. Carefully designed dusty plasma experiments have used statistical analysis of dust to investigate the behavior of individual particles during phase transitions (Thomas & Morfill 1996[40]), measured the instantaneous entropy production rates of self-organized dust as a validation of statistical fluctuation theorems (Wong et al. 2017[46]), and looked at statistical mechanical descriptions of imposed ordered structures found in magnetized dusty plasmas (Hall et al. 2018[9]).

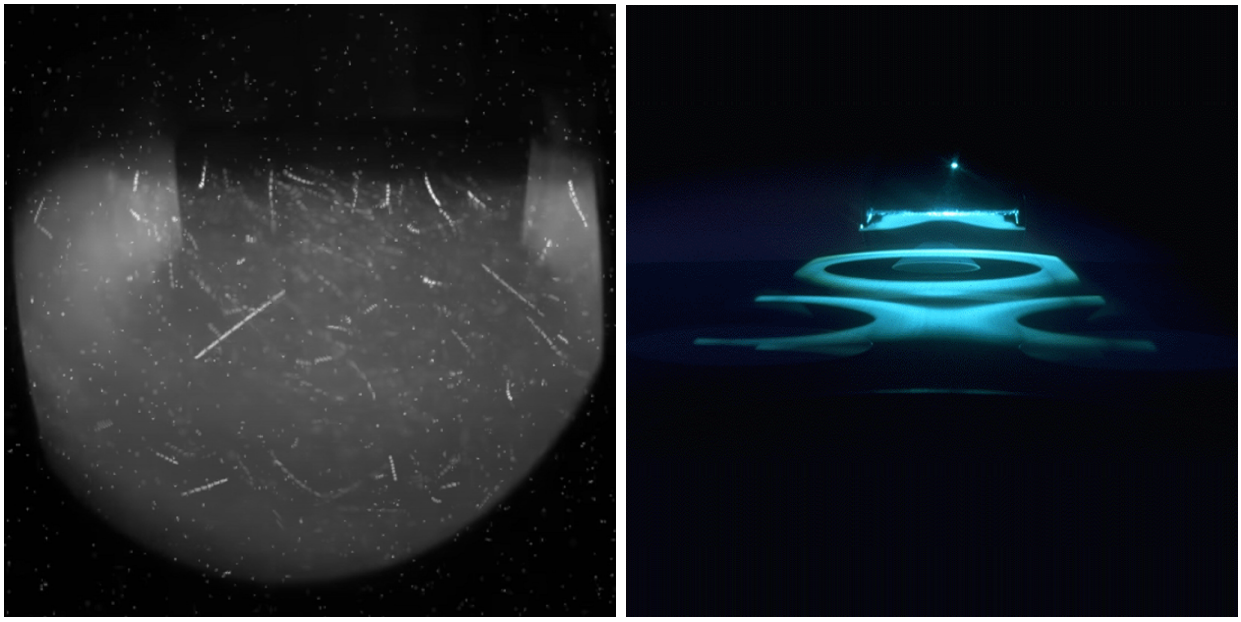

Figure 1.2: Dust produced by pellet injections (*left*) or the ablation and erosion of shielding and other plasma-facing components can disrupt and destabilize fusion plasmas (IPP 2020[6]). Dust can enter industrial plasmas (*right*) through external contamination, sputtering, or in-situ particle growth caused by chemical reactions. If left unchecked, particle deposition can pollute apparatuses and ruin fabricated devices (Selwyn 1994[30]).

Practical interest in dusty plasmas, on the other hand, generally views the dust almost exclusively as a nuisance - a contaminant that needs to be avoided or excised from environments. Some examples of contamination can be found in Figure 1.2. In fusion devices, loose particles generated by the ablation and erosion of plasma-facing components represent a potentially disruptive and dangerous element; if these particles find their way towards the core they can dilute the plasma, produce radioactive materials, or even damage the device. Dust is also a nuisance in low-temperature plasmas (LTPs): Particles produced through external contamination, sputtering, or in-situ growth of particles from chemical reactions in industrial devices can be devastating to plasma processing (Selwyn 1994[30]); dust particle deposition on vacuum chamber surfaces, electrodes, or probes can alter plasma conditions or impact the performance of diagnostics. For fabricated devices, which must often be accurate to the nanometer, even sub-micrometer dust particles becomes 'device-killers'. Even

in space, charged dust can be a potential hazard, adhering to and interfering with surface instruments and astronaut equipment.

1.3 The Trouble With Charge

What these academic and practical interests all have in common is that they all face the same frustrating obstacle: The limited external control that can be exerted over the most basic physical property of the dust - the charge - without having to completely alter characteristics of the surrounding plasma environment. Researchers have made enormous progress with dusty plasmas over the last few decades: Our understanding of the dust charging process and the forces acting on the dust has improved significantly over the last twenty years. Likewise, we have a far better grasp over how to use changes in plasma conditions to nudge the dust's equilibrium, dynamics, and coupling behavior in a desired direction than early experimenters did. However, through all of this progress the direct and independent control of the dust charge itself has remained a challenge. As illustrated in Figure 1.3, experimenters are constantly forced to compromise between the plasma conditions that they want or need for a given experiment, and the plasma conditions that will allow the dust to remain suspended within the experiment and fall into the coupling regimes and equilibrium behavior necessary for the experiment to work.

In order to continue improving our ability to study and control the behavior of the dust, we must ultimately seek out techniques that can allow the equilibrium properties of the dust to be altered independently of the plasma parameters. The key to developing such techniques, if they are possible, must lie in exploiting the charging behavior of the dust: Can we use external means to modify the incident electron and ion currents collected by the dust, or introduce new charging or discharging currents into the system with minimal perturbation to the background plasma?

The research presented in this dissertation will show, conclusively, that it can be done. We will present the results of several attempts to control the charging behavior of dust in

Figure 1.3: The inherent coupling between the equilibrium properties of the dust and the background conditions of the plasma limits the ability of experiments to control one without altering the other. Researchers and technicians must often settle for compromising between the plasma conditions they prefer and the plasma conditions that will confine or eliminate the dust from a region in the experiment. But what if we didn't have to?

a plasma, including a novel proof-of-concept test utilizing high-intensity ultraviolet light to discharge dust particles through photoelectric current with only minimal effects to the background plasma.

1.4 Outline of Dissertation

This dissertation is presented as seven chapters and two appendices. The content of these chapters will walk the reader through the theoretical background and related experimental work which led up to the photo-discharging experiment, the results and implications of that experiment, and the new research questions raised by it.

Chapter 1 introduces the concept of a dusty plasma and lays out the motivation for the research that will be discussed throughout the rest of this dissertation: Why dusty plasmas are important and why we desire the ability to more effectively and less disruptively alter and control their important properties.

Chapter 2 lays the conceptual and theoretical groundwork for exploring different techniques for controlling the dust charge as well as ultimately analyzing the efficacy of these techniques. This chapter discusses the physics of the dust charging process and introduces the Orbital Motion-Limited Charging model. The discussion of unaltered models of the dust

charging process serves as a prelude to investigating how the collection currents incident on the dust can potentially be modified, or how the introduction of new charging or discharging currents may alter the equilibrium charge of the dust. This chapter discusses the predominant forces acting on the isolated dust particles - the gravitational, electric, neutral drag, and ion drag forces. This chapter also discusses how these forces will be estimated, and introduces the different force balance models that will be used for estimating the dust charge later on.

Chapter 3 reviews the details of the hardware common to the experiments discussed in this dissertation and the diagnostics employed in analyzing the experimental results. This chapter introduces the Auburn Dusty Plasma Experiment (DPX), the principal experimental apparatus used for the work described in this dissertation. The basic layout of the chamber and the typical arrangement of components for the experiments are described. This chapter also presents the construction of the various probes used in measuring the different plasma parameters in the experiments, and in measuring the response of the background plasma to the different attempts made to control the dust charging process. The cameras and imaging techniques used in the experiments are presented and and the different analysis techniques utilized for diagnosing the dynamics of the dust are discussed. Finally this chapter presents data on the typical conditions and profiles of the typical, unperturbed background plasmas in these experiments, and presents justifications for some of the arguments regarding symmetry and analytic approximations that will be made in the experimental analysis.

Chapter 4 introduces the first of two experiments that form the body of this dissertation: An attempt to modulate existing charging currents incident on dust particles in order to reduce the net charge on the dust. This chapter introduces additional theoretical framework to describe the effects of a weak, oscillating electric field as a means of altering the existing charge collection by the dust; as well as modifications the baseline experimental apparatus described in Chapter 3. This chapter will demonstrate that this technique produces clear evidence of a change to the equilibrium dust conditions, and strong evidence of a reduction in

the net equilibrium charge of the dust. The effects of the oscillating electric field on the dust equilibrium and behavior will be discussed in detail. However, this chapter will also show that this method results in a non-negligible change in the background plasma conditions and fields and that the analysis of this method's efficacy is overly complicated by its effects on the plasma. It will show that while direct manipulation of the existing plasma currents may be possible, it is ultimately ill-suited to the goals of this research. It will conclude that the introduction of new charging currents represents the preferable angle of attacking this problem.

Chapter 5 introduces the second experiment: An attempt to introduce a large, externally-generated discharging current to the dusty plasma in the form of a photoelectric current induced by high-intensity ultraviolet (UV) light. This chapter introduces further theoretical modelling to describe the induced photoelectric current and its anticipated effects on the dust charge, and outlines the challenges of optimizing a proof-of-concept test. This chapter also outlines changes to the baseline experimental configuration described in Chapter 3 and also the additional hardware introduced for the proof-of-concept test. This chapter will demonstrate, unequivocally, that photo-discharging of dust particles can be accomplished in a high pressure, low-temperature plasma. It will further demonstrate that, if attempts are made to tailor the parameters of the UV source, this photo-discharging can be accomplished in such a way as to have a negligible effect on the background plasma. This chapter will conclude that photo-discharging represents the best approach for further improving attempts to independently control charge in dusty plasmas and outline future avenues for investigating and refining the technique.

Chapter 6 presents computational research which follows up on the experiment outlined in Chapter 5. The research into photo-discharging also led to the discovery of unexplained differences in particle behavior in response to the UV exposure - with some dust particles behaving periodically and predictably, and others behaving in an erratic, chaotic manner. This chapter uses computational modelling to investigate the hypothesized role that the

geometry and asymmetry of the dust grain shape plays in determining the nonlinear dynamics of the dust in response to the photo-discharging. This chapter outlines the computational model used to simulate the dust behavior and discusses some of the mathematical analysis used to analyze the results of the simulations. This chapter will conclude that the shape of the dust particles plays a critical role in determining the dust's response to the UV, and will discuss plans for further followup work.

Chapter 7 summarizes the results of the experiments outlined in Chapters 4 and 5, and examines the overall progress made during this research towards developing a method or family of methods of controlling the equilibrium charge of the dust. This chapter also discusses the potential applications and future directions for the work as well as introduces some of the follow-up research already underway.

Chapter 2

Theory

In order to begin to explore how modifications to the charging behavior of the dust may be developed and applied, the underlying mechanisms governing the charging process must be understood. In order to develop reliable estimates of the effects (if any) that these modifications have on the equilibrium of the dust, the predominant forces acting on the particles must also be understood. This chapter provides a theoretical foundation to both the dust charging process and the forces acting on the dust as a prelude to the modifications and analysis that will be explored in the experimental chapters.

2.1 Dust Charging Behavior

The charging process of dust suspended in a plasma environment is critical to the physics of dusty plasmas; the dust charge determines the forces acting on the dust, the equilibrium positions of the particles, the interactions between neighboring grains, the dispersion relation of density waves in a dust cloud, and much more. Analysis of dusty plasma behaviors, estimation of the properties of the dust, and understanding of the coupling between the dust and the plasma all require an understanding of the charging process; as does our ultimate goal of developing methods of modifying the dust charge.

Dust suspended in a plasma environment collects and emits positive and negative charges. The dust charge itself, Q_d, can be generally considered to be some function of space and time, which can shift or fluctuate as various physical processes compete with one another. This generally includes the collection of negative electrons in the plasma, I_{ed} and the collection of positive and/or negative ion species, $\sum I_{id}$, but may also include other effects like secondary electron emission, I_{see}, thermoemission, I_{th}, photoemission, I_{pe}, and so

on.

$$\frac{dQ_d}{dt} = I_{ed} + \sum I_{id} + I_{see} + I_{th} + I_{pe} + \ldots \tag{2.1}$$

To begin to understand this complex balancing act of collection and emission we start by considering only the collection of negative electrons and positive ions in a singly-ionized, single gas plasma.

2.1.1 Orbital Motion-Limited Charging

The most common approach employed for estimating the collection currents by dust suspended in a plasma is known as the Orbital Motion-Limited model (OML). In the OML approach the plasma is assumed to be in a steady-state, with collisionless ions and electrons. The collection of the electrons and ions by the dust particle is treated classically, without regard for atomic processes. This model also ignores the effects on the potential structure surrounding the particle that may arise due to Debye shielding. While these assumptions are not necessarily reasonable for all particles and all plasmas, we can justify these approximations for the kinds of low temperature laboratory plasmas being dealt with in these experiments: Plasma densities are low enough that electron-ion and ion-ion collisions can be neglected (the matter of electron-neutral and ion-neutral collisions will be discussed later), and in general the particles themselves are sufficiently small with respect to the shielding scale length that the effects of that shielding on the charging process can be neglected. The description of the OML charging process below will follow the approach described by Shukla & Mamun[33].

Let us consider, as shown in Figure 2.1, a charged, spherical dust particle with a radius, r_d and some electrostatic potential at its surface, ϕ_d. The dust particle is approached by a point particle, s, with a charge, q_s, and a mass, m_s[1]. Let the smaller charge start from some arbitrary distance, b_s, from the dust particle. Assume that b_s is sufficiently distant that the

[1]In this text, the subscript s will typically be used to identify theoretical and experimental parameters relating to generic or unspecified plasma species, e for electrons, i for ions, n for neutrals, and d for dust.

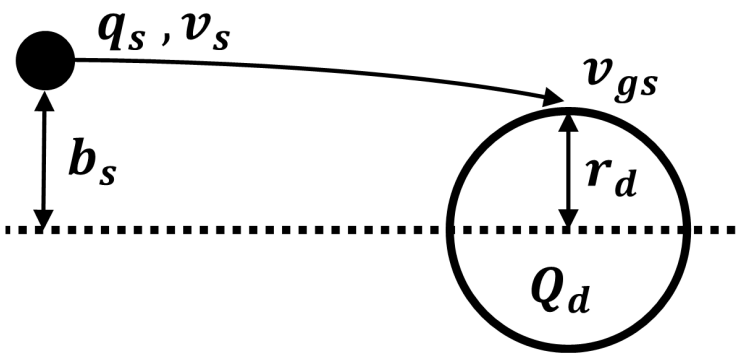

Figure 2.1: Diagram of the model for charge collection used in the Orbital Motion-Limited model. The interaction is treated classically, applying conservation of angular momentum and energy to derive velocity-dependent collision cross-sections between the charged plasma species and the dust.

electrostatic potential energy of the particle can be taken as zero. Also assume that the small particle is just barely collected by the dust with some grazing velocity, v_{gs}. Given all of this information, we can write a statement for the conservation of angular momentum of the charged particles approaching the dust surface:

$$m_s \, v_s \, b_s \; = \; m_s \, v_{gs} \, r_d \tag{2.2}$$

And can also describe the conservation of energy of the charges:

$$\frac{1}{2} \, m_s \, {v_s}^2 \; = \; \frac{1}{2} \, m_s \, {v_{gs}}^2 \; + \; q_s \, \phi_d \tag{2.3}$$

From this starting point, we can derive a collection cross-section for each of the charges by the dust, which we will define as:

$$\sigma_{sd} \; = \; \pi {b_s}^2 \; = \; \pi {r_d}^2 \left(1 - 2 \, \frac{q_s \, \phi_d}{m_s \, {v_s}^2} \right) \tag{2.4}$$

Now, assume that the dust particle can be treated as a spherical capacitor with a capacitance, $C_d = 4\pi\epsilon_o r_d$. The electrostatic potential at the surface of the dust particle can then be described in terms of the equilibrium charge of the dust, $\phi_d = Q_d / C_d$. We can also

define a normalized dust charge, defined as the ratio of the electrostatic potential energy of the charges at the dust surface to their thermal energy, $z_s = |(q_s\phi_d) \ / \ (k_B T_s)|$. This notation will be used later to simplify our expressions for the currents. For ions and electrons with a thermal speed, $v_{ts} = \sqrt{k_B T_s \ / \ m_s}$, we can describe motion in terms of a thermal Mach number, $M_s = v_s/v_{ts}$. Using these definitions, the velocity-dependent collection cross sections for the electrons and ions can be written in the condensed form:

$$\sigma_{ed} = \pi {r_d}^2 \left(1 - 2\frac{z_e}{{M_e}^2}\right) \tag{2.5}$$

$$\sigma_{id} = \pi {r_d}^2 \left(1 + 2\frac{z_i}{{M_i}^2}\right) \tag{2.6}$$

Where σ_{ed} and σ_{id} are the cross sections for the electrons and ions, respectively, being collected by the dust. For dust suspended in a low-temperature plasma, we can assume, due to the much higher mobility of the electrons compared to the ions, that the dust will collect an excess of electrons and therefore have a negative equilibrium charge.[33] In that case we can define the equilibrium charge as, $Q_d = -Z_d \ e$ where Z_d is the dust charge number (the number of excess electrons on the surface at any moment).

For deriving the incident currents we assume that the collection of charge by the dust can be described statistically, beginning with some flux of particles, Φ_{sd}, which can be described in terms of the velocity-dependent cross sections above and integrated for some velocity distribution of the plasma species:

$$I_{sd} = \langle q_s \ n_s \ v_s \ \sigma_{sd} \rangle = \int q_s \ n_s \ v_s \ \sigma_{sd} \ f_s(v_s) \ d^3 v_s \tag{2.7}$$

Assuming that there is a Maxwellian velocity distribution for both the ions and electrons:

$$f_s(v_s) \ d^3 v_s = \sqrt{\frac{2}{\pi}} {M_s}^2 \ e^{-\frac{{M_s}^2}{2}} \ dM_s \tag{2.8}$$

Gives analytic expressions for the incident ion and electron currents:

$$I_{ed} = -\sqrt{8\pi}\ e\ n_e\ v_{te}\ {r_d}^2\ e^{-z_e} \tag{2.9}$$

$$I_{id} = +\sqrt{8\pi}\ e\ n_i\ v_{ti}\ {r_d}^2\ (1\ +\ z_i) \tag{2.10}$$

To complete the derivation, we will apply two final assumptions. First, we will assume that the quasi-neutrality condition applies to the dusty plasma:

$$-e\ n_e + e\ n_i - Z_d\ n_d = 0 \tag{2.11}$$

From this condition we can relate the electron, ion, and dust densities in terms of a Havnes parameter, $P_H\ =\ Z_d\ n_d\ /\ n_i$. We will, furthermore, assume that the equilibrium charge is determined by a floating potential condition; that is to say that we will assume there is some charge and surface potential for which the collection of electrons and ions will balance out:

$$I_{ed} + I_{id} = 0 \tag{2.12}$$

From these two assumptions and the expressions for the currents from (2.9) and (2.10) we can derive(2.13)[33]:

$$e^{-z_e}\left(\frac{1-P_H}{1+z_i}\right) = \left(\frac{T_i\ m_e}{T_e\ m_i}\right)^{1/2} \tag{2.13}$$

And, since z_e, z_i, and P_H, are all functions of Z_d, this expression can be solved numerically to obtain the dust charge number.

2.1.2 Modifications to Charging

The charging model above is by no means an exhaustive or complete description of the charging process. The OML model makes assumptions that may not apply to every set of experimental parameters, and ignores some physical processes which may be important, but

it provides us with some basic insights for how the properties of the dust and plasma effect the equilibrium charge of the dust, and gives us some ideas for what approaches may exist for manipulating the dust charge.

The first approach we can consider is the modification of the existing plasma currents incident on the dust. As the derivation indicates, the collection currents and the resulting equilibrium condition between them are complex and nonlinear functions of the masses, temperatures, and densities of electrons and ions in the plasma. Altering any of these experimental parameters or altering the distribution functions of the plasma species to something non-Maxwellian would alter the plasma currents found in (2.9) and (2.10) and alter the resulting equilibrium condition for the dust charge. Steady-state changes to these conditions are not an option, as doing so would alter the plasma and defeat the entire purpose of the exercise; however time-dependent changes in these properties may present options worth exploring, if there are fluctuations that can produce a time-average effect on the dust charging currents with a minimal affect on the steady-state of the plasma. The research presented in Chapter 4 investigates whether controlled fluctuations in the charging currents, produced by an oscillating electric field applied to the background plasma, can accomplish this.

The second approach we can consider is the introduction of new current sources. As (2.1) and (2.12) indicate, any additional sources of charging or discharging will alter the equilibrium charge of the dust. As is the case for modification of the existing currents, most of the options at our disposal are not what would could be considered minimally disruptive: Injecting gas into the plasma to absorb free electrons and form negative ions, introducing an electron beam to bombard the dust with negative charge, or heating the dust to induce secondary emissions are all options that could significantly alter the equilibrium charge of the dust, but all require major alterations to either the background plasma, the dust, or both. The research presented in Chapter 5 investigates whether photoemission, induced by a UV source, can alter the dust charge while producing a minimal perturbation to the physical condition of the dust and the background plasma.

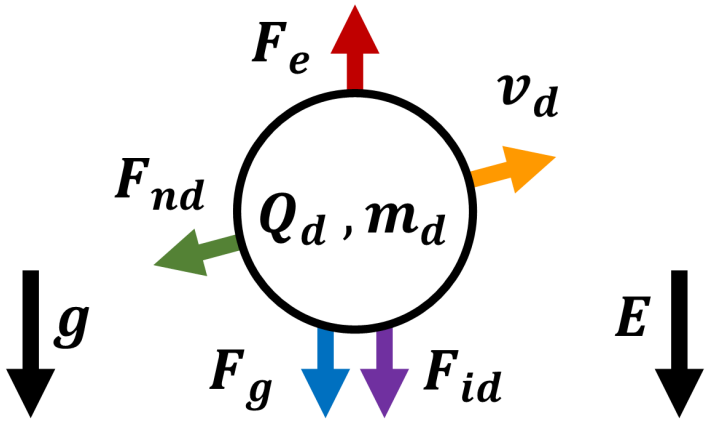

Figure 2.2: Free Body Diagram of a negatively-charged dust particle and the predominant forces acting on it in a weakly-ionized, non-magnetized plasma. These forces include the gravitational (F_g) and electric forces (F_e), the interaction between the dust and non-ionized neutral particles (neutral drag, F_{nd}), and the interaction between dust and streaming ions in the background plasma (ion drag, F_{id}).

2.2 Forces

Any examination of the physical behavior of dusty plasmas requires an understanding of the forces acting on the dust. Modelling the forces acting on the dust can be paradoxical; on the one hand, the behavior of isolated particles can be treated with a Newtonian approach and several of the interactions are straightforward to model or at least approximate, but on the other hand the predominant forces all have very different responses to the dust scale and to the properties of the background plasma, which can make predicting or controlling the behavior of the dust deceptively complex. For a weakly-ionized plasma like those that will be explored in the experiments described in later chapters, only four forces will be relevant (illustrated in Figure 2.2): The gravitational force acting on the dust's mass, the electric force acting on the dust's charge, the effect of collisions with neutral gas particles in the system (which we will call the neutral drag), and the interaction between the dust and flowing ions in the plasma (which we will call the ion drag).

Predominant Forces in Dusty Plasmas		
Force	Source of Force	Scaling
Gravitational	Gravity	${r_d}^3$
Electric	Electric Fields	r_d
Neutral Drag	Interaction with neutrals	${r_d}^2$
Ion Drag	Interaction with ions	${r_d}^2$

Table 2.1: The four primary forces acting on dust particles suspended in a non-magnetized plasma: the gravitational and electric forces, and the neutral and ion drag. The forces are (arguably) ordered from most simple to most complex in terms of modelling and experimental difficulty in estimating. The approximate scaling, with respect to the physical size of the dust, is also listed.

2.2.1 Simple Forces

The force of gravity on the dust's mass and the electric force acting on the dust's charge are what we will describe as "simple forces". These forces require the fewest assumptions in order to model them, and the fewest experimental measurements in order to estimate them. These forces will form the basis of the simpler of the two force balance models we will introduce later in this chapter.

The most obvious contrast with forces in conventional plasmas is the role that gravity plays in dusty plasmas. The mass of the dust particles is generally millions or even billions of times greater than the mass of the ions in the plasma, and the effect of the gravitational force on the dust's equilibrium and dynamic behavior cannot be neglected or even overstated: For micron-sized dust grains, the gravitational force is often the dominant force acting on the dust in any ground-based experiment.

$$\mathbf{F_g} \;=\; m_d\,\mathbf{g} \tag{2.14}$$

The gravitational force on the dust is trivial to estimate, assuming that the size and shape of the particles are relatively monodisperse. Most laboratory experiments with dusty plasmas employ highly monodisperse microspheres of silica or melamine formaldehyde (MF)

specifically for this reason. Dust comprised of more irregularly-shaped particles, or polydisperse size distributions of dust can make calculating the gravitational force more challenging, but not impossible.

The presence of a significant gravitational force in ground-based experiments also informs experimental efforts to suspend and confine the dust. Most experiments rely on producing a strong electric force to counteract the downward pull of gravity. There are, of course, other means of suspending particles, such as imposing a temperature gradient in the gas to produce a thermophoretic force on the dust, but the inherent electrical fields produced in generating the plasma make electric forces an obvious choice for suspending and confining the dust.

$$\mathbf{F_e} \;=\; Q_d\,\mathbf{E} \tag{2.15}$$

Like the gravitational force, the electric force is trivial to model, provided we know the right information. If the potential structure of the plasma is known, then the background electric field can be calculated which leaves only the dust charge itself as an unknown.

2.2.2 Collisional Forces

In a weakly-ionized dusty plasma we must consider the effects of three collisional interactions which affect the background plasma and the dust: Collisions between neutrals and electrons and ions in the background plasma, collisions between the neutrals and the dust, and collisions between the ions and the dust.

Collisions between the neutrals and the plasma ions and electrons can limit the mobility of these lighter charged species. This mobility-limited behavior can produce drift motion and alter the ambipolar diffusion of the electrons and ions in the background plasma. For a given neutral density, n_n, and a collisional cross-section between the charged plasma species and

the neutrals, σ_{sn}, we can define a collisional mean free path for the plasma species:

$$\lambda_{sn} = \frac{1}{n_n \sigma_{sn}} \tag{2.16}$$

And can define a collision frequency:

$$\nu_{sn} = \frac{v_{ts}}{\lambda_{sn}} \tag{2.17}$$

The collision cross sections between the electrons and neutrals is a complex function of the electron temperature, but can be broken down into a term for elastic scattering, a term for ionization, and a term for excitation (details for which can be found in Lieberman & Lichtenberg (2005)[21]). The cross section between the ions and neutrals in a low-temperature plasma, on the other hand, can usually be approximated as a simple hard-body collision between two spheres with radii equal to the Van der Waals radius of the gas particles. For argon, which has a Van der Waals radius of 188 pm (LANL, n.d.[26]), this gives an ion-neutral collision cross section, $\sigma_{in} \sim 4.44 \times 10^{-19}\ m^2$.

We can describe the dynamics of the plasma particles as:

$$m_s \mathbf{a_s} = q_s \mathbf{E} - m_s \nu_{sn} \mathbf{v_s} \tag{2.18}$$

For a steady-state plasma it is assumed that there is some drift velocity, v_{Ds} for which the electric force and collisions balance each other out[2]. Defining a mobility, $\mu_s = q_s / m_s \nu_{sn}$, we can express that drift velocity as:

$$\mathbf{v_{Ds}} = \mu_s\ \mathbf{E} \tag{2.19}$$

[2]The subscript D will be used to distinguish physical parameters related to drift motion here and in Chapter 4 from properties relating to the dust (d).

We can also define a drift thermal Mach number:

$$M_{Ds} = \frac{v_{Ds}}{v_{ts}} \tag{2.20}$$

Which, for an ideal neutral gas, $P_n = n_n k_B T_n$ can be expressed as:

$$M_{Ds} = \frac{T_n}{T_s}\left(\frac{q_s\, E}{\sigma_{sn}\, P_n}\right) \tag{2.21}$$

While the inertia and charge of the neutral and ionized gas particles are both orders of magnitude lower than those of the dust, their collective effect on the motion and equilibrium of the dust cannot always be ignored. While the gravitational and electric forces are simple, even trivial to model and estimate, the same is not so true for these collective interactions with the background gas and plasma.

The effect of neutral atoms colliding with the dust (or the dust colliding with neutral particles, depending on the point of view) is especially important to consider in weakly-ionized plasma experiments like those that will be examined in this dissertation. The effects of the neutral drag on the dust can dampen or even mobility-limit the motion of the dust in the plasma.

The interaction between the neutrals and dust is described using the Epstein drag model.[4] The dust is assumed to be spherical and travelling with a subsonic velocity, v_d, relative to a background of neutral particles with mass, m_n, temperature, T_n, and thermal velocity $v_{tn} = \sqrt{k_B T_n / m_n}$. The dust is also assumed to be small compared to the mean free path of the neutrals. In the case of a negligible background flow in the neutral gas, the observed and relative velocity of the dust can be taken to be the same. Under these assumptions the drag force exerted by the neutrals takes the form:

$$\mathbf{F_{nd}} = -\frac{8\sqrt{2\pi}}{3} {r_d}^2 m_n n_n v_{tn} \mathbf{v_d} \tag{2.22}$$

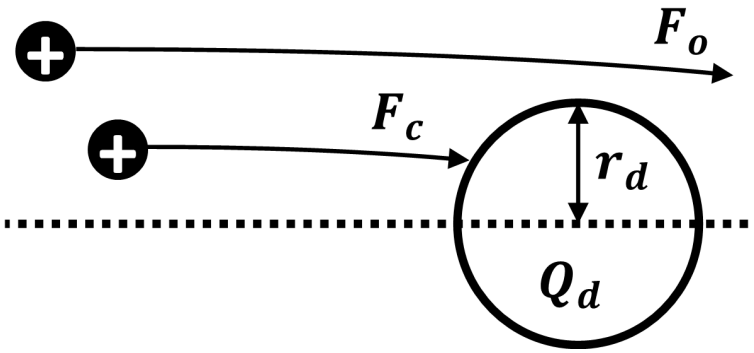

Figure 2.3: Diagram of the models for the collected and orbital components of the ion drag force acting on the dust. The quantitative modelling of these forces is still an open question in dusty plasmas physics, but qualitatively the flow of ions into and about a dust particle produces a net force along the direction of the electric field. For negatively-charged dust the ion drag force will oppose the electric force.

The interaction between negatively charged dust particles and positively charged ions in the background plasma is an effect that is quite important to dusty plasmas. Qualitatively, this interaction is simple to describe - ions in the plasma flow preferentially along the direction of the background electric field, and as they collide with or are scattered by the dust particles, momentum is transferred by the interaction. The net result is that ions in the plasma push and pull the negatively charged dust particles in the direction of the electric field (and opposite the direction of the electric force on the dust). Actually modelling this force, on the other hand, is considerably more complicated. A simplified model was first introduced in Barnes (1992)[1], which breaks the ion drag into a collection component (momentum transfer from direct collisions with ions) and an orbital component (momentum transfer from Coulomb collisions with ions grazing or passing close to the dust particle). These components are illustrated in Figure 2.3.

$$\mathbf{F_{id}} \;=\; \mathbf{F_c} \;+\; \mathbf{F_o} \tag{2.23}$$

The Barnes model for the ion drag is appropriate for making a preliminary, order-of-magnitude estimate of the ion drag force but, like the OML charging model, requires

several assumptions to be properly evaluated. Because of the complexity of modelling the momentum transfer between the ions and the dust and the debate over the appropriate cross sections, distributions, and even bounds of integration to use in calculating it, a complete and accurate modelling of the ion drag force is still, very much, an open question in dusty plasma physics. Numerous improvements and modifications to the Barnes model have been made over the years, many relying on quasi-analytic functions or even purely numerical simulation. For the work described in this dissertation we will apply the model for the orbital force developed in Khrapak (2002)[19] and the model for the collection force developed in Uglov (1991)[42] and Hutchinson (2003, 2004, 2006)[12][13][14]. A summary of both models can also be found in Hall (2016)[10].

In brief: If we assume that the background ions take on a shifted Maxwellian velocity distribution (that is, a Maxwellian with some background drift velocity):

$$f_s(v_s)d^3v_s = \frac{1}{\sqrt{2\pi}}\frac{M_s}{M_{Ds}}\left[e^{-\frac{(M_s-M_{Ds})^2}{2}} - e^{-\frac{(M_s+M_{Ds})^2}{2}}\right]dM_s \tag{2.24}$$

Then this distribution can be used in combination with a more complete model of the momentum transfer, in order to derive the orbital and collisional components of the ion drag force, which can be written as:

$$\mathbf{F_o} = n_i\ k_B T_i\ \pi {r_d}^2\ \ln\Lambda\ G(M_{Di})\ \hat{\mathbf{E}} \tag{2.25}$$

$$\mathbf{F_c} = n_i\ k_B T_i\ \pi {r_d}^2\ H(M_{Di})\ \hat{\mathbf{E}} \tag{2.26}$$

Where $\ln\Lambda$ is the Coulomb Logarithm, and G and H are unitless scale functions for the orbital and collisional fluxes (here, $F(x)$ is the error function):

$$G(M_{Di}) = 4\frac{{z_i}^2}{{M_{Di}}^2}\left(F\left(\frac{M_{Di}}{\sqrt{2}}\right) - \sqrt{\frac{2}{\pi}}M_{Di}e^{-\frac{{M_{Di}}^2}{2}}\right) \tag{2.27}$$

$$H(M_{Di}) = \sqrt{\frac{2}{\pi}} e^{-\frac{{M_{Di}}^2}{2}} \left(\frac{{M_{Di}}^2 + 2z_i + 1}{M_{Di}} \right) + F\left(\frac{M_{Di}}{\sqrt{2}} \right) \left(\frac{{M_{Di}}^4 + 2{M_{Di}}^2 + 2z_i \left({M_{Di}}^2 - 1 \right) - 1}{{M_{Di}}^2} \right) \quad (2.28)$$

2.2.3 Force Balance Models

The experimental research presented in this dissertation will employ three models for estimating the effects (if any) of different techniques on the equilibrium charge of dust particles in the plasma. The first model is the OML charging model derived and outlined in Section 1.1. The second is what we will refer to as the Simple Force Balance model (SFB). In this approach we consider only the gravitational and electric forces to estimate the charge of the dust.

$$\mathbf{F_g} \; + \; \mathbf{F_e} \; = \; 0 \quad (2.29)$$

The third is what we will refer to as the Full Force Balance model (FFB), which includes the instantaneous acceleration of the dust (if it is measurable) as well as adding the neutral drag and ion drag forces into the equation.

$$m_d \, \mathbf{a_d} \; = \; \mathbf{F_g} \; + \; \mathbf{F_e} \; + \; \mathbf{F_{nd}} \; + \; \mathbf{F_{id}} \quad (2.30)$$

Each model has advantages and disadvantages: The OML model takes the charging behavior of the dust into consideration, however it makes a number of approximations for modelling this process that may not hold for all regions of the plasma or the dust cloud. The SFB model is the simplest to calculate (assuming a reasonable estimate of the dust mass and a good measurement of the electric field are known), however the exclusion of the collisional forces may not be a good approximation in some or most regions of a particular plasma. The FFB model is the most complex to calculate, and requires the most assumptions due to the uncertainty of the quantitative estimate of the ion drag force, but provided these additional forces are at least of the correct order of magnitude it should provide a closer estimate of the

dust charge in most regions of the plasma. In the cases shown in this research (outlined in Chapters 4 and 5), it will be shown that the OML model generally represents a lower-bound to any estimated discharge of the dust, while the SFB model represents an upper-bound.

Chapter 3

Experimental Apparatus and Diagnostics

In this chapter we introduce the Auburn Dusty Plasma Experiment or DPX; the apparatus on which the experiments that will be described were performed. This chapter also discusses the components, diagnostics, and analytic methods common to the two experiments discussed in this dissertation. Section 3.1 presents the baseline apparatus; the chamber, gas and vacuum components, and the plasma-generating components and power supplies. Section 3.2 presents the physical construction of the various probes employed in the experiments and discusses the extraction of plasma properties from the various probe measurements. Section 3.3 presents optics - the various cameras and light sources employed in the experiments, their calibration, and how data from the devices is processed and analyzed. Section 3.4 characterizes the different types of dust grains utilized in the experiments. The specific configurations, elements, and instruments utilized in each experiment will be discussed in later chapters.

3.1 The Dusty Plasma Experiment (DPX)

The experiments discussed in this dissertation were all performed on the Auburn Dusty Plasma Experiment (DPX)(Thomas 1999[38]). This device was developed over 20 years ago to function as an experimental apparatus for investigating the behavior of dust suspended in low-temperature and weakly ionized plasmas.

3.1.1 Chamber Layout and Support

As seen in Figure 3.1, the basic layout of the DPX consists of a joined pair of standard ISO-100, stainless steel, six-way cross chambers. As viewed from the 'front' in Figure 3.2,

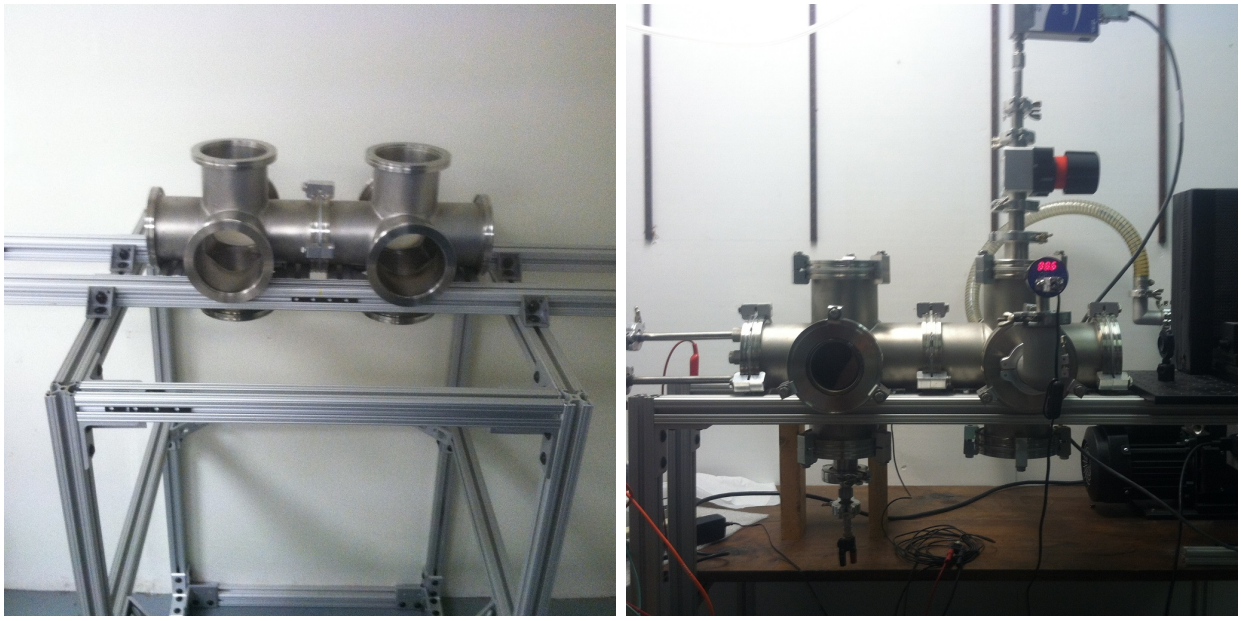

Figure 3.1: The Dusty Plasma Experiment (DPX) at Auburn University, (*left*) as seen during reassembly at its new home in the MPRL center lab. (*right*) View of the exterior of the primary chamber during setup of one of the experiments. A simple-but-robust apparatus, the DPX is frequently used by the Auburn Magnetized Plasma Research Laboratory (MPRL) for experimenting with unmagnetized and weakly-ionized dusty plasmas.

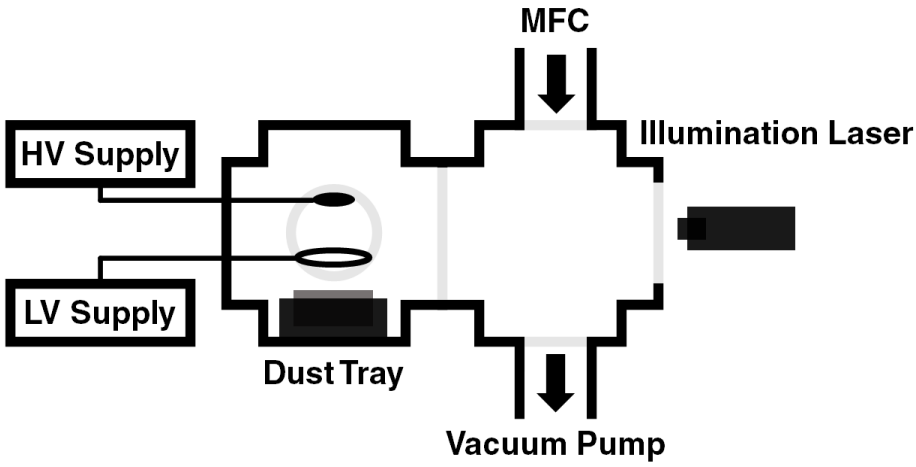

Figure 3.2: Unmodified layout of the Dusty Plasma Experiment (DPX) apparatus. The primary chamber (*left*) holds the critical experimental components: The plasma generating anode (*disk*), which is connected to a high voltage, current-limited power supply; the confining electrode (*ring*), which is connected to a low voltage DC bias; and dust tray. The secondary chamber (*right*) contains access to the mass flow controller and vacuum pump, as well as access for the illumination laser.

the chamber on the left side (the primary chamber) holds the bulk of the actual experimental components and diagnostics; this includes the conducting electrodes which are used to form the plasma and shape the potential structure within the device, the various diagnostic probes, and the loaded dust tray. The primary chamber is also where the dust is injected and suspended within the device. The right side (the secondary chamber), meanwhile, functions as the access point for the gas inflow, the vacuum pump, and neutral pressure gauge. Kodial glass viewports provide optical access for lasers and other light sources, while a transparent acrylic flange provides optical access for cameras.

The connected chambers rest on top of a mount constructed of standard 80/20 aluminum T-slot structural framing provides a stable support for the chambers. The mount is designed to keep the experiment stable and level with the ground as well as provide mounting points for the various cameras and light sources.

3.1.2 Gas and Pressure Regulation

As shown in Figure 3.3, Argon gas is delivered to the DPX through an MKS Instruments G-Series GE50A mass flow controller (MFC) connected to the flange on the top of the secondary chamber. Atmospheric gasses are pumped out of the chamber by a Kurt J Lesker ULVAC GLD-136C rotary vacuum pump located in the base of the mount and connected to the bottom flange of the secondary chamber. This pump can sustain a baseline vacuum pressure of $\lesssim$5 mTorr. The applied voltage to the MFC is controlled using a LabView VI. At maximum voltage applied to the MFC, and the outlet to the pump fully open, the balance between inflow and outflow of neutral gas reliably holds the interior equilibrium operating pressure at $\sim$120-125 mTorr using the argon gas. This is the gas pressure range used for all of the experiments described in this dissertation.

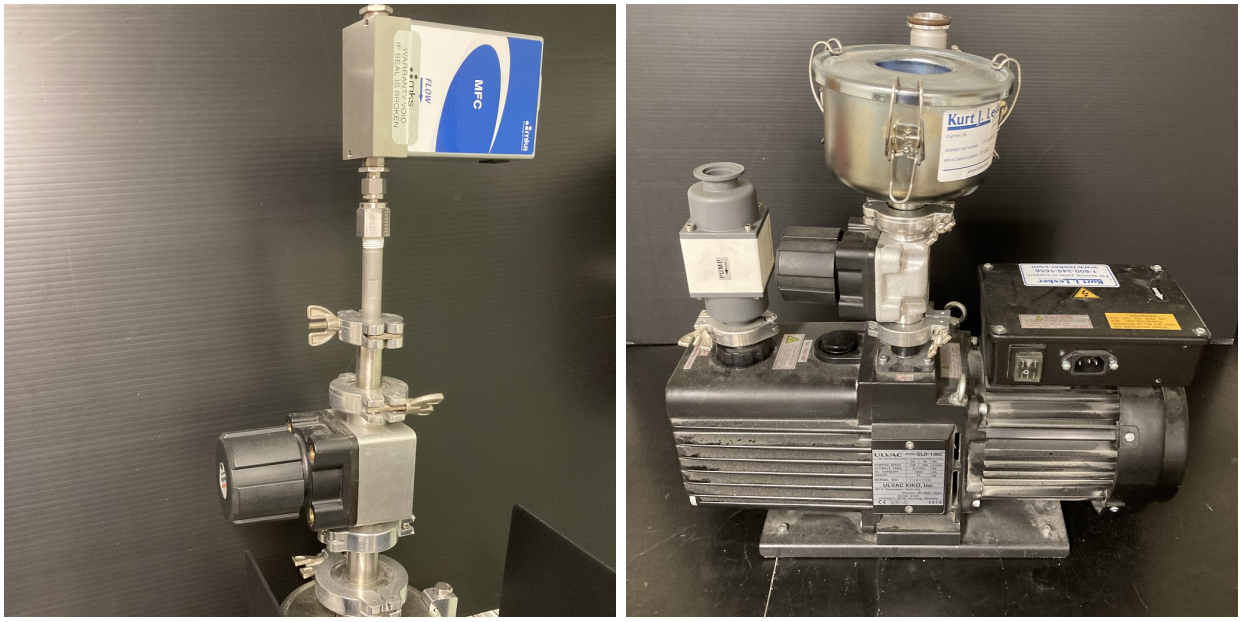

Figure 3.3: Equipment used in the gas and pressure regulation of the DPX experiment. (*left*) The mass flow controller (MFC) which provides regulated flow of argon gas into the secondary chamber. (*right*) The roughing pump which evacuates gas from the chamber. The pump can sustain a baseline vacuum pressure of $\lesssim 5$ mTorr in the chamber. Operating neutral pressure for the experiments described in this dissertation was $\sim$ 120-125 mTorr.

3.1.3 Electrodes and Power

While the specific size, shape, and configuration of plasma generating and confining components within the primary chamber varies slightly between experimental configurations (the specific measurements can be found in Chapters 4 and 5), the basic layout of the primary chamber is always the same: A powered electrode above the geometric center of the primary chamber acts as the anode/plasma source, a negatively biased ring electrode located below the center of the chamber acts as the cathode/sink. The two electrodes create an electric field pointing downward and radially outward away from the source at the top of the chamber. For the negatively charged dust particles, this field creates an upward and inward electric force which helps confine the dust. All of the interior electronics are biased relative to the electrically grounded walls of the stainless steel vacuum chamber.

The plasma is primarily powered by a Glassman EH Series high voltage power supply operated in current-limited mode. For the experiments described in this dissertation, the

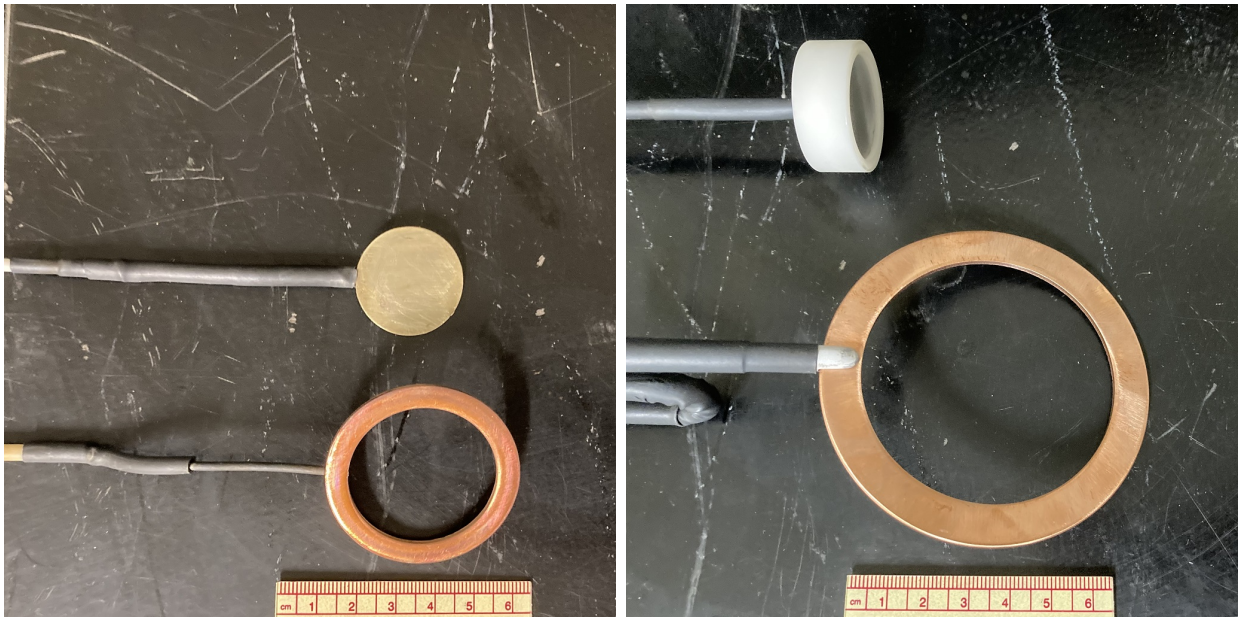

Figure 3.4: Electrodes used for plasma generation and dust confinement in the experiments described in this dissertation. (*left*) The 2.9 cm brass disk anode and small copper confining electrode (outer diameter, 4.8 cm, inner diameter, 3.7 cm) used for the baseline measurements described in this chapter and the experiment described in Chapter 4. (*right*) The 2.8 cm aluminium disk anode and the larger copper confining electrode (outer diameter, 8.3 cm, inner diameter, 6.4 cm) used in the experiment described in Chapter 5.

supply was operated at 2.0-2.5 mA of current. The confining electrode is connected to an Instek GPR-30H10D power supply operating in voltage-limited mode. The specific voltage applied to the confining electrode varies between experimental configurations. Figure 3.4 shows the different electrodes used in the experiments described in this dissertation.

The dust itself is scattered onto a large, electrically floating aluminum disk located beneath the confining electrode. This dust tray is held by a cylindrical delrin mount. The dust particles are injected into the plasma by temporarily increasing the bias on the confining electrode to generate random discharges. This 'arcing' kicks dust up into the plasma where it collect charge and transports to an equilibrium position, typically located near the center of the primary chamber.

Additional equipment was introduced and modifications to the apparatus and hardware described here were made to accommodate the needs of the experiments outlined in Chapters 4 and 5. The specifics of these additions and alterations are outlined in those chapters.

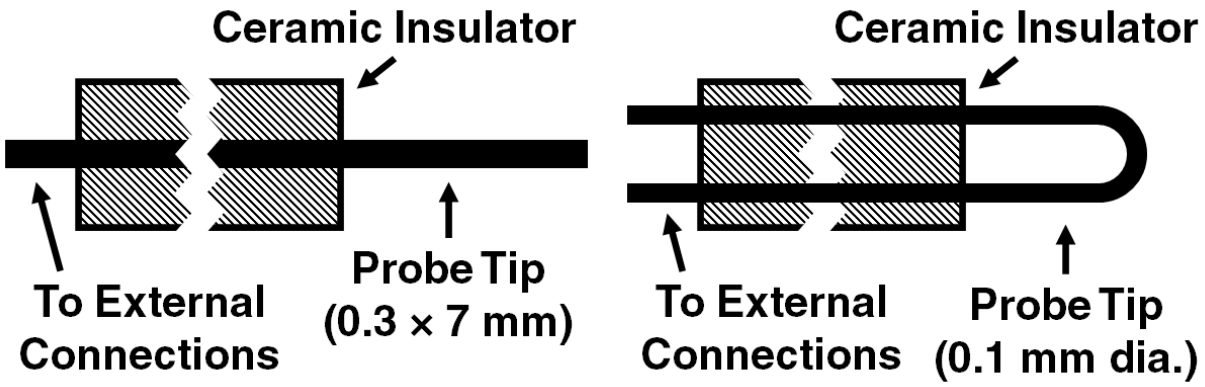

Figure 3.5: Schematic diagrams of two of the probe types used in the research presented in this dissertation. Langmuir probes (*left*) consist of a single, electrically biased wire. Emissive probes (*right*) consist of an exposed loop of wire heated by an external power source. Both probes can be used to measure and estimate different plasma parameters.

3.2 Plasma Diagnostics

In order to be able to estimate the effects of any of the techniques that will be explored in this dissertation, it is necessary to be able to measure at least three key plasma parameters within the primary chamber: The potential structure (which is necessary to estimate the electric field), the density profile, and the temperature profile. Most of the plasma diagnostics utilized in this research take the form of simple probes like those shown in Figure 3.5.

3.2.1 Langmuir Probes

Cylindrical Langmuir probes are a simple and robust tool for measuring plasma parameters and the specifics of extracting information from the probe response are well established (Merlino 2007[24]). For the experiments described in this dissertation, Langmuir probes were assembled using 0.3 mm thick tungsten wires insulated by alumina tubes. A length of wire 7 mm long was left exposed at the plasma-facing end of the alumina tubes, giving an effective probe area of approximately $\sim 6.6\ mm^2$. At the base of the alumina tubes, the tungsten wires are joined to a copper wire using a set screw wire connector, which in turn connects to a pin connector sized for a standard BNC feedthrough. Feedthroughs of various lengths

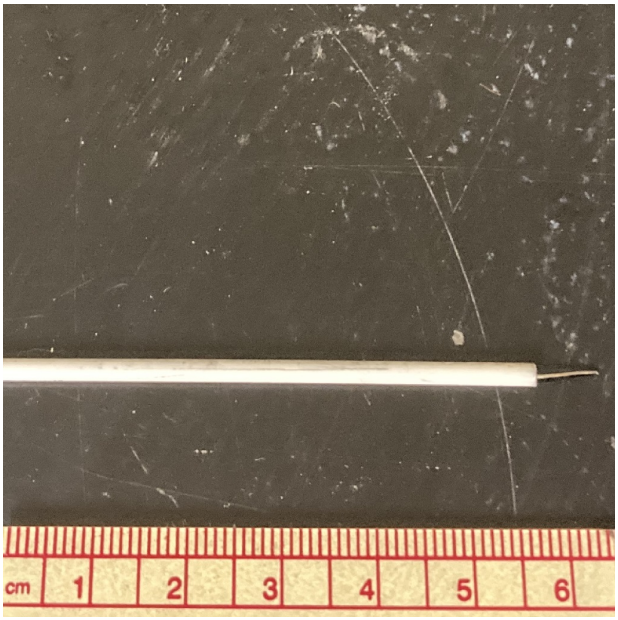

Figure 3.6: Example of one of the many Langmuir probes used for measuring properties of the background plasma during experiments, and to investigate the effects of various charge control methods attempted in this research. The tungsten wire has a diameter of 0.3 mm and an exposed length 7 mm. Probes are encased in alumina tubes to insulate the rest of the wire from the plasma.

are used to give the probes stability as they are extended into or extracted from the plasma. An example of one of these Langmuir probes can be seen in Figure 3.6. The probe wires were provided with a DC voltage bias using an Instek GPR-30H10D power supply and the voltage was swept using a Keithley 2400 Series Sourcemeter) which simultaneously recorded the current collection by the probe. The Langmuir probes used in our experiments could reliably measure the ion saturation current, floating potential, and electron temperature of the plasma. Since one of the goals of the research presented in this dissertation is to determine if methods used to alter the dust temperature can be utilized in a way which minimizes the effect on the background plasma, many of the analyses in later chapters will consider the relative or fractional change in plasma or dust parameters:

$$\delta_f \equiv \frac{\Delta f}{f} \tag{3.1}$$

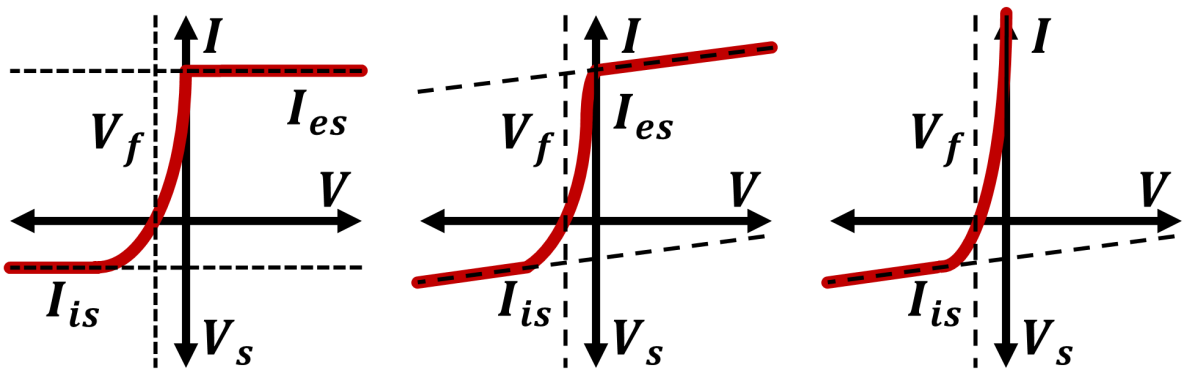

Figure 3.7: An illustration of Langmuir probe diagnostics. In the ideal I-V characteristic (*left*), the ion and electron currents saturate and are easily identified. In a more realistic trace (*middle*) like those seen in most MPRL RF-generated plasmas, the currents saturate to an approximately linear trend that can be traced to the floating or space potentials to estimate the saturation current. In lower power plasmas (*right*) the electron current rarely saturates, however estimates of the floating potential, ion saturation current, and electron temperature can still be obtained.

There are other advantages to using the Langmuir probes. The manner in which the probe collects current from the surrounding plasma is not dissimilar from how the dust itself collects charge from its environment. Chapter 4 will compare changes in the ion saturation current collected by the probe to changes in the predicted ion current collected by dust particles.

Langmuir probes do, however, have some disadvantages and caveats when used in low-power, weakly-ionized discharges. In the idealized current-voltage response, the ion and electron currents both saturate at sufficiently negative and positive voltages. While this typically occurs in highly ionized plasmas, like those in Q-machine devices, or high-power RF plasmas, these currents generally do not saturate in the low-power, weakly-ionized LTPs like those presented in this research. At sufficiently negative voltages where we would expect to see ion saturation, instead we generally see a linear increase in the ion current. At these biases the sheath structure around the probe becomes modified and effectively increases the collection area surrounding the probe, which increases the collected ion current collected.

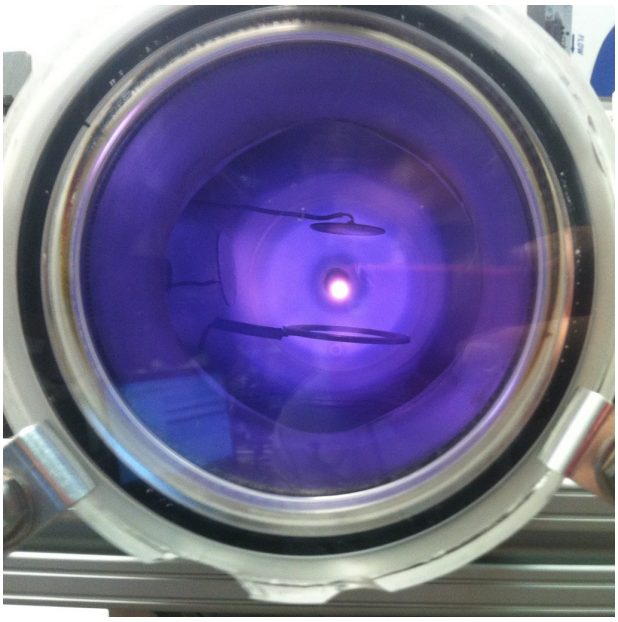

Figure 3.8: Anode glow generated by a Langmuir Probe in one of the test plasmas generated in DPX. In high pressure plasmas ($\gtrsim$ 100 mTorr) probes biased near the plasma potential can transition from a perturbative regime (where probe measurements can be reliably interpreted) to a discharge regime where the probe itself becomes a secondary plasma source. This necessitates the use of an emissive probe in situations where the floating potential cannot be used as a surrogate.

The ion saturation current can still be estimated by fitting a linear function to this increasing ion current and extrapolating it back to the floating potential (as illustrated in Figure 3.7).

Additionally, at voltages approaching or exceeding the plasma potential the power being drawn by the probe can become comparable to the power drawn by the anode. Under these circumstances (demonstrated in Figure 3.8) the probe itself can transition into a mode of operation where it acts as a secondary plasma source. This can make the conventional approaches for estimating the plasma potential unreliable. This can, in turn, make estimation of the background electric field in low-power LTPs more challenging.

For a Maxwellian, quasi-neutral plasma the relationship between the floating and space potential measured by a grounded Langmuir probe can be taken to be a function of electron temperature. This function is interpreted as the relative floating potential (the floating

potential as measured with respect to the surrounding plasma as opposed to ground):

$$V_f = V_s + V_r(T_e) \tag{3.2}$$

If the electron temperature across the plasma is approximately constant (as will be shown to be the case in DPX), and if no other changes to the background plasma are observed, then the floating potential may be used as a substitute for determining the background electric field. However, if it is known or anticipated that the relationship between the floating and plasma potential will be altered, a more reliable measurement of the plasma potential is necessary.

3.2.2 Emissive Probes

Heated emissive probes can be a more reliable diagnostic for getting accurate measurements of the plasma potential, though their construction is slightly more involved than the simple Langmuir probes. An emissive probe was used to estimate the unperturbed plasma potential profile and changes to the plasma potential in the experiment described in Chapter 4. The probe design was based on a setup used in (Jaiswal 2015[16]). The emissive probe consists of a short, 0.1 mm thick loop of tungsten wire with a horseshoe-shaped segment exposed to the plasma.

As the wire is heated by an electric current, the floating potential increases and asymptotes near the value of the plasma potential (as illustrated in Figure 3.9), allowing for accurate measurements of the potential structure and the electric field. Emissive probes can be difficult to employ in high pressure plasmas as the tungsten wire has a tendency to become oxidized at higher pressures, even when there is only trace contamination by atmospheric gasses in the vacuum chamber (Sheehan 2011[32]). The oxidized tungsten is extremely brittle and the thin probe wires frequently shatter upon re-pressurization. The probe used in

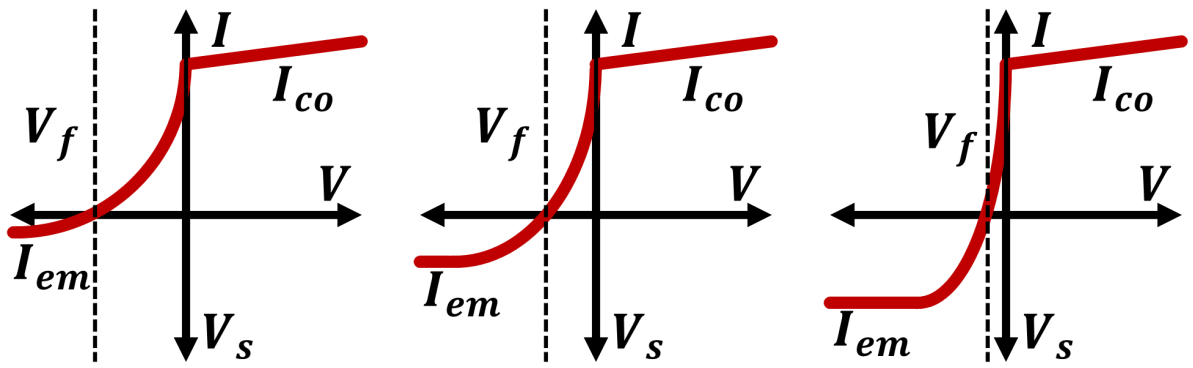

Figure 3.9: An illustration of emissive probe diagnostics. As a heating current is applied to the probe (here the current would increase going from left to right), the emitted electron current, I_{em}, which dominates the collected ion current at lower voltages, increases substantially. As the emitted electron current increases, it shifts the floating potential asymptotically towards the plasma or space potential, while leaving the collected electron current, I_{co}, relatively unchanged. At a sufficient heating current, the measured floating potential can be used as a proxy for the space potential.

the experiment in Chapter 4 was designed so that the exposed wires could be quickly replaced between trials. Analytically there are still outstanding questions about the accuracy of emissive probe measurements at higher pressures.

The heating current for the emissive probe was provided by an Instek GPR-3060D power supply operating in current-limited mode. The probe voltage bias and sweeping voltage were provided by the same Instek GPR-30H10D power supply and Keithley 2400 Series Sourcemeter used for the Langmuir probes.

3.2.3 Probe Arrays

A single Langmuir or emissive probe can frequently be limited to a narrow range of physical positions it can reach. Probe arrays consisting of many single Langmuir probes, arranged in some configuration, allow a wider range of positions to be accessed by probes. Such an array was used to look for indications of spatial variation in the unperturbed plasma conditions. The three-pronged array (dubbed the 'pitchfork probe'), shown in Figure 3.10, consisted of three identical, single Langmuir probes which could be connected to the Keithley

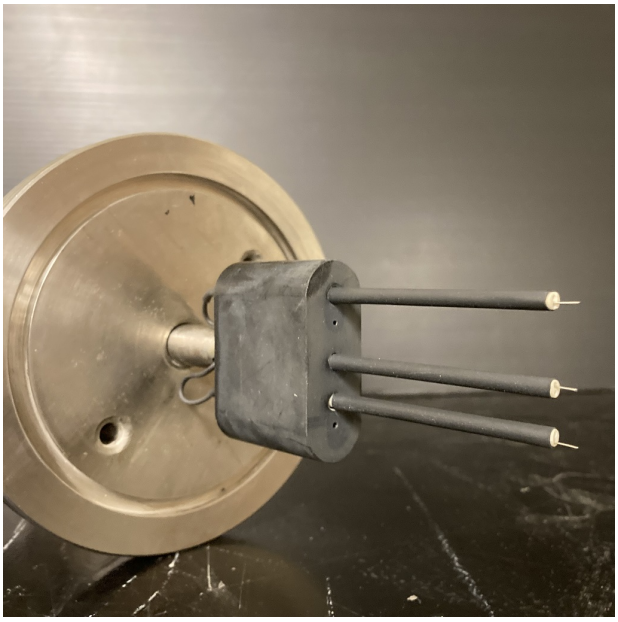

Figure 3.10: The pitchfork probe array used for investigating spatial symmetry in the unperturbed DPX background plasma. The delrin mount holds three identical single Langmuir probes which can be individually biased and swept. The array rotates about an off-center axis allowing points within a two-dimensional slice of the plasma to be accessed.

sourcemeter and biased and swept independently. The array itself was assembled into a smooth, delrin mount which held the individual probes at three different distances from the axis of rotation of the array. By rotating the array about an axis, measurements of plasma properties could be made in a two-dimensional 'slice' within the plasma at the center of the chamber. In principle, three-dimensional measurements could also be obtained by translating along and rotating about the probe axis.

3.2.4 Unperturbed Plasma Conditions

The unperturbed plasma potential, density, and temperature profiles within the DPX are dependent on the electrode configuration and applied biases in each of the experiments discussed in this dissertation. The specific baseline measurements are discussed in their respective chapters, but fall within similar ranges for both experiments and can be broadly described as follows: The electric potential of the anode is typically around 220-230 V for an

applied current from the anode supply of 2.0-2.5 mA. This translates to generating power around half a watt. The confining electrode is generally biased between -50 V to 0 V.

Figure 3.11 shows plots of the measurements made using the pitchfork probe array in the unperturbed plasma. Figure 3.12 and Figure 3.13 show the results of these measurements projected along the horizontal and vertical axes. The projections show that while there is obviously some amount of radially oriented structure for measurements of the floating potential, ion saturation current, and electron temperature - the radial structure is negligible compared to the much more pronounced vertically oriented structure. This near-1D symmetry in the center of the plasma justifies the use of the simpler single Langmuir and emissive probe setups that will be used for the collection of data in the experiments described in Chapters 4 and 5, as well as the justification of quasi-1D models described in the computational work in Chapter 6.

The potential structure in the plasma initially falls off linearly as we move down along the z-axis. One or two centimeters below the center of the primary chamber, as the plasma starts to approach the confining electrode, the potential structure transitions to a more exponential falloff. This is qualitatively consistent with a transition from the bulk plasma closer to the anode to a presheath region surrounding the confining electrode. The ion saturation current (and ion density) decreases linearly moving down away from the anode before exponentially levelling off near the confining electrode. The electron temperature is approximately constant (about 2 eV), with a slight gradient in the bulk and several outliers very near the bottom of the pitchfork probe's range. It is uncertain whether these outliers indicate a sudden jump in electron temperature in the transition to the presheath region, or if, in this region, the presence of the probe is too disruptive to the surrounding plasma to recover reliable estimates of temperature from the probe traces.

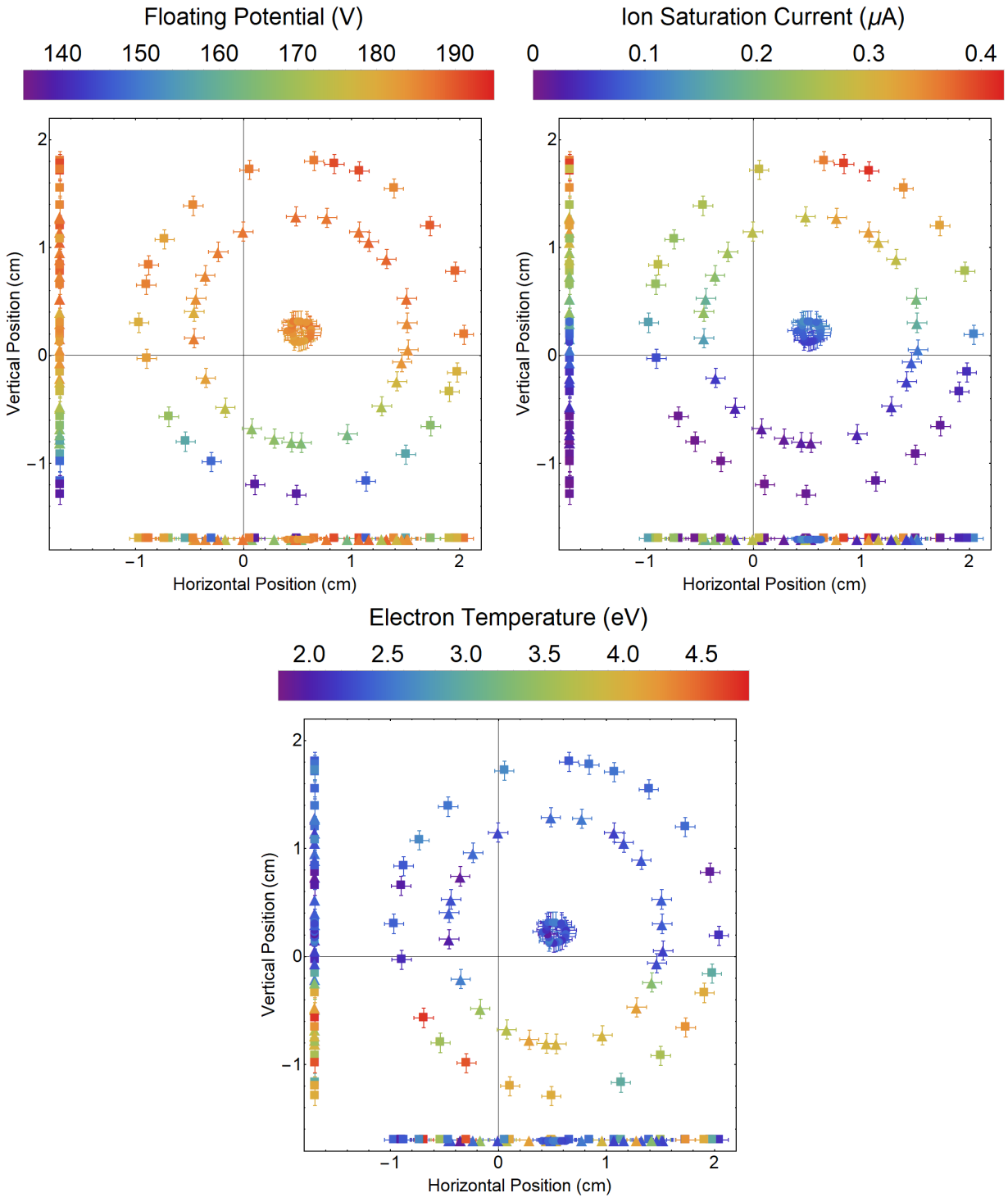

Figure 3.11: Measurements of the unperturbed floating potential (*top-left*), ion saturation current (*top-right*), and electron temperature (*bottom*) taken using the 'pitchfork probe'. The shape of the markers indicates which probe made the measurement, and the color indicates the measurement value. Projections of these measurements onto the horizontal and vertical axes are shown in Figures 3.12 and 3.13, respectively.

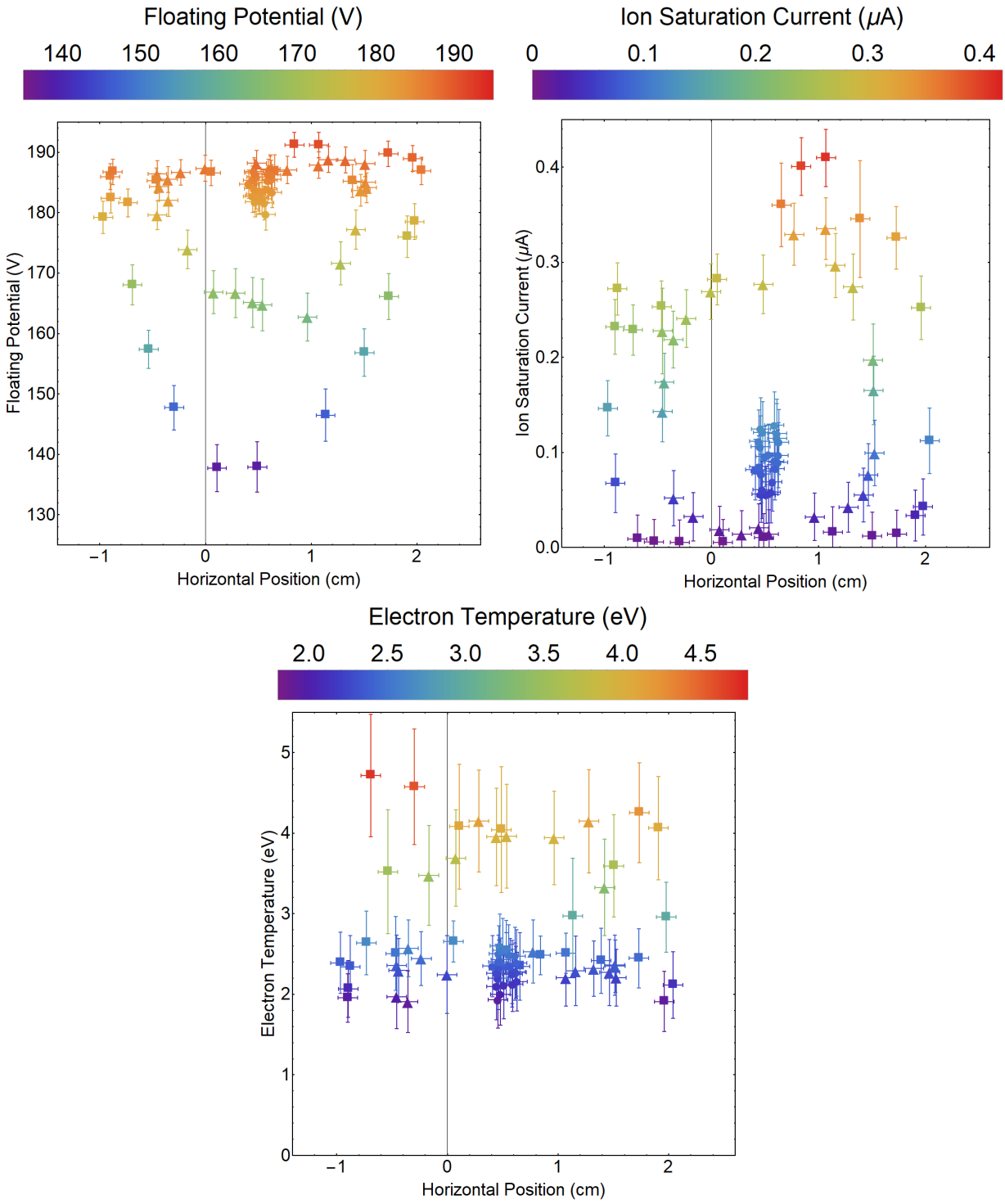

Figure 3.12: Projections of the unperturbed floating potential (*top-left*), ion saturation current (*top-right*), and electron temperature (*bottom*) from Figure 3.11, projected onto the horizontal or x-axis. These projections demonstrate the lack of significant radial variation in the plasma parameters, at least in the regions near the center of the chamber where the dust is suspended.

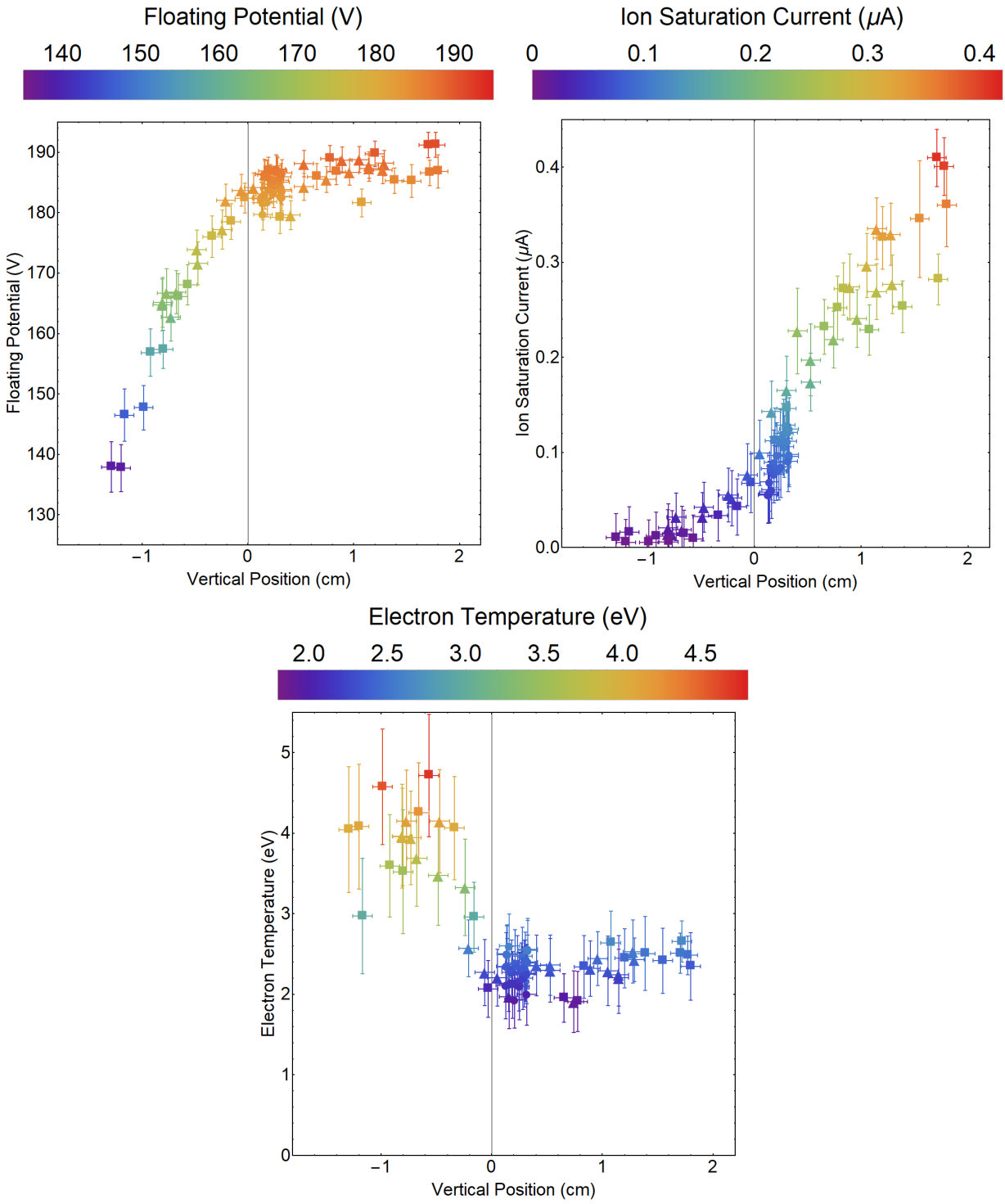

Figure 3.13: Projections of the unperturbed floating potential (*top-left*), ion saturation current (*top-right*), and electron temperature (*bottom*) from Figure 3.11, projected onto the vertical or z-axis. These projections show the variation in plasma parameters is oriented along the vertical axis. This justifies the use of single axis Langmuir and emissive probes and the modelling of the plasma as 1D in later chapters.

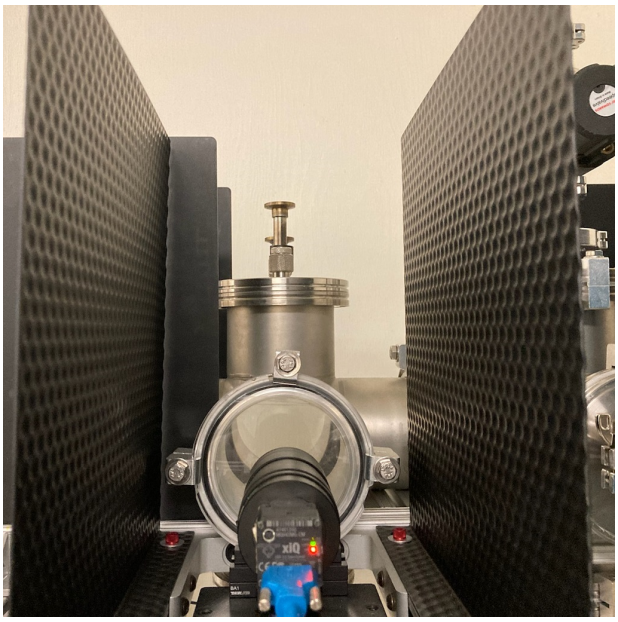

Figure 3.14: A camera-eye view of the exterior of the chamber exterior. A PointGrey Flea3 camera was used in the controlled current fluctuation experiment described in Chapter 4. The Ximea MQ042MG-CM camera (shown above) was used for taking the higher framerate videos in the photo-discharging experiment described in Chapter 5.

3.3 Dust Diagnostics

As discussed in Chapter 1, the macroscopic time and length scales of dusty plasma dynamics provide experimenters with the unique opportunity of making measurements through direct observation. This is accomplished through the analysis of still images or video captured by cameras mounted on the sides of the chamber. The cameras record the behavior of illuminated dust particles and the images are later processed so that information about the equilibrium position of a dust cloud or the instantaneous position, velocity, and acceleration of individual dust particles can be obtained for use in the models described in Chapter 2.

3.3.1 Cameras

All the examination of the dust behavior in the experiments described here is based on analyzing videos captured by a cameras mounted on the front of the primary chamber, seen in Figure 3.14. Two cameras were used in the experiments described in this dissertation.

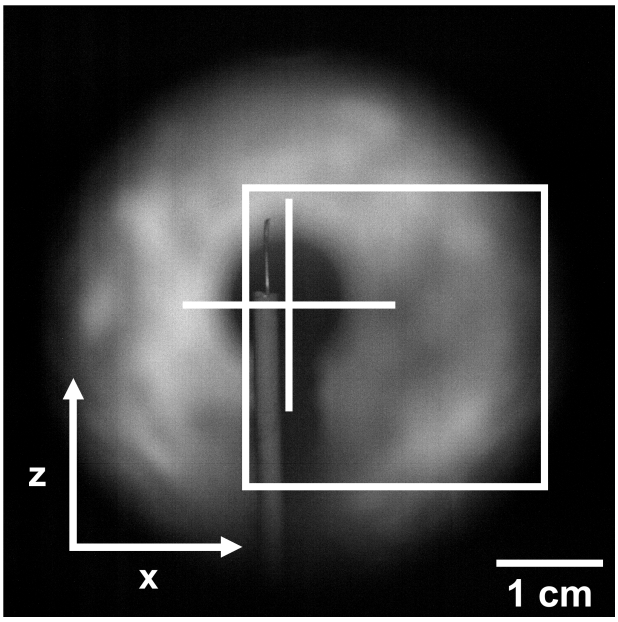

Figure 3.15: Example of the coordinate system used for describing dust and plasma measurements in this research. The x-axis points horizontally through the center of the two chambers towards the right (from the camera's perspective). The y-axis points horizontally through the center of the primary chamber away from the camera. The z-axis points vertically upward through center of the primary chamber. The box indicates the typical region of interest for the dust particles while the cross indicates the approximate geometric center of the plasma chamber.

The first experiment used a PointGrey Flea3 camera at 15 FPS. The second experiment used a Ximea MQ042MG-CM camera at 100 FPS.

A 532 nm continuous-wave laser with an average optical output between 554 to 568 mW is mounted on the side of the secondary chamber. Light from the laser is passed through a cylindrical lens which fans the laser beam out into a plane which can illuminate two-dimensional cross sections of the dust clouds. For the images analyzed as part of this research, we define the following coordinates for the experiment (illustrated in Figure 3.15): The origin is defined to be at the geometric center of the plasma chamber. The x-axis runs horizontally through the center of the two chambers, parallel to the ground, with positive direction pointing towards the right from the camera's viewpoint. The y-axis runs horizontally through the center of the primary chamber and follows the camera line of sight, with the positive direction pointing towards the camera. The z-axis runs vertically through the center of the

primary chamber, perpendicular to the ground, with up being the positive direction. The dust behavior analyzed in later chapters is confined to the x-z plane illuminated by the laser.

3.3.2 Image Processing

In order for information to be extracted from the raw footage recorded during the experiments, the video must go through several steps of processing. The processing is performed in ImageJ/Fiji (Schindelin et. al. 2012[29]). Preparation of the videos for analysis consists of first creating a calibration image using a projection of the minimum intensity of each pixel from the length of a given video and subtracting it from the rest of the footage. Subtracting this calibration image allows us to remove most of the illuminated background (the chamber walls, the electrodes, etc.) from the video, leaving the dust particles as the brightest remaining objects in the processed video. Brightness and contrast are adjusted to make the dust clearer and a Gaussian filter with a smoothing radius of one pixel is applied to the video to give the particles a more radial appearance that can be more easily identified and tracked.

Depending on the parameter of interest for a given video, one of several additional paths may be followed: If the goal is to determine the average equilibrium position of dust in the cloud or observe the paths traced out by particles over time, then the maximum intensity of each pixel over the length of the video is projected into a single image. If, on the other hand, we are interested in measuring the position of a particle over time, then measurements consistent with Particle Tracking Velocimetry (PTV) are conducted. While there are many particle-tracking tools available, including some built into the ImageJ/Fiji program, for the experiments discussed in this dissertation it was decided to track our selected particles manually. Dust particles are free to move in all three dimensions in the plasma, however only a two-dimensional 'slice' of the cloud can be illuminated by the laser at any given moment; thus, it is frequently the case that a particle may leave or enter this plane of visibility, which can lead to misidentification by automated tracking algorithms.

In order to convert data from the pixel coordinates of the videos to real space coordinates within the chamber, a spatial calibration image is produced. From this image a conversion to the real space coordinates can be generated and applied to the position data extracted from the images.

Chapter 4

First Approach: Modification of Existing Charging Currents

Chapter 4 discusses the first method investigated as a means of controlling dust charge - the modification of the existing charge collection currents incident on the dust. The OML charging model (2.13) introduced in Chapter 2 shows how the inherent collection of charge from the surrounding plasma determines the equilibrium charge of the dust. Altering these incident currents must, consequently, alter the equilibrium charge of the dust. If this alteration can be accomplished through some means which minimizes any effect on the background plasma, then this would present a simple and effective way for controlling dust charge.

Section 1 of this chapter lays out the theoretical framework for modifying the charging behavior: Utilizing an oscillating electric field to drive controlled fluctuations in the incident charging currents collected by the dust. Section 2 presents alterations and additions that were made to the baseline DPX apparatus and discusses developing a 'proof-of-concept' test for the controlled current fluctuation concept. Section 3 presents the results of the experiment, and Section 4 discusses the estimated discharge of the dust, the effects on the background plasma, and the efficacy of controlled current fluctuations as a means of controlling dust charge.

4.1 Controlled Current Fluctuation

As discussed in Section 2.1, there are many ways that the inherent ion and electron currents collected by the dust can be altered: Changing the plasma density, temperature, the physical properties of the dust, etc. However, all of these conventional approaches to altering the inherent charging currents require making substantial changes to either the

dust or the background plasma. Since our goal is to avoid making steady-state changes to the plasma, let us consider this question: Can we produce a time-dependent change in the plasma conditions and charging behavior; a fluctuation in charging currents which can lead to a time-averaged change in the dust charge without inducing a time-average change in the background plasma?

4.1.1 Theoretical Motivation

The perturbative coupling between plasma and dust conditions (Shukla 2002, p.61 [33]), and the discrete nature of the charging process (Cui (1994)[3], Goree (1999)[8]) mean that fluctuations in the charging currents are an inherent characteristic of dusty plasmas, and a few detailed theoretical and computational studies have looked at the role that these natural fluctuations may play in the behavior of dust waves (Jana, 1993[17]) and crystals (Vaulina, 1999[43]). However, these types of naturally occurring fluctuations in charging currents are extremely small under the conditions used for most dusty plasma experiments (high densities, low temperatures, microparticles as opposed to nanoparticles, etc.), certainly far too small to observe their effects directly, let alone measurably alter the equilibrium charge of the dust. While inherent fluctuations in the charging currents are not large enough to produce the effects we desire, artificial fluctuations may be.

As was also discussed in Section 2.1, different distribution functions in the plasma species will generate different forms for the charging currents; that is to say, the dust will charge differently in a non-Maxwellian system like a spatially inhomogeneous beam or a magnetized plasma, then it will in a Maxwellian bulk plasma. This is also true of time-dependent distribution functions; the dissipating afterglow of a plasma after the source has been shut off, for example. The shifted Maxwellian distribution discussed briefly in the derivation of the ion drag force in Section 2.2 serves as the source of inspiration for the approach we will take here: If the mobility-limited drift produced by the steady-state electric field produces a change in the velocity distribution of the plasma species, then the drift produced

by an oscillating electric field will produce an oscillating change in the distribution. For parameters like the ion drag, which depend on the direction of the drift motion, the effects of any oscillation or fluctuation in the drift on a short enough time-scale should not affect the time-averaged dynamics of the dust, provided the drift is spatially uniform. However, the scalar charging currents collected by the dust are independent of the direction of whatever drift intersects the dust, and fluctuations may be able to produce a time-averaged change in the dust charge.

We previously stated in Section 2.1 that for ions and electrons with a thermal speed, $v_{ts} = \sqrt{k_B T_s \,/\, m_s}$, we could describe their motion in terms of a thermal Mach number, $M_s = v_s / v_{ts}$. From these definition we defined the the velocity-dependent collection cross sections for the electrons and ions:

$$\sigma_{ed} = \pi {r_d}^2 \left(1 - 2\frac{z_e}{{M_e}^2}\right) \tag{4.1}$$

$$\sigma_{id} = \pi {r_d}^2 \left(1 + 2\frac{z_i}{{M_i}^2}\right) \tag{4.2}$$

We further defined the collection currents incident on the dust as:

$$I_{sd} = \langle q_s \; n_s \; v_s \; \sigma_{sd} \rangle = \int q_s \; n_s \; v_s \; \sigma_{sd} \; f_s(v_s) \; d^3 v_s \tag{4.3}$$

In the derivation of the ion drag in Section 2.2, we stated that for plasma species mobility-limited in a weakly ionized plasma with collision frequency $\nu_{sn} = v_{ts} \,/ \lambda_{sn}$, we could define a thermal mach number for the drift:

$$M_{Ds} = \frac{T_n}{T_s} \left(\frac{q_s \; E}{\sigma_{sn} \; P_n}\right) \tag{4.4}$$

And derive a distribution function for a shifted Maxwellian

$$f_s(v_s)d^3v_s = \frac{1}{\sqrt{2\pi}}\frac{M_s}{M_{Ds}}\left[e^{-\frac{(M_s-M_{Ds})^2}{2}} - e^{-\frac{(M_s+M_{Ds})^2}{2}}\right]dM_s \tag{4.5}$$

The combination of this new form of the distribution function with the derivation of the charging currents above forms the theoretical basis of our new charging model.

4.1.2 Charging in a Weak Electric Field

Combining the OML cross sections with this shifted Maxwellian is challenging. However, a series expansion of the result of the integration can yield analytic expressions for the currents in a 'weak-field' limit where the kinetic energy of the mobility-limited particles is small compared to the magnitude of the electric potential energy of the charges as they approach the dust's surface.

$$\frac{1}{2}m_s{v_{Ds}}^2 \ll q_s\phi_d \tag{4.6}$$

To see if this limit is reasonable, a quick 'back of the envelope' estimate of the conditions which satisfy the weak-field limit can be found by assuming that the electrostatic potential energy of the particles approaching the dust surface is of-order the electron thermal energy, k_BT_e, or in other words that $z_s \sim T_e\ /T_s$. This yields the limiting condition:

$$\frac{1}{2}\frac{T_s}{T_e}{M_{Ds}}^2 \ll 1 \tag{4.7}$$

Or, rearranging this:

$${M_{Ds}}^2 \ll 2\ \frac{T_e}{T_s} \tag{4.8}$$

Using our definition of the thermal Mach number for the drift from (4.4) gives us a limit for the weak electric field:

$$E^2\ \ll\ 2\left(\frac{T_eT_s}{{T_n}^2}\right)\left(\frac{\sigma_{sn}P_n}{e}\right)^2 \tag{4.9}$$

Which, for our low-temperature plasma conditions: T_e ~2 eV and $T_i \sim T_n$ ~0.025 eV puts the limit of a 'weak' electric field at ~12-13 V/cm for the electrons and ~5-6 V/cm for the ions. While this weak-field limit may not necessarily be satisfied for the drifts in the background plasma produced by the strong steady-state electric field (which, incidentally, may account for some of the discrepancies in estimated dust charges in the OML model), it should certainly be satisfied for the time-dependent drift that would be generated by a weaker, oscillating electric field.

In the limiting case of the weak-field, the integration of the OML cross sections with the shifted Maxwellian distribution yields these expressions for the charging currents:

$$I'_{ed} = \left(1 + \frac{{M_{De}}^2}{6}\left(2\ z_e + 1\right)\right) I_{ed} \tag{4.10}$$

$$I'_{id} = \left(1 + \frac{{M_{Di}}^2}{6}\left(\frac{z_i - 1}{z_i + 1}\right)\right) I_{id} \tag{4.11}$$

where the 'un-primed' currents are the original OML currents derived with the standard Maxwellian distribution in Section 2.1. The conditions satisfying this weak-field limit also imply that for the electrons, $M_{De} \ll 1$ and $z_e \sim 1$, and for the ions, $M_{Di} \gg 1$ and $z_i \gg 1$. Given these conditions we can further simplify these expressions for the currents to:

$$I'_{ed} \approx I_{ed} \tag{4.12}$$

$$I'_{id} \approx \left(1 + \frac{{M_{Di}}^2}{6}\right) I_{id} \tag{4.13}$$

For the plasma and dust conditions we expect for our experiment, this modification to the charging behavior suggests that any perturbation to background drifts in the plasma will predominantly affect the ion current. The presence of a background shift, implicitly, must reduce the net negative charge of the dust.

4.1.3 Oscillating Electric Field

Consider an electric field with a steady-state component, E_{DC}, and time-dependent component, E_{AC}, with a sinusoidal form, oscillating at an angular frequency, ω_{AC}, which falls within the regime:

$$\omega_{pd} \ll \omega_{AC} \ll \nu_{in} \ll \omega_{pi} \tag{4.14}$$

where ω_{pd} is the dust-plasma frequency, ν_{in} is the ion-neutral collision rate, and ω_{pi} is the ion-plasma frequency. For $\omega_{pd} \ll \omega_{AC}$, the inertia of the dust particles is too large for the dust to respond directly to the oscillation of the electric field, and the signal should also not produce the kinds of steady-state wake effects seen in the polarity-switching experiments on PK4 experiment on the International Space Station (Thomas, 2018[39]). For $\omega_{AC} \ll \nu_{in}$, we can still treat the ions as mobility-limited and use the same form for the drift motion defined above (2.24), but now with an oscillating drift:

$$M_{Di}(t) = M_{DC} + M_{AC} \sin(\omega_{AC} t) = (\mu_i / v_{ti}) (E_{DC} + E_{AC} \sin(\omega_{AC} t)) \tag{4.15}$$

Finally, for $\omega_{AC} \ll \omega_{pi}$, the electric field is effectively steady-state on the timescale of the ion response, and we can use the same distribution function shown in (4.5) and the same ion currents derived for the case of a constant drift shown in (4.13), but now using this new form for the drift.

Any perturbations to the charging behavior produced by a weak, steady-state field are already factored in to determining the dust's equilibrium charge. The addition of another, weaker, oscillating electric field will not produce a time-averaged change in the net ion drift, nor should it directly lead to a change in net force balance on the dust particles. However, it will still lead to a net increase in the time-averaged ion current collected by the dust:

$$\delta_I = \langle \Delta I / I_o \rangle \approx {M_{AC}}^2 / 12 \propto {E_{AC}}^2 \tag{4.16}$$

If we assume that:

$$E_{AC} \propto V_{AC} \tag{4.17}$$

Then it follows that the relative change in ion current, δ_I should scale like the applied AC voltage squared.

$$\delta_I \propto {V_{AC}}^2 \tag{4.18}$$

Based on this estimate, an oscillating drift with $M_{AC} \approx 1.1$ should increase the incident ion current onto the dust by about 10%, enough to produce a measurable reduction in the dust charge.

The goal of the experiment described in this chapter was to test the validity of this model, and to determine whether oscillating electric fields could be used to reduce the dust charge without radically altering the background plasma. The model presented in this section makes four predictions about the response of dust clouds and Langmuir probe measurements to an oscillating electric field in the described frequency regime:

First, because the collection of current by the Langmuir probe functions in a similar matter to current collected by the dust, we should see a comparable change in the ion current collected by the probe. Second, an increase in collected ions by the dust should produce a noticeable decrease in its net negative charge (its floating potential); this reduction in floating potential (with respect to the space potential) should, similarly, be reflected in the Langmuir probe measurements. Third, if the net negative charge of the dust is reduced, the equilibrium position of the dust cloud must alter in response to this change, moving to a lower vertical position where the electric field is stronger. Fourth, if this method does not alter the background plasma conditions, we should see no change in the Langmuir probe measurements of the space potential or the electron temperature profiles in the plasma.

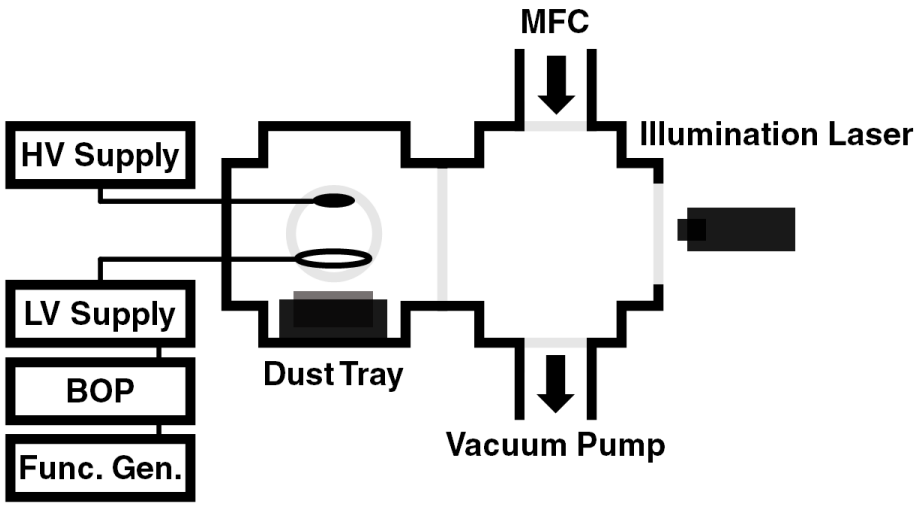

Figure 4.1: Layout of the DPX apparatus for the controlled current fluctuations experiment. The same electrodes and power supplies were utilized, but a function generator amplified by a bi-polar operating amplifier (BOP) produced an oscillating electric field in the plasma.

4.2 Experimental Configuration

As shown in Figure 4.1, the layout out of the experimental apparatus for the controlled current fluctuation experiment was largely similar to the unmodified layout described in Section 3.1, though some minor adjustments and additions were made.

4.2.1 Layout of Primary Chamber

The same 2.9 cm solid brass disk anode and the same copper confining electrode (outer diameter, 4.8 cm, inner diameter, 3.7 cm) that were used in the unmodified apparatus were employed, powered by the same supplies. The anode and confining electrode were located approximately 3.0 cm above and below the geometric center of the chamber, respectively. 2 mA was applied to the anode, producing a bias of $\sim$ 220-225 V, and the confining electrode was biased to -50 V.

With the pitchfork probe measurements confirming that the plasma profiles within the region of the chamber where the dust is suspended are predominantly one-dimensional, the pitchfork probe array was replaced with single axis Langmuir and emissive probes, inserted

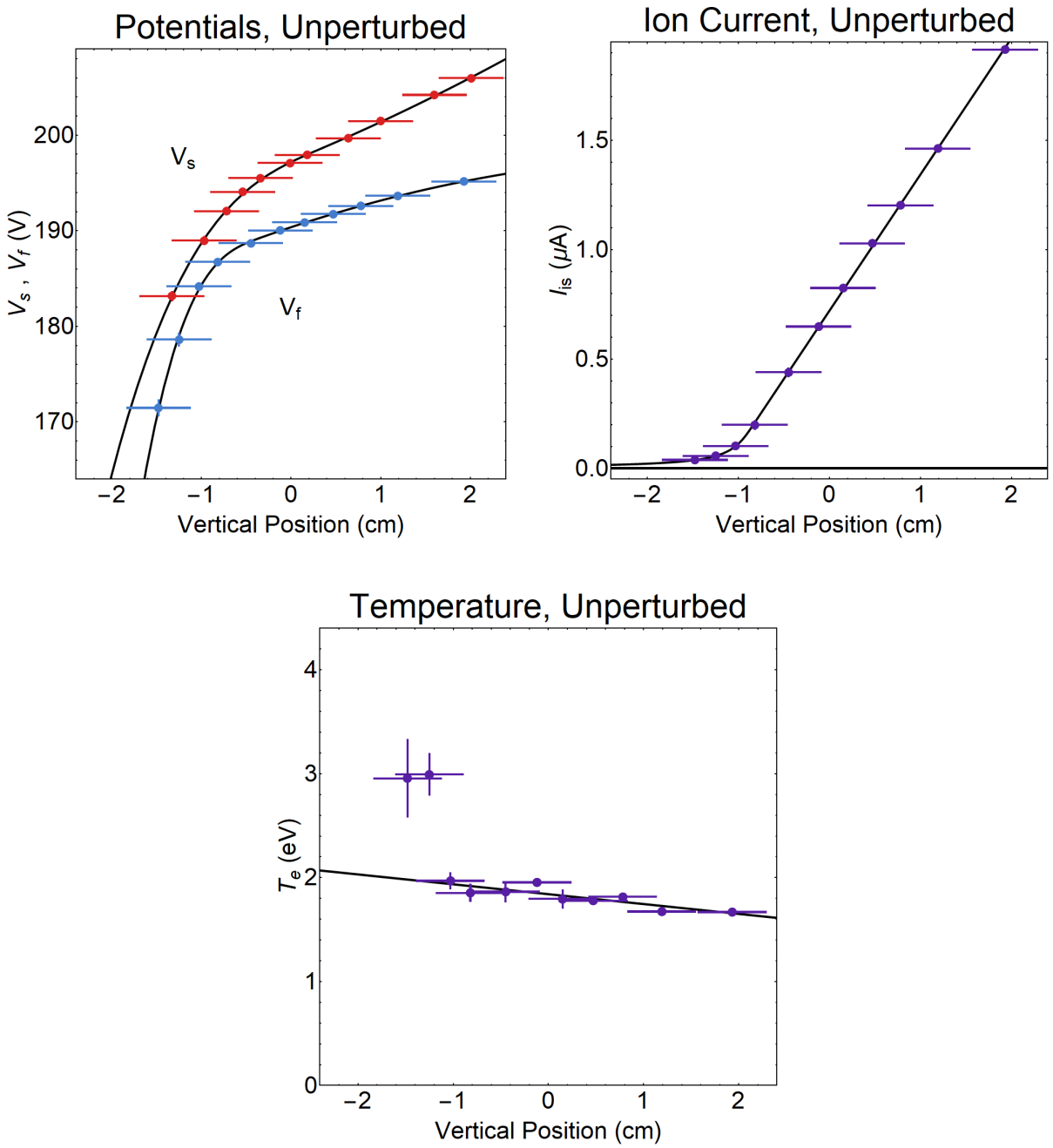

Figure 4.2: The unperturbed profiles for the space potential and floating potential (*top-left*), the ion current, (*top-right*), and electron temperature (*bottom*). The red and blue data points in the potential plot indicate the space and floating potential, respectively. The black lines in each plot indicate the analytic functions used to approximate the profiles (the data and fitted functions from the perturbed plasma profiles follow the same structure).

through the center of the dust tray. The chamber was thoroughly cleansed of any residual dust from previous testing before the plasma conditions were measured. Figure 4.2 shows the unperturbed vertical profiles for the space and floating potentials, the ion saturation current, and the electron temperature. The results of these unperturbed measurements are comparable to the vertical projections of the unperturbed plasma measured by the pitchfork probe shown in Figure 3.13.

The potential structure starts out mostly linear (implying a constant electric field) in the bulk plasma near the anode, falling off (indicating an increasing electric field) as the plasma transitions into the presheath region. The ion current (and, implicitly, the ion density) falls off linearly in the bulk and exponentially in the presheath (the estimated ion density in the bulk was calculated to be $n_i \sim 10^{15}\ m^{-3}$). The electron temperature is roughly constant in the bulk and appears to vary as we transition into the presheath, but given the large increase in uncertainty in the temperature measurements this may be the result of electron current behavior being more sensitive to disruption by the probe in the sheath region. One-dimensional analytic functions are used to fit the unperturbed and perturbed profiles for the purposes of analyzing the dust behavior.

4.2.2 Generating the Oscillating Field

The oscillating electric field is generated by superimposing an AC voltage signal on top of the DC voltage bias applied to the confining electrode which traps the dust. The base AC signal is produced by an HP 33120A signal generator. The generator was used to produce output signals with an peak-to-peak voltage of 10 V_{pp} at frequencies between 10 kHz and 50 kHz. These signals were further amplified by a KEPCO 72-3M bi-polar operational amplifier (BOP). Amplification by the BOP is frequency-dependent, with 10 V_{pp} from the signal generator corresponding to 35.4 V_{AC} at 10 kHz and 7.76 V_{AC} at 50 kHz. The signal generator and amplifier can be seen in Figure 4.3.

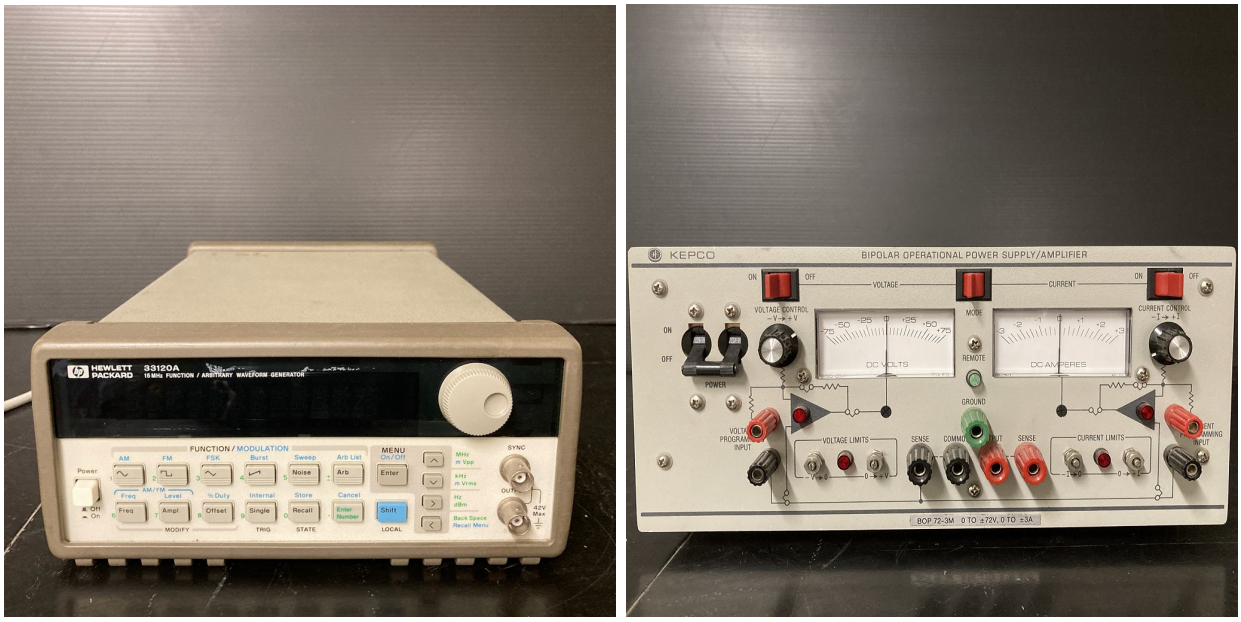

Figure 4.3: For the controlled current fluctuation experiment, an HP 33120A signal generator (*left*) was used to generate sinusoidal voltage signals which were then amplified by a KEPCO 72-3M bi-polar operational amplifier or BOP (*right*). These amplified, oscillating voltages were superimposed onto the existing DC bias on the confining electrode.

The amplified signals are superimposed on the DC voltage bias applied to the confining electrode. It is this signal which is used to influence the dust in this experiment. While the AC voltage applied to the confining electrode is not insignificant compared to the voltage difference between the electrodes, the actual power drawn by the confining electrode at maximum signal amplitude was measured to be between (∼5-10 mW); which is negligible compared to the power typically drawn by the plasma source (∼500-600 mW). The output from the BOP was run in series with the Instek GPR-30H10D power supply which powers the confining electrode to superimpose it onto the existing DC bias used to confine the dust.

4.2.3 Dust Parameters

The dust particles used in this experiment were 2 μm diameter silica microspheres. The particles have an average mass density of $\rho_d = 2200\ kg/m^3$, with an average mass of $m_d \sim 9.2 \times 10^{-14}\ kg$ which are dispersed onto the dust tray before being mounted in the

chamber. The particles are injected into the plasma by drawing an arc from the confining electrode. The clouds formed by the dust are stable, maintaining consistent size, shape, and position for experimental runs lasting several hours.

For the purposes of describing the response of the dust clouds to the applied AC signals, the qualitative or quantitative changes in the observed clouds will be described in terms of the size, shape, and particle dynamics observed, as well as in terms of the equilibrium position of the dust cloud - which we will define here as the bottom edge of the illuminated cross-section of the dust cloud.

4.3 Results

Because probes are inherently disruptive to dusty plasmas (Thomas 2004[37]), the dust and plasma measurements are performed separately. For this experiment the dust measurements are considered first.

4.3.1 Dust Response

After a suitable and stable cloud was generated, various AC signals were applied to the confining electrode and the response of the cloud was recorded for analysis. As the applied signal amplitude increased the following changes were observed: The equilibrium position of the dust progressively decreased vertically, moving closer to the confining electrode, where the steady-state electric field is stronger; the inter-particle spacing between dust grains decreased and the cloud generally decreased in size (however, this was occasionally complicated by the influx of dust from other regions of the plasma); and significantly increased circulation was observed within the cloud cross-section.

The montage of images in Figure 4.4 shows the response of the same dust cloud to a range of AC amplitudes at 10 kHz. Each figures shows a summation of 5 seconds at 15 frames per second. The decrease in the dust cloud's equilibrium position is clearly visible. The decrease in the size and shape of the cloud is also observable, as is the appearance of

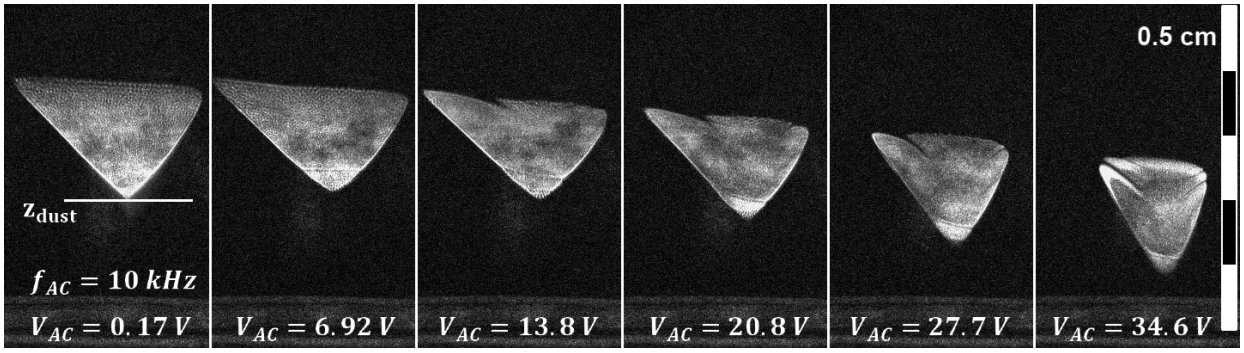

Figure 4.4: Response of a dust cloud to signals with a range of applied voltages at 10 kHz. Each image shows a summation of 5 seconds at 15 frames per second. As the amplitude increases the equilibrium position of the cloud decreases, moving closer to the confining electrode. The cloud can also be observed decreasing in size and evidence of circulation in the cloud can also be seen in the rightmost images (the streaks produced by particle motion over the summation period).

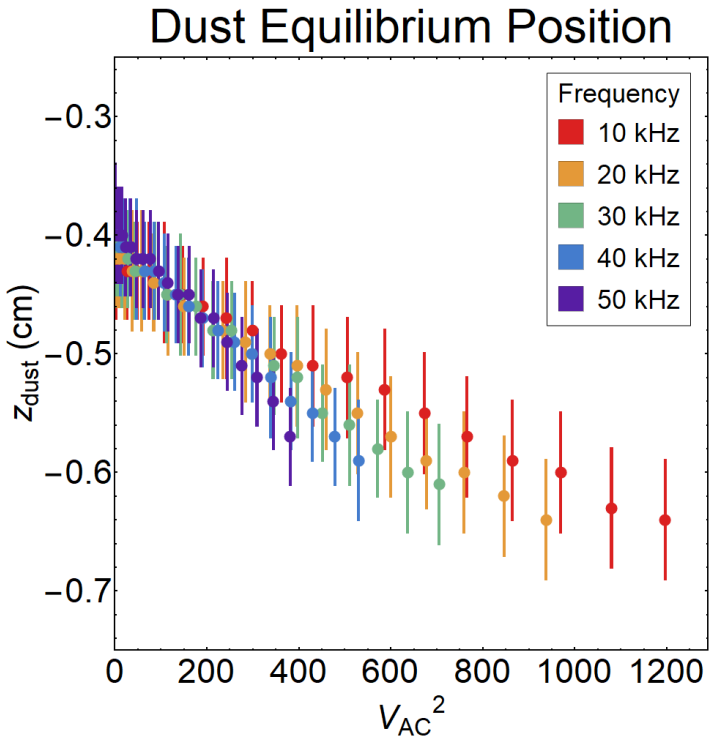

Figure 4.5: The response of the dust's equilibrium position to a range of AC frequencies and voltages. The equilibrium position decreases vertically, up to ~ 0.3 cm below its original position. The strength of the electric field increases as the dust drops and our force balance models would interpret this drop in equilibrium position as a reduction in dust charge.

circulation in the cloud (indicated by the streaks from moving particles in the rightmost image). While this particular trial is not used in the final analysis (this trial lacked the critical emissive probe), the images here are indicative of behavior seen in other trials.

Figure 4.5 shows the response of the equilibrium position of the dust (defined here as the bottom of the dust cloud) in response to increasing the applied AC voltage at 10, 20, 30, 40, and 50 kHz. The dust's equilibrium position decreases vertically in response to the increasing AC signal, up to an observed maximum of ~ 0.3 cm below its original position, approximately a third of the cloud's diameter. Since the vertical electric field magnitude increases lower in the plasma, the Simple and Full Force Balance models would qualitatively interpret this drop in equilibrium position as a reduction in dust charge. The displacement of the dust cloud from its equilibrium position scales like the amplitude of the signal squared and is consistent across the various frequencies up until amplitudes exceeding $\sim 50V_{AC}$, at which point there appears to be some deviation in the dust response.

4.3.2 Probe Response

The applied signals also had effects detected by the emissive and Langmuir probes inserted into the plasma. Figure 4.6 shows the changes in vertical projections of the space and floating potentials, the ion current, and electron temperatures measured by the probes in response to several applied signal amplitudes. The potentials both maintain their general structure, but increases in both the space potential and especially floating potential with respect to ground were seen, with the effect being more pronounced closer to the source of the signal. The ion current collected by the probe, likewise, increased (as was predicted), but this change, too, was not uniform. The electron temperature exhibited no consistent response to the applied signals.

To better see the changes, the perturbed results of the measurements in Figure 4.6 were plotted against the unperturbed measurements to produce a kind of correlation plot for each plasma parameter. The results of this can be seen in Figure 4.7. The horizontal and vertical

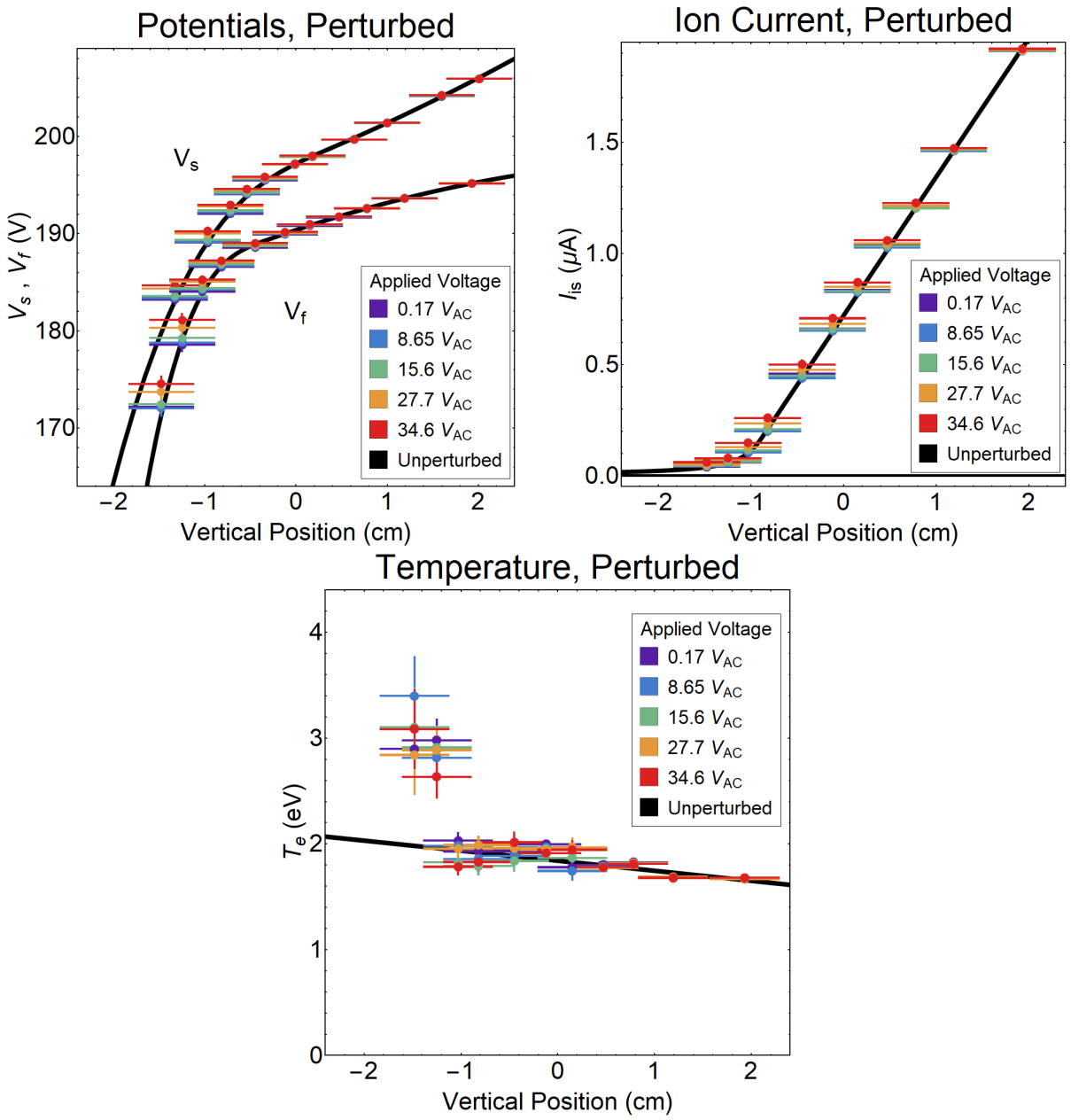

Figure 4.6: Vertical projections of space and floating potentials (*top*), ion current (*bottom-left*), and electron temperature (*bottom-right*) showing the response to the AC signal at several selected applied voltages.

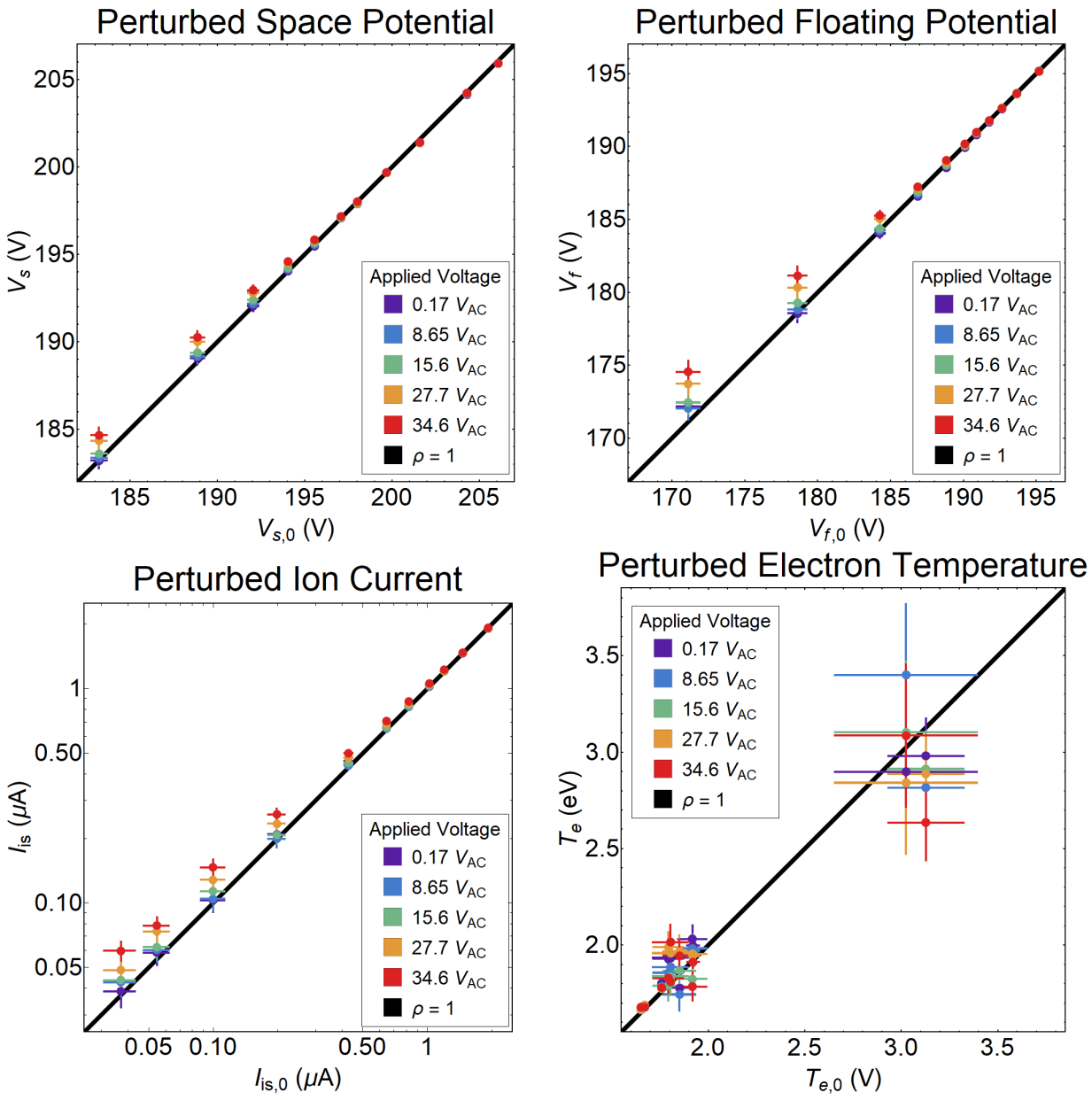

Figure 4.7: The data from Figure 4.6, plotted against the unperturbed measurements from the same positions. The black line running diagonally across each plot shows a line of perfect correlation ($\rho = 1$). As with the data from the previous plot, significant deviation from the unperturbed values can be seen in the space potential (*top-left*), floating potential (*top-right*), ion current (*bottom-left*), while there is less of a clear trend in the data for the electron temperature (*bottom-right*). Since we are more interested in relative changes than absolute changes, the ion current is plotted on a log-log scale to make the changes clearer.

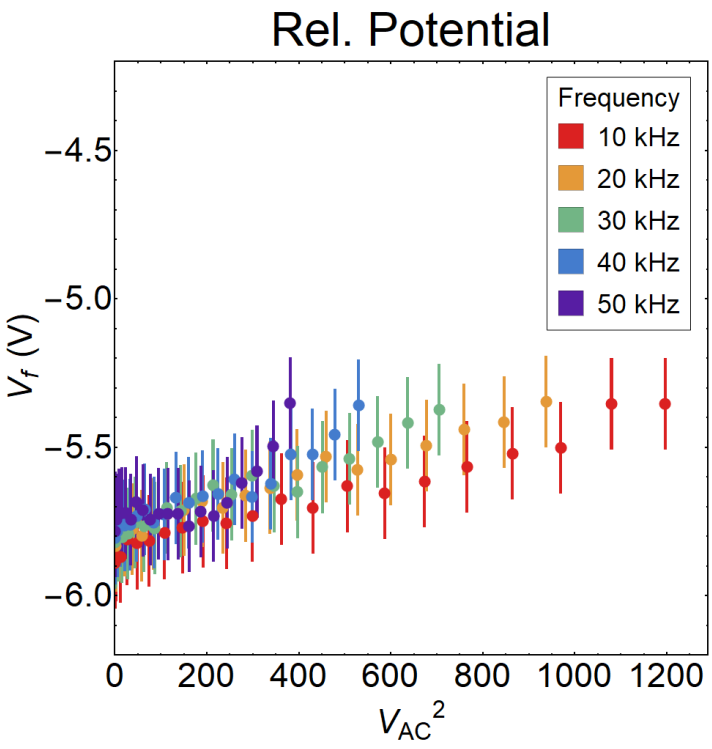

Figure 4.8: The relative floating potential ($V_f - V_s$) that would be measured on the Langmuir probe, interpolated at the dust's equilibrium position. As the AC voltage increases the relative floating potential at the dust's position, which should, in principle, be analogous to the dust charge, becomes less negative.

axes of each plot cover the same ranges on each plot, and the thick, black line running diagonally across the middle of each graph indicates a line of perfect correlation ($\rho = 1$). As with the data from the previous plot, noticeable deviation from the unperturbed values can be seen in the space potential, floating potential, and ion current, while there is less of a clear trend in the data for the electron temperature (*bottom-right*). Despite the changes, the results remain highly correlated with coefficients of $\rho = 0.9166$ for the space potential, $\rho = 0.9638$ for the ion current, $\rho = 0.9801$ for the space potential, and the lowest, $\rho = 0.7976$ for the electron temperature.

Of particular interest to us is not the value of the potentials with respect to ground, but the relative floating potential ($V_f - V_s$) at the position which the dust particles move to. The results of Figure 4.8 show the relative floating potential at the dust's initial position to be approximately -6 V (for a spherical dust particle with a radius of 1 μm this would correspond

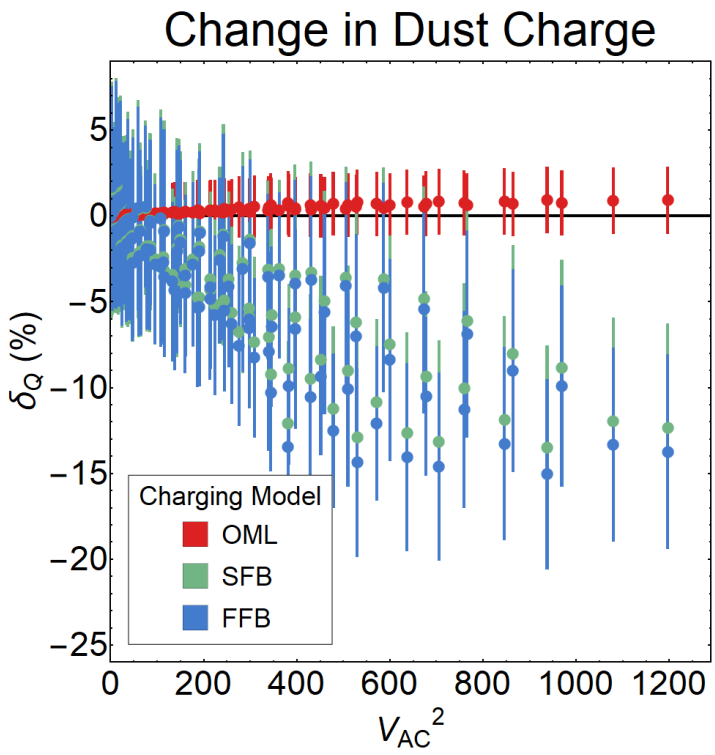

Figure 4.9: The relative change in dust charge ($\delta_Q = \Delta Q_d \ / \ Q_{d,0}$) versus the applied signal amplitude-squared. The force balance models estimated a maximum reduction of $\sim 15\%$.

to a surface charge of $Q_d \sim 4100$ electron charges). As the signal amplitude increases, the magnitude of the relative floating potential is reduced to about -5.2 V ($Q_d \sim 3600$ electron charges). This represents a reduction in relative floating potential of about 15%. These results and the effects on the current are discussed further in the next section.

4.4 Discussion

Our 'proof-of-concept' experiment had two objectives: First, to determine whether the application of an oscillating electric field to the plasma could produce a controlled fluctuation in charging currents, increasing the collected ion current and decreasing the net negative charge. The second was to determine whether this decrease in dust charge could be generated with negligible effects on the plasma.

4.4.1 Estimated Discharge

Qualitatively, the observation of the decrease in dust position shown in Figure 4.5 and the reduction of the magnitude of the relative floating potential shown in Figure 4.8 support the conclusion that there has been a reduction in the dust charge.

The discharge of the dust particles was estimated using the three models outlined in Chapter 3: The orbital motion-limited (OML) charging model which balances the estimated charging currents to find a floating surface potential, and the simple (SFB) and full force balance (FFB) models which balance the estimated forces acting on the particles. The calculated discharges versus signal amplitude are shown in Figure 4.9. No distinguishable definitive change in charge was calculated using the OML model, but the SFB and FFB models both estimated a dust discharge on the order of $\sim 15\%$ in response to the increasing amplitude.

4.4.2 Effects on Plasma

The effects of the AC signals on the measurements made by the probe are relatively straightforward to see - as the results of Figures 4.6 and 4.7 show, the collected ion current is increased, the relative floating potential is reduced, and there is a negligible effect on the electron temperature. These changes are more clearly seen in Figure 4.10, which shows the relative difference (in terms of percentages) of the relative floating potential at the dust cloud's new equilibrium position, and the relative difference in the ion current and electron temperature at the dust's original position, all versus the applied signal amplitude. As predicted by our model, we see a negligible change in temperature, an increase in ion current that scales like the amplitude-squared, and a corresponding decrease in relative floating potential. However, interpreting these results to determine the effects on the background plasma are less clear cut. The change in the space potential with respect to ground is negligible, but the changes are not uniform across the length of the plasma, which means while the potential itself is not changing significantly, the resulting background electric field

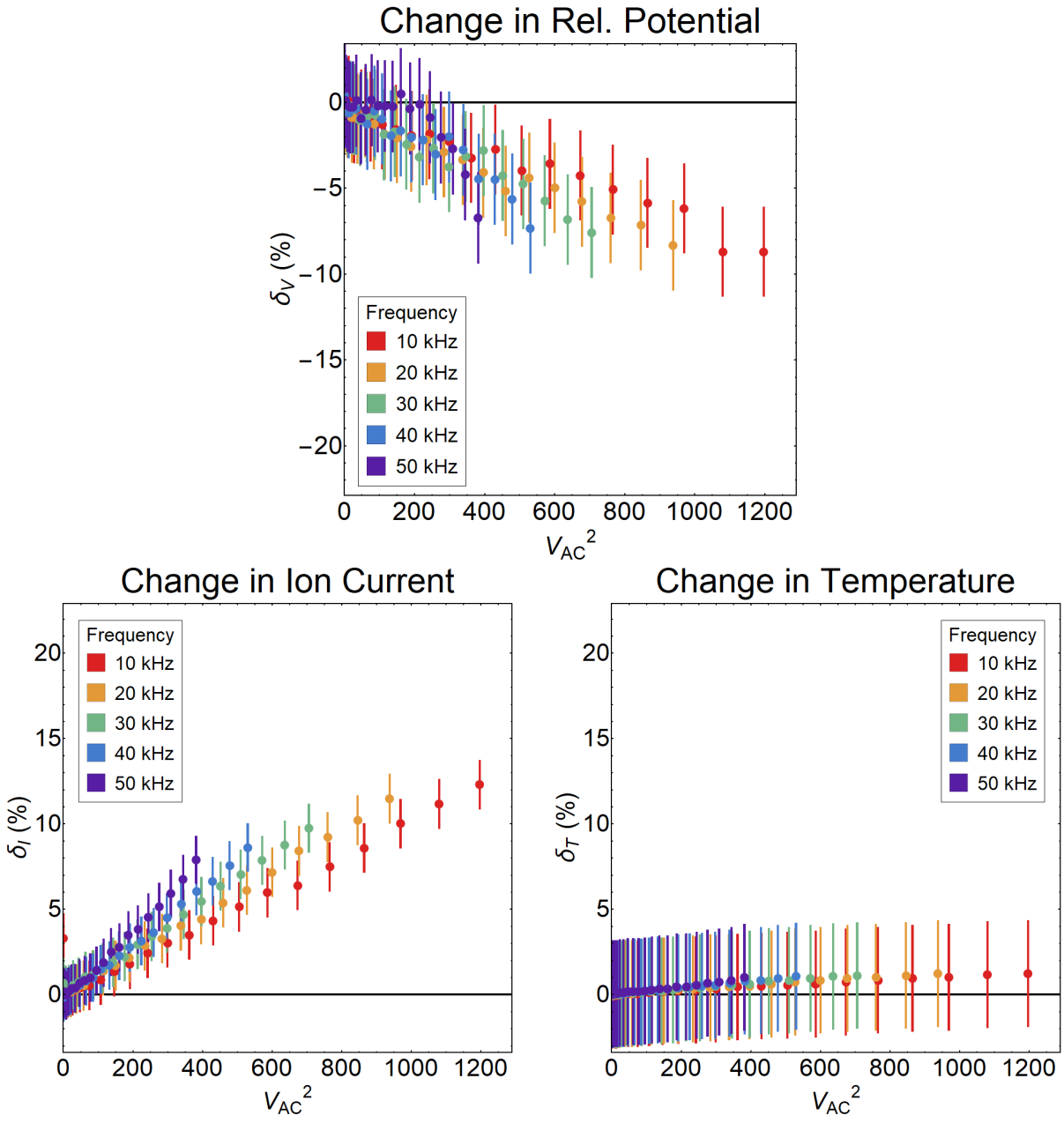

Figure 4.10: The relative difference in floating potential (δ_V, *top*) measured at the new equilibrium position of the dust cloud, and the ion current (δ_I, *bottom-left*) and electron temperature (δ_T, *bottom-right*) measured at the dust cloud's original equilibrium position. As predicted by our models in Section 4.1, the ion current increases like the signal amplitude-squared, the magnitude of the relative floating potential decreases, and the electron temperature is effectively unchanged.

is. We estimate that the electric field at the final equilibrium position of the dust is reduced by somewhere between 5-10%. While this reduction in the background electric field is accounted for in the calculations for the discharge of dust particles, it means we cannot ignore that there are non-negligible changes being made to the background plasma conditions in response to the application of the AC signals.

Determining the effects on the plasma is also complicated by analysis of the ion current. While the response of the current follows the predictions made by our model, the Langmuir probe diagnostics used cannot be used to determine whether or how much of this change is due to a change in the ion distribution or due to an increase in ion density. While the small increase in total power represented by the AC signal suggests it is unlikely that there is a significant increase in ion density, it cannot be conclusively ruled out at this time with the data and diagnostics available.

4.4.3 Efficacy of Controlled Current Fluctuation

The 'proof-of-concept' test for the controlled current fluctuation concept had two goals: to determine whether the application of an oscillating field could produce a net increase in the ion current collected by the dust and reduce the net charge and equilibrium position, and to do so with a negligible change to the background plasma.

While it can be said with certainty that the application of the AC signals was successful in producing a change in the equilibrium properties of the dust, and while the calculated changes in the dust charge and floating potentials (seen in Figure 4.11) both support the conclusion that there was a reduction in dust charge correlated with an increase in collected current, we cannot conclusively say whether the increase in current is due to the controlled current fluctuations we attempted to produce, or a change in background ion density.

We also must concede that this method did not succeed at minimizing its effects on the background plasma. While we were able to confirm that there was a negligible response by the electron temperature profile to the AC signal, the same cannot be said of the potential

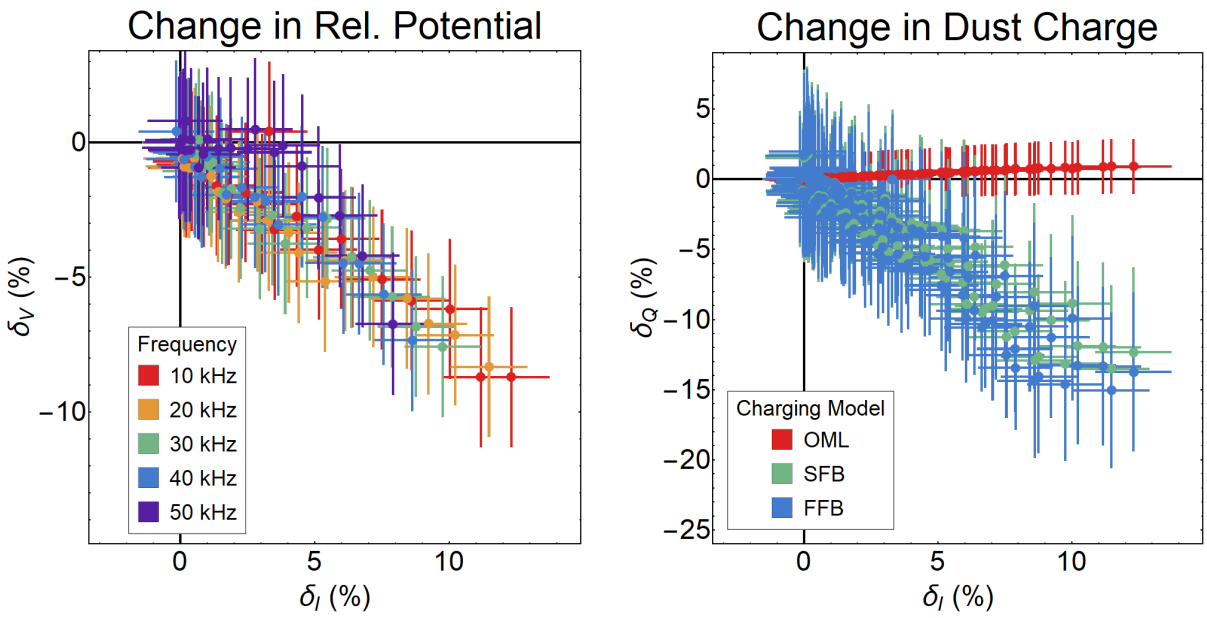

Figure 4.11: The change in relative floating potential at the dust's position, (*left*) and the estimated relative dust discharge (*right*) versus the relative change in ion current at the dust's original position.

profile of the plasma. At a minimum there was a non-negligible change in the background electric field.

There is a great deal about this concept worth following up on. Further refinement of the technique may succeed at minimizing the perturbation of the plasma, and the addition of other diagnostics could answer some of the outstanding questions raised by the results outlined in this chapter; for example, laser-induced fluorescence (LIF) could, in principle, be used to directly measure the response of the ion velocity distribution function to the signal, and look for evidence of the oscillating drift predicted by our model. However, it was decided at this point that alternative methods of altering the dust charge should be investigated.

Chapter 5

Second Approach: Introduction of New Charging Currents

Chapter 5 discusses the second approach for controlling dust charge explored as a part of the research presented in this dissertation: The introduction of new sources of charging or discharging currents to the system. While the modification of existing charging currents explored in the research described in Chapter 4 showed promising indications of altering the dust charge, there was also evidence of significant changes to the background plasma conditions which could not be ignored. Modifying the existing charging currents is non-trivial, difficult to optimize, and is ultimately not-ideal as a means of controlling dust behavior. Introducing a new charging current external to the plasma should, in principle, allow for better control by the experimenter and may present more options for optimizing in order to maximize the effect on the dust while minimizing the effect on the plasma.

Section 1 of this chapter discusses the concept of photo-discharging, inducing a photoelectric current by exposing the dust to UV light. Section 2 presents modifications and additions made to the DPX apparatus and examines the development of a 'proof-of-concept' test for photo-discharging. Section 3 presents the results of the experiment, and Section 4 discusses the estimated discharge of the dust, the effects of the UV on the background plasma, and the efficacy of photo-discharging as a means of controlling dust charge. The results of this research were originally published in the *Journal of Plasma Physics* (McKinlay 2021[23]). This chapter follows and summarizes the results of that work and presents some of the key figures and plots.

5.1 Photo-Discharging

When illuminated by light with a photon energy, E_p, which exceeds the work work function, W, binding the electrons to the material's surface, that material will emit a photoelectric current or photocurrent of electrons. Photocurrents are not an unfamiliar concept in dusty plamas; indeed, photocurrents from starlight represent the dominant charging process of dust particles in the extremely low density plasmas of interplanetary and interstellar space (Spitzer 1941[36]; Goertz 1989[7]), and a handful of experiments have demonstrated the charging of dust using artificial photocurrents in plasmas duplicating these kind of extremely low density conditions (Sickafoose et al. 2000[35]). In these environments, where the extremely low plasma density results in negligible electron and ion collection by the dust, the photocurrent will cause the dust to charge positively. The equilibrium charge or potential of the dust is effectively determined by the balance between incoming light and the material work function:

$$e\,\phi_d \;=\; E_p \;-\; W \tag{5.1}$$

In high pressure, low temperature plasmas (like those found in laboratory or processing plasma apparatus), charging behavior transitions from an energy-dominated regime, to a flux-dominated regime. The higher plasma density results in much larger collections of ions and electrons by the dust particles, and its equilibrium charge is determined by the floating current condition which (in the presence of a large photocurrent) takes the form:

$$I_{ed} \;+\; I_{id} \;+\; I_{pe} \;=\; 0 \tag{5.2}$$

Where I_{ed} and I_{id} are the collected electron and ion currents outlined in (2.5) and (2.6), and I_{pe} is the is the photocurrent. For the negatively charged dust particles found in the laboratory experiments described in our research, it can be safely assumed that any emitted photoelectrons will escape from the influence of the emitting dust particle. Then, for a spherical dust particle comprised of a material with a photoelectron or quantum yield, Y_p,

which is illuminated by a light source with some instantaneous intensity, S_p, and absorbed by the dust particles with some efficiency of order unity, $Q_{ab} \sim 1$, we can estimate the discharging photocurrent as (Shukla & Mamun 2002[33]):

$$I_{pe} = e\left(\frac{S_p}{E_p}\right) Y_p \pi {r_d}^2 \tag{5.3}$$

In principle, photocurrents represent an ideal method for controlling the charge of dust particles: They are a source of discharging current originating from outside the plasma environment, depend only on the energy and intensity of the light source and the material properties of the dust material, and these parameters can be tuned to minimize the effects on the background plasma. The application of photocurrents as a method for deliberately discharging negatively charged dust particles in high pressure, low temperature plasmas, like those found in laboratory and processing plasmas has long been proposed by theorists (Rosenberg, Mendis, & Sheehan 1996[27]), but never demonstrated in any practical experiment, prior to the research presented here.

5.2 Experimental Configuration

For the purposes of this experiment several adjustments and additions to the baseline apparatus described in Chapter 3 were made.

5.2.1 Layout of Primary Chamber

As shown in Figure 5.1, the configuration of the primary chamber for the photo-discharging experiment involved a few changes to the basic hardware and the addition of some new components; however the basic underlying layout is similar to that shown in Chapters 3 and 4. The brass anode from the previous experiments was replaced with a new, solid aluminum disk, 2.8 cm in diameter and 1.0 cm tall. The edge and top of the new anode was covered with a thin delrin cap to ensure that plasma generation was confined to the circular

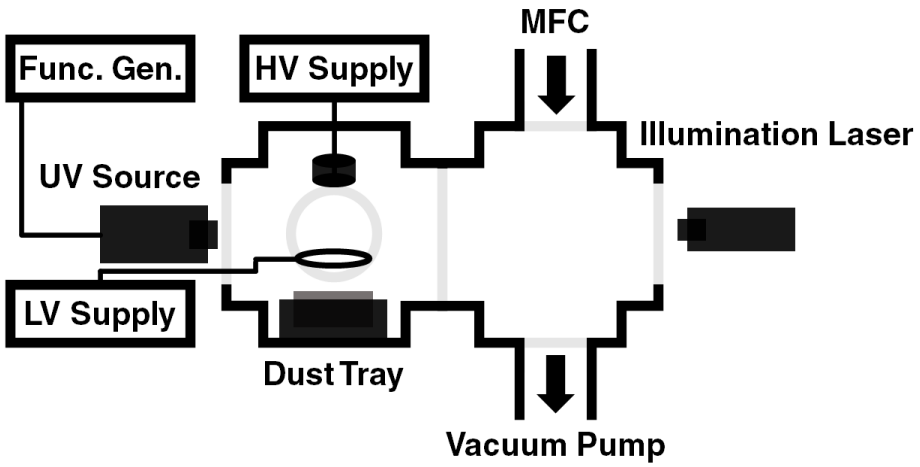

Figure 5.1: Layout of the DPX apparatus for the photo-discharging experiment. A new aluminum anode and a larger confining electrode were added. A window port was added to the left side of the primary chamber to allow access for the UV source, which was connected to a function generator in order to pulse the source.

face facing the center of the chamber. This anode was mounted to the top of the chamber using a threaded aluminum rod connected to the Glassman power supply. A larger, copper confining electrode, with an outer diameter of 8.3 cm and an inner diameter of 6.4 cm was used to encourage the formation of lower density dust clouds in the plasma. The confining electrode was biased to 0 V.

5.2.2 Optimization

In developing a 'proof-of-concept' test for applying photo-discharging to dust, the descriptions of the dust charging behavior from Section 5.1 provided some constraints and guidelines for optimizing the experiment to produce the greatest discharge possible while minimizing the effect on the plasma.

The physics of photoelectric charging give us an upper and lower limit for the photon energy of the UV source used in the experiment. In order to minimize the impact on the plasma, it is necessary to avoid generating photocurrents via the exposure of the chamber walls, instruments, and other components of the experimental apparatus to the light source.

For this reason the photon energy of the source must be below the work function of any of the materials in the apparatus ($\sim 4 - 5\ eV$ for most of the materials in our experiment). This gives us a practical photon energy range for selecting our UV source:

$$W_{dust} \ll E_p \ll W_{apparatus} \tag{5.4}$$

However, this limit severely shortens the list of viable dust materials. Virtually all conventional dust materials like silica or MF are ruled out due to their high work functions and poor quantum yields (Kimura 2016[20]).

Furthermore, the new floating potential condition from (5.2) gives us a second optimization condition:

$$I_{pe} \sim I_{ed}, I_{id} \tag{5.5}$$

In order to have a measurable effect on the equilibrium charge of the dust particles, the induced photocurrent must be comparable to the existing electron and ion currents incident on the dust. Given the estimated discharging current from (5.3), this requires that we find a material which maximizes our quantum yield, and finding a UV source which maximizes our intensity while also satisfying the energy optimization condition above.

Eventually, it was determined that the best choice of dust material for the photo-discharging experiment was lanthanum hexaboride or LaB_6. This ceramic material has a work function of about $\sim 2.7\ eV$ (Torgasin et al. 2017[41]) and an extremely high emissivity (LaB_6 is frequently used as a base or coating for hot cathodes). This choice of material satisfies the two optimization conditions for our experiment, though there are some disadvantages in the choice.

Figure 5.2 shows the LaB_6 dust used in our photo-discharging experiment as viewed using a scanning electron microscope (SEM). Unlike the highly uniform and monodisperse samples of silica used in the controlled current fluctuation experiment described in Chapter 4, the LaB_6 dust is highly polydisperse and irregularly shaped - having an appearance more

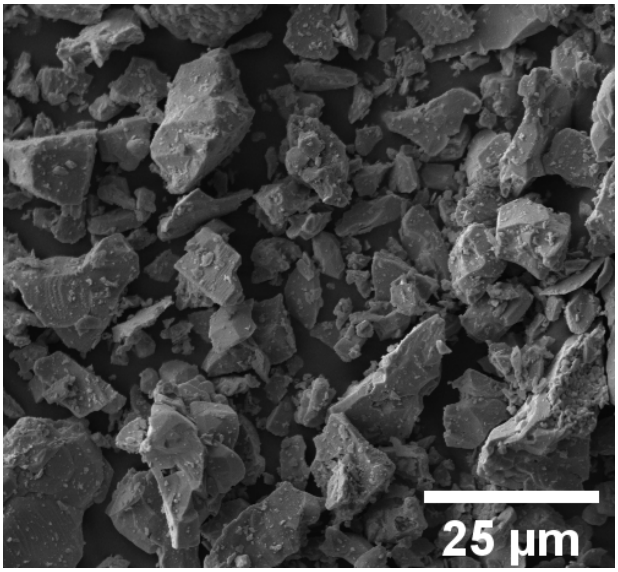

Figure 5.2: Sample of the lanthanum hexaboride dust, as seen under a scanning electron microscope (SEM) 2000X magnification. Unlike the uniform, monodisperse silica microspheres used in the controlled current fluctuation experiment, the LaB_6 dust used for the photo-discharging experiment is highly irregular, with an almost gravel-like appearance, and highly polydisperse, coming in a distribution of sizes.

closely resembling gravel than uniform microspheres. Despite much searching, no provider of monodisperse LaB_6 could be located, and it is uncertain whether spherical LaB_6 dust can be practically produced. The dust samples in the experiment ultimately had to be sieved manually, through the use of a Gilson GA-6 sonic sifter using a series of electroformed test sieves to work the samples from raw powder down to a smaller range of particle sizes that could reliably be suspended in the plasma. Figure 5.3 shows a histogram of the dust sizes found in the various SEM data taken for our LaB_6 samples. In order to estimate what we will describe as a characteristic 'cross-length' (L_d) of the dust, two lines were measured across the image of each particle in the image - one along the longest axis of the dust particle, and one perpendicular to it. The mean cross-length was determined to be 10.77 μm with a standard deviation of 5.42 μm.

For the UV source, various analog discharge lamps were originally tried for the photo-discharging experiment, all producing filtered light in the near UV range. It was ultimately determined, however, that while these discharge lamps produced photons of sufficient energy

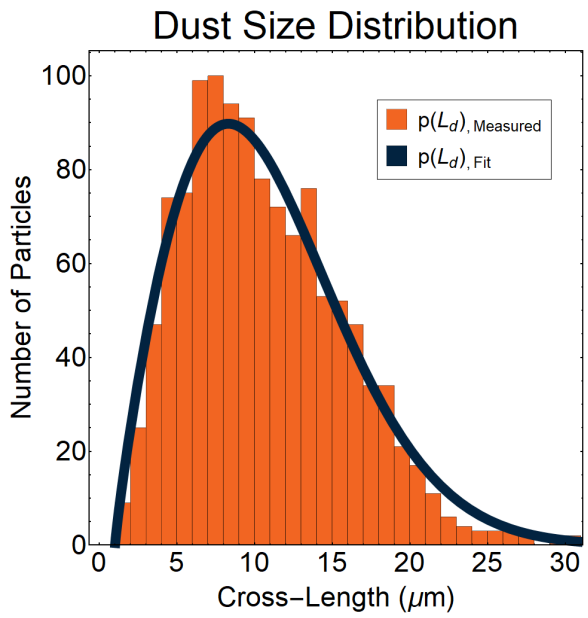

Figure 5.3: A histogram of the dust samples shown in Figure 5.2, showing the probability distribution of dust sizes. The mean cross-length was found to be 10.77 μm with a standard deviation of 5.42 μm.

to produce a photocurrent, they could not produce sufficient intensities to induce a detectable discharge. A more powerful solid-state source, a Solis 365-C high powered microscopy LED with an optical output of $\sim 4W$, was ultimately selected.

The solid-state source had several advantages apart from the significantly higher intensity: The intensity at a given applied voltage is extremely reproducible, and can be changed much quicker than an analog source. Most importantly to our experiment, the UV source could be pulsed through the use of a function generator, allowing us to produce short, reproducible 'shots' of UV in the dust portion of the experiment.

5.3 Results

Different measurements were performed to determine the effects of the high-intensity UV pulse on the properties of the background plasma as well as to determine. In this chapter, we will first consider the effects on the plasma. Probe measurements of the background plasma parameters and the positions of dust particles are made using particle tracking velocimetry

(PTV) with and without the application of the UV pulse. These measurements will show that the UV has little impact on background plasma, but produces a clear and reproducible effect on the suspended dust particles in the experiment. These results will be used in the following section to estimate the discharge of the dust particles.

5.3.1 Probe Measurements

A simple cylindrical Langmuir probe was inserted through a hole in the dust tray and plasma parameters were measured along a vertical line through the center of the chamber (with some minor deviation in the horizontal direction based on the orientation of the probe). The extent of the 2D slice accessed by the Langmuir probe (which is within the same plane illuminated by the laser in the dust experiments) spanned $\sim$0.5 cm across and $\sim$6 cm high.

As with the analysis in the controlled current fluctuation experiment described in Chapter 4, since the motion of the probe is limited to the vertical axis and we cannot measure the plasma parameters at the precise equilibrium positions of every dust particle seen in our experiment, empirical models were, again, fitted to our data for the floating potential, ion density, and electron temperature in order to interpolate measurements of temperature, density, and electric field strength at the position of the dust particles.

The vertical projections of the unperturbed floating potential, ion saturation current, and electron temperature shown in Figure 5.4 exhibit the same broad structures as the unperturbed profiles shown in Chapters 3 and 4. The red and blue data points indicate (respectively) the probe measurements made with the UV source turned off and with the the source on and pulsing at a frequency of 1 Hz with a duty cycle of 50% (0.5 s on, 0.5 s off), while the black curve indicates the empirical function used to fit the data and used for the analysis of the dust behavior in the following section. The integration time for the measurements made using the Keithley was several seconds for each bias voltage in the sweep, so the effects (if any) of the UV source would have been averaged over several pulses. The figures suggest that unlike the experimental results from Chapter 4, there is a negligible

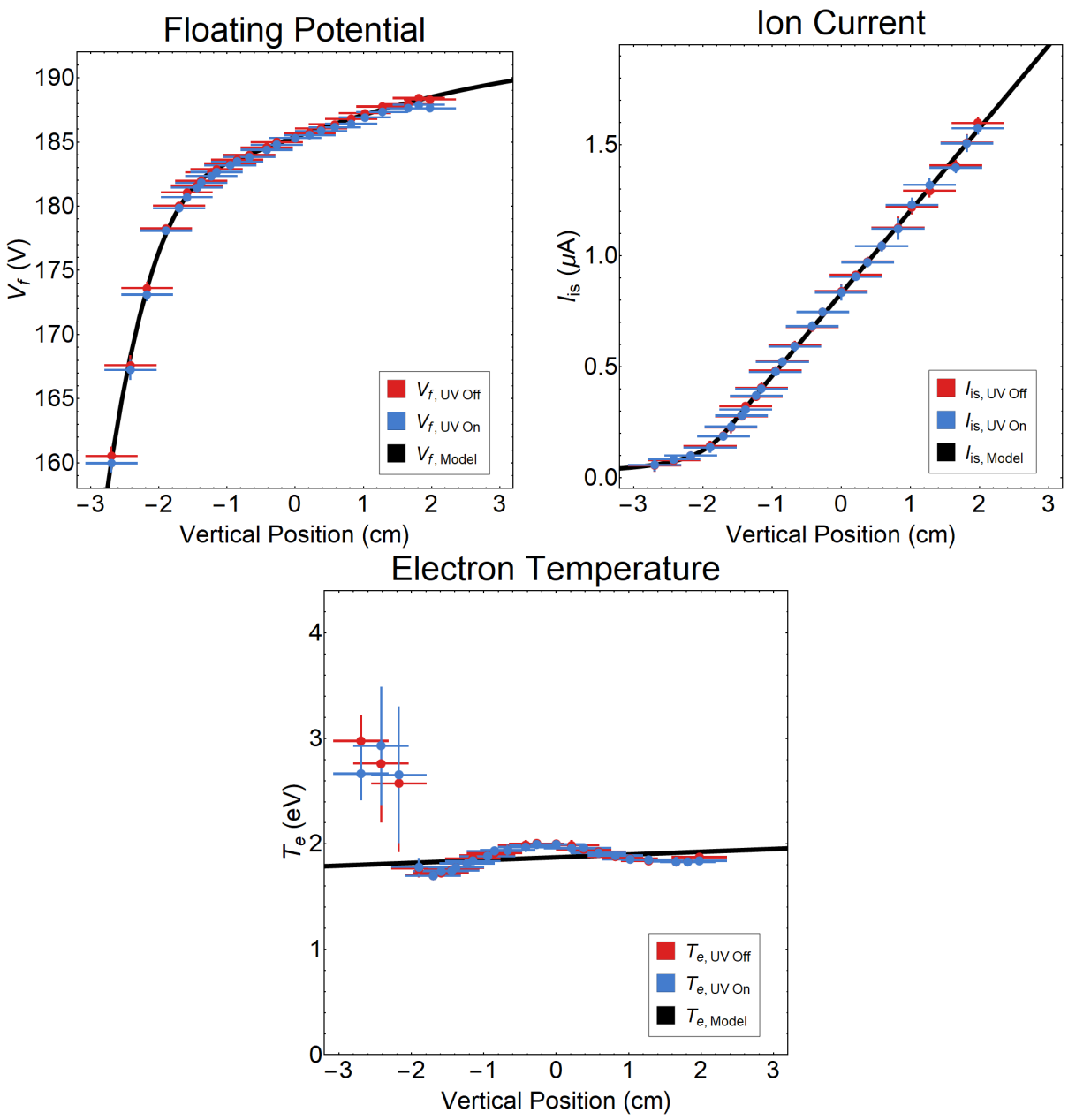

Figure 5.4: Vertical (the previously defined z axis) projections of the floating potential (*left*), ion current (*middle*), and electron temperature (*right*) measurements made by the Langmuir probe, with and without the UV source on. The origin corresponds to the geometric center of the vacuum chamber. The thick black vertical lines indicate the maximum vertical extent of the various dust clouds formed during the different injections in this experiment. The light blue curves show the different functions used for fitting the plasma parameters.

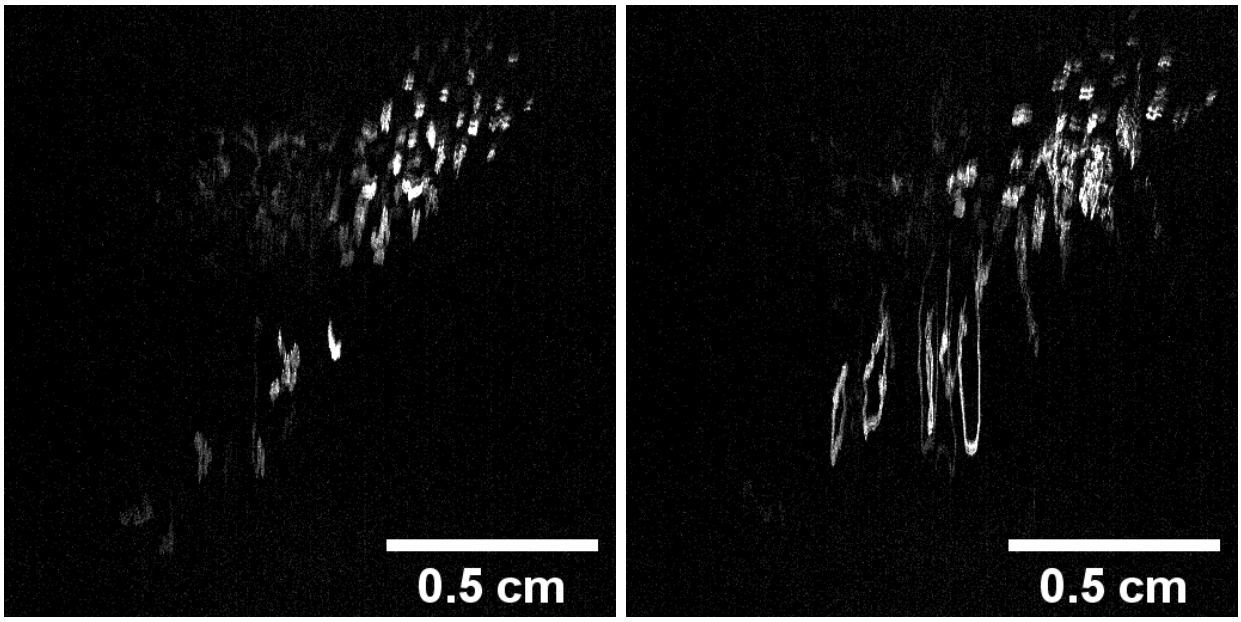

Figure 5.5: Examples of dust clouds without the UV source activated (*left*), and with the UV source (*right*), pulsing at 1 Hz using a 50% duty cycle (0.5 s on, 0.5 s off). Each image in the figure shows the summation of 100 frames or 1 s of video footage (one pulse). The response of the dust to the UV can be divided into periodic-like and chaotic-like behaviors.

change in these background probe measurements in response to the UV pulse. These results are discussed more extensively in Section 5.4.

5.3.2 The Effect on the Dust

The particular size and shape of the unperturbed dust clouds varied with each dust injection; however, in general, in the absence of the UV pulse, the 2D cross section of the dust clouds illuminated by the laser appeared to take on roughly elliptical or triangular shape, indicating an ellipsoidal or conical cloud. The cross section of the main dust clouds were typically 0.5 - 1.0 cm across, with a number density around $10^9 m^{-3}$. The bottom edge of the clouds was generally located at or just below the geometric center of the chamber. Many isolated dust grains were also typically found within the potential trap formed by the confining electrode; near, but still clearly separated from the main cloud.

The images in Figure 5.5 show the response of the dust to the UV pulse. Both images represent a summation over 100 frames of video at 100 fps (the behavior of the dust over

one pulse). The image on the left shows the dust with the UV source turned off, and the image on the right shows the motion of the same set of dust particles over the course of a single UV pulse at 1 Hz with a duty cycle of 50% (0.5 s on, 0.5 s off). In general, the behavior of the dust can be broken into three, qualitatively distinguishable types or classifications of particle motion. When the UV source is turned off, the dust particles undergo small, random motion about a given equilibrium position, which we characterize as stochastic motion. This behavior is likely due to fluctuations in the local plasma parameters and electrostatic interactions between neighboring particles.

When the UV source is turned on and begins pulsing, the behavior can be described as either periodic (exhibiting large, quasi-periodic displacement in-sync with the UV pulse, followed by a gradual return to the dust particle's approximate original position, consistent with a kind of relaxation-like motion) or chaotic (exhibiting large, quasi-random displacements when the UV pulse is on and making their way back to their approximate original equilibrium position when the pulse if off. Particles undergoing periodic motion will settle into a cyclic pattern between two equilibrium points, which can be brought closer together or pushed further apart by modifying the frequency or duty cycle of the pulse so that the dust has more or less time between the UV being on or off.

Particles exhibiting chaotic behavior are highly sensitive to the location and motion of the dust prior to the UV turning back on during each pulse. As a qualitative observation (which will be expanded on in the computational work described in Chapter 6), it has been observed in multiple trials that particles which exhibit smaller stochastic motions when the UV is turned off tend more towards periodic behavior when the UV is on, while particles that exhibit larger stochastic motions when the UV is turned off trend towards chaotic behavior when the UV is on. Figure 5.6 shows displacement data for examples of the stochastic, periodic, and chaotic behavior taken from several different trials.

The vertical displacement of the dust particles in response to the UV pulse appears to be strongly dependent on the intensity of the UV source; when the UV intensity is turned

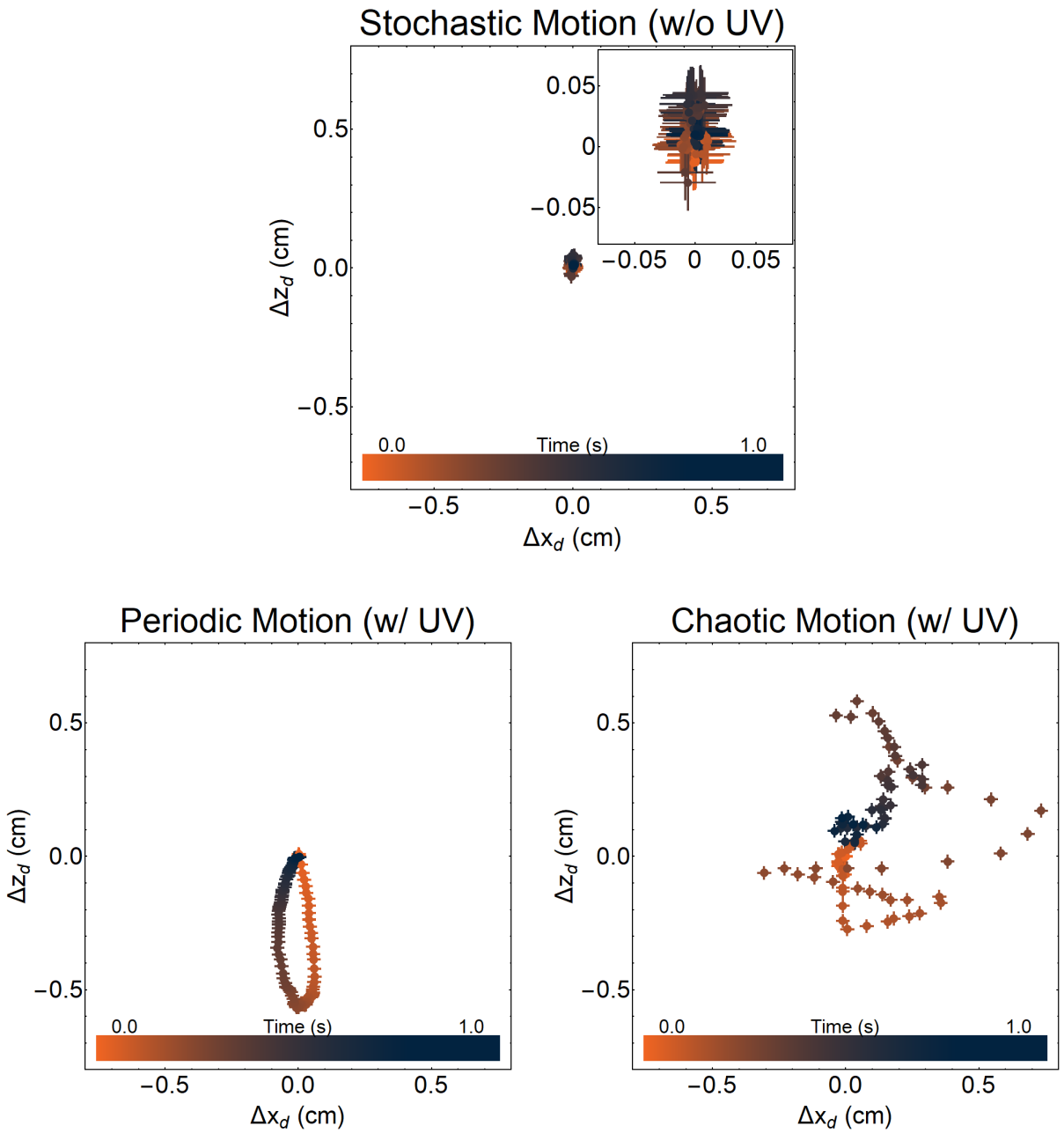

Figure 5.6: Measurements of particle displacement for 1 s without the UV source on (*top*) and over the course of a single, 1 s UV cycle (*bottom*). Dust motion can be divided into three types: Stochastic motion (*top*) characterized by small, random displacements without the UV pulse (the inset shows the displacement magnified); Periodic motion (*bottom-left*), distinguished by large, quasi-periodic displacements in response to the UV pulse; and Chaotic motion (*bottom-right*), characterized by large, quasi-random displacements in response to the UV pulse.

down, the scale of both the periodic-like and chaotic-like motion is much smaller than when the UV intensity is higher. The horizontal motion of the particles was observed to be independent of the direction of the UV source (which would seem to rule out any kind of radiation pressure effect). Particles in many trials were observed traveling towards and away from the UV source. In one especially photogenic trial (shown in Figure 5.7) the particle was observed being ejected from the right side of the cloud and travelling *away* from the UV source, and then a few moments later another particle (or possibly the same particle) was observed reentering from the right and travelling *towards* the UV source while simultaneously exhibiting drops in its vertical position consistent with the periodic-like motion described above. Examples like this would indicate that any horizontal motion the particles exhibit is not due to any direct effect of the UV (like radiation pressure), but are rather the result of indirect effects like changes in the instantaneous forces or interactions with neighboring particles in the cloud.

In addition to the motion described above there is also motion in and out of the plane of the laser sheet. This plane is only a few millimeters thick, which means that particles which are displaced far enough along the viewing axis can 'appear' or 'disappear' from view over the course of a trial. This can considerably complicate the analysis of the particle motion; particle tracking velocimetry can be especially difficult over long periods (especially for particles exhibiting chaotic-like motion in response the the UV pulses) as there is nothing to conclusively indicate whether a particle observed leaving the plane of illumination and a particle observed entering the plane of illumination later in the footage are the same particle or not.

For the purposes of the analysis for this 'proof-of-concept' experiment, it was decided to locate an 'ideal' example of dust motion; a particle was identified near the edges of one cloud which remained within the plane illuminated by the laser for the entire duration of two recording sessions (with and without the UV). Figure 5.8 shows the particle's behavior with and without the UV. Without the UV, the test particle exhibited minimal stochastic

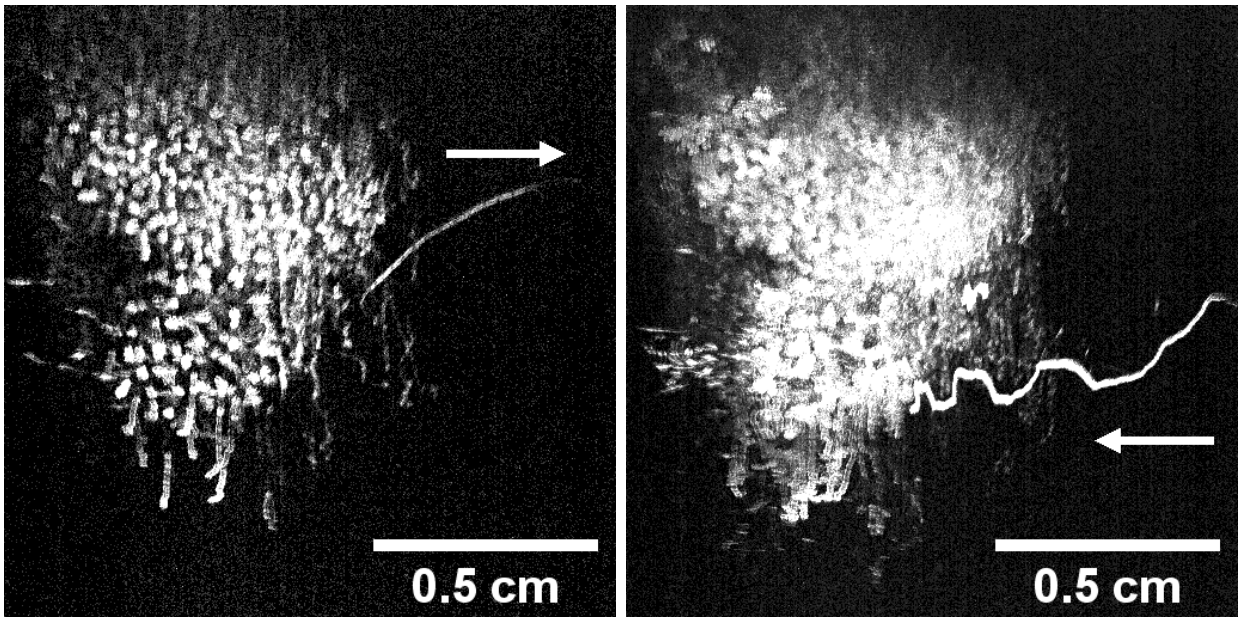

Figure 5.7: A particularly photogenic example of the dust responding the the UV pulses. The arrow indicates the direction of the particle's horizontal motion. UV illumination is from the left side in each image. A particle is ejected from the cloud (*left*) and travels *away* from the UV source (0.3 s elapsed). A short moment later (0.4 s), another particle (or potentially the same particle) reenters the cloud (*right*) travelling *towards* the UV source and exhibiting periodic drops in its vertical position in sync with the UV pulses (3.7 s elapsed). This example not only illustrates the dust's reaction to the UV, but because it also shows that the particles do not exhibit a preference for travelling *away* from the UV source when it is active, radiation pressure can be reasonably eliminated as an explanation for the effects observed in this experiment.

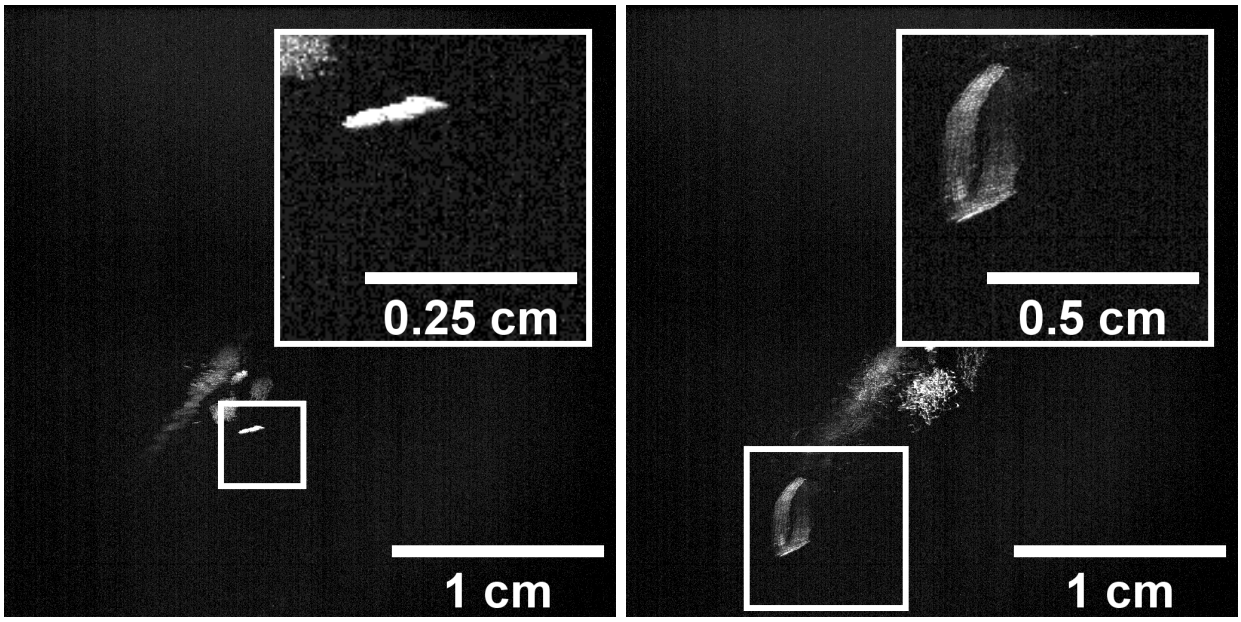

Figure 5.8: The 'ideal' test particle selected for the analysis conducted in this chapter (circled). When the UV pulse is turned off (*left*), the particle exhibits minimal stochastic motion. When the pulse is turned on (*right*), the test particle exhibits extremely regular periodic motion. Each image is a sum of $\sim$ 2000 frames ($\sim$20 s of video), covering 19 pulses. The top-right inset in each image shows the particle's motion magnified.

motion for a period of $\sim$20 s. When the UV was pulsed, the ideal particle underwent highly periodic motion, following a nearly-identical path with each pulse over $\sim$20 s. The selection of this ideal example meant that the results of 19 total shots could be overlaid in order to get an average for the particle's motion over a pulse. The ideal particle's motion is shown in Figure 5.9.

5.4 Discussion

Our 'proof-of-concept' experiment had two objectives: First, to determine whether a UV source could produce a measurable discharge of the dust. Second, to determine whether this discharge could be accomplished with minimal effect on the plasma.

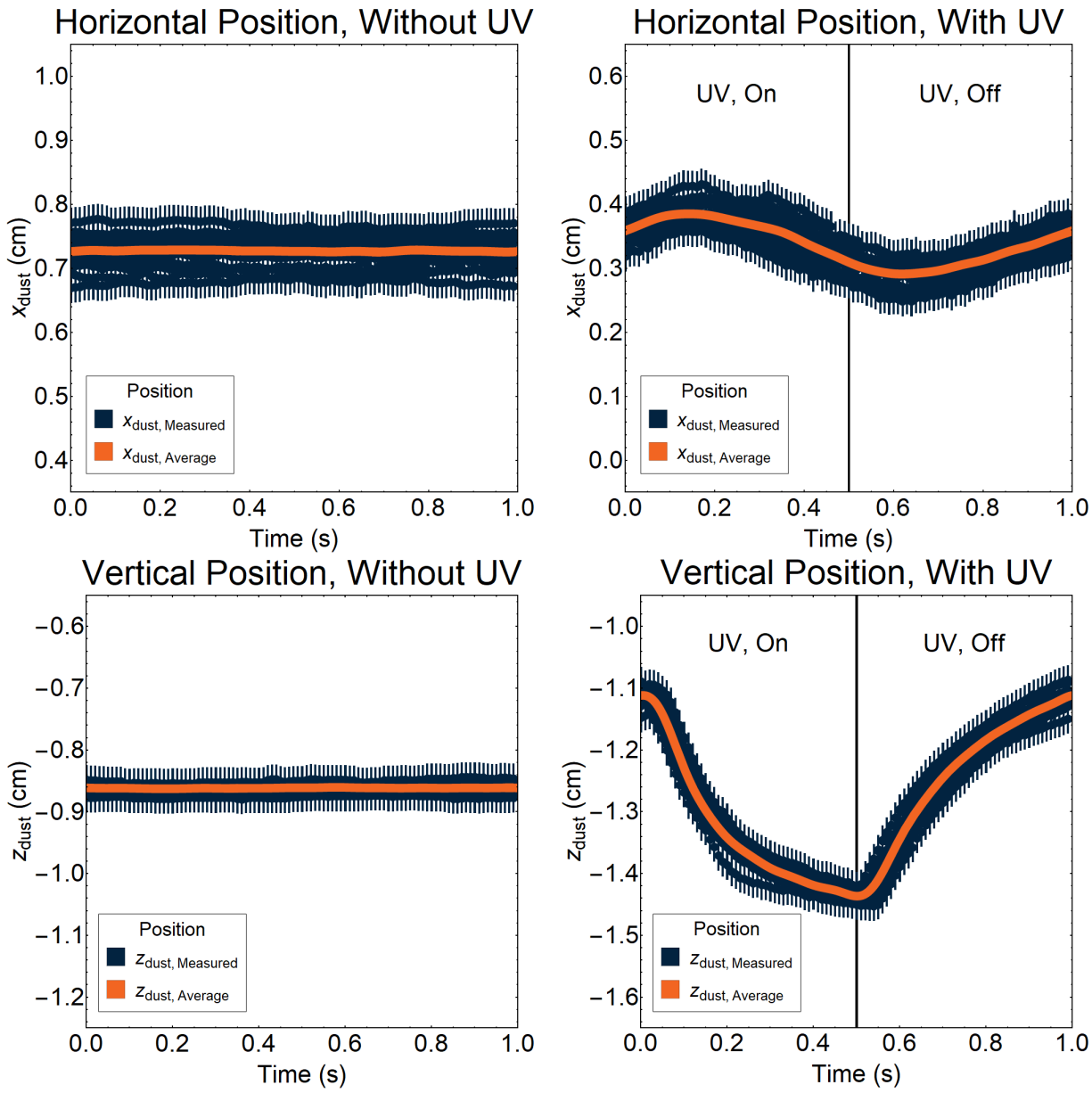

Figure 5.9: The ideal particle's horizontal (*top*) and vertical position (*bottom*) over time, both without the UV source on (*left*) and with the UV source pulsing (*right*) at a frequency of 1 Hz and a duty cycle of 50% (0.5 s on, 0.5 s off). The ∼20 s worth of data from each video is divided into 1 s segments which are superimposed to illustrate the periodicity (or lack of periodicity) of the dust's motion with and without the UV. Without the UV, the particle exhibits only some minor fluctuation in the horizontal direction. With the UV, the particle exhibits periodic-like motion in sync with the pulse.

5.4.1 Minimal Plasma Perturbations

As the previously indicated by Figure 5.4, unlike the experimental results from Chapter 4 there is a negligible change in these background probe measurements in response to the UV pulse. Figure 5.10 shows the results for each plasma parameter with the 1 Hz UV pulses on plotted against the results with the source off. The results are extremely correlated, with coefficients of r = 0.9997 for the floating potential, r = 0.9999 for the ion current, and r = 0.9716 for the electron temperature. The average relative changes in the floating potential, ion current, and electron temperature were, respectively, $\delta_V \sim 0.16\%$, $\delta_I \sim 1.6\%$, $\delta_T \sim 1.3\%$. Based on these measurements, it is reasonable to conclude that exposure to the pulsed UV has a minimal perturbing effect on the background plasma.

While the results above are promising, it was also decided to measure the effects, if any, of constant exposure to the UV on the background plasma. Figure 5.11 shows the relative change in the ion current, δ_I, as measured by the Langmuir probe, positioned at the center of the chamber and held at a particular bias voltage while exposed to constant UV. The black lines indicate the UV source being turned on and off. The response is similarly small compared to the pulsed UV results, appears to saturate after several minutes of exposure, and dissipates quickly once the UV is turned off. It is unclear at this time whether this effect is an actual change in plasma conditions or some kind of charging effect on the probe related to the UV exposure. However, it should be noted that no measurable current was detected by the probe when exposed to UV in a vacuum, so we are confident that this is not a photoelectric current on the probe itself.

5.4.2 Determining Dust Discharge

As in the analysis of Chapter 4, the discharge of the dust was estimated using three methods - the orbital motion-limited charging (OML), simple force balance (SFB) and full force balance (FFB) models. For the purposes of using the models outlined in Chapter 2, the particle is assumed to be a sphere with a radius $r_d = L_d/2 \pm \sigma_d/2$ where L_d and σ_d

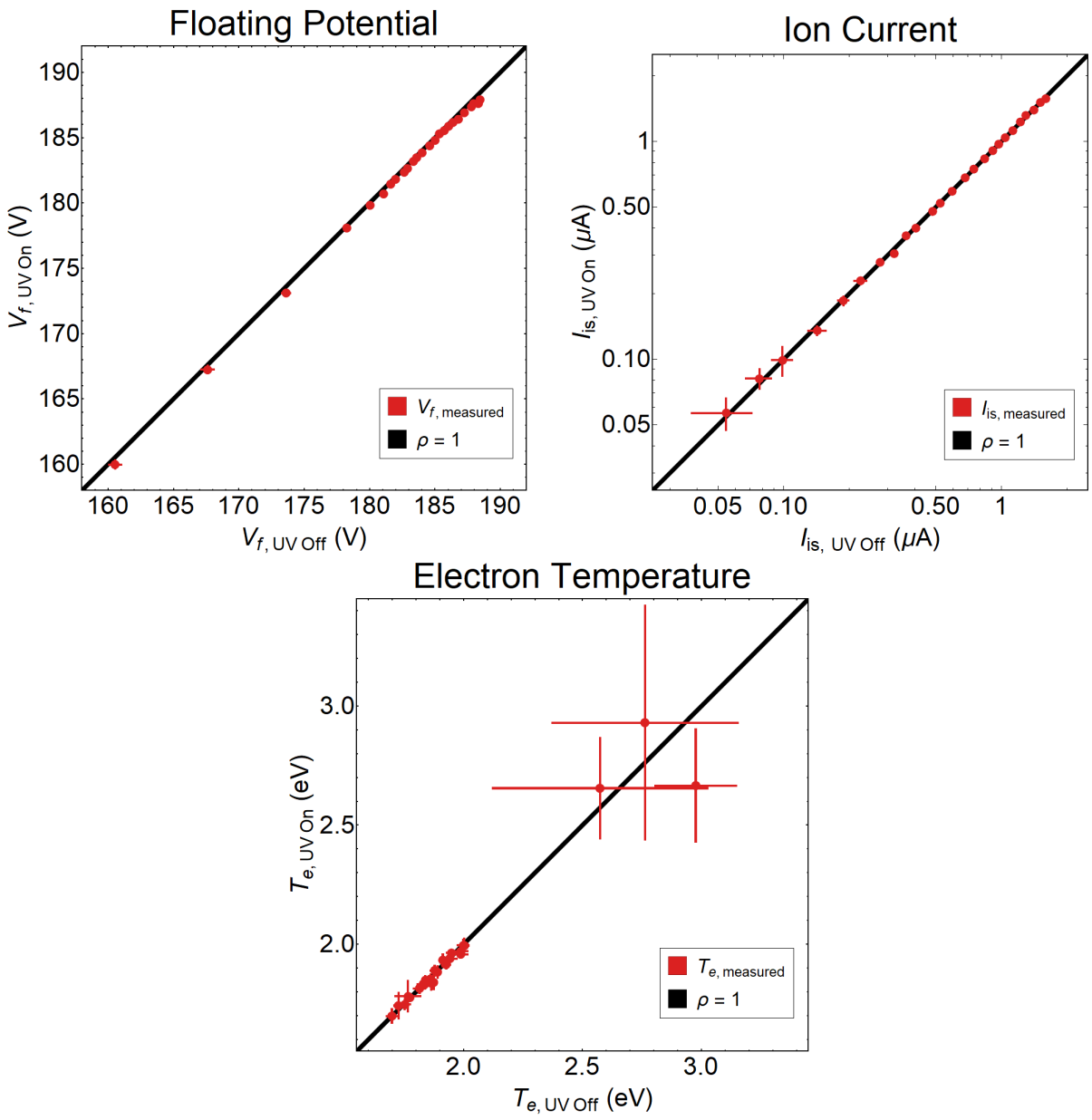

Figure 5.10: The measurements for the floating potential (*top-left*), ion current (*top-middle*), and electron temperature (*bottom*) measurements with and without the UV source pulsing, plotted against one another. As in Figure 4.7, the ion current is plotted on a log-log scale. The thick black line indicates a perfect correlation, $\rho = 1$. All three Langmuir probe measurements demonstrate nearly perfect correlation to one another, and any change or deviation observed in the probe measurements is negligible ($\delta_V, \delta_I, \delta_T \sim 1 - 2\%$).

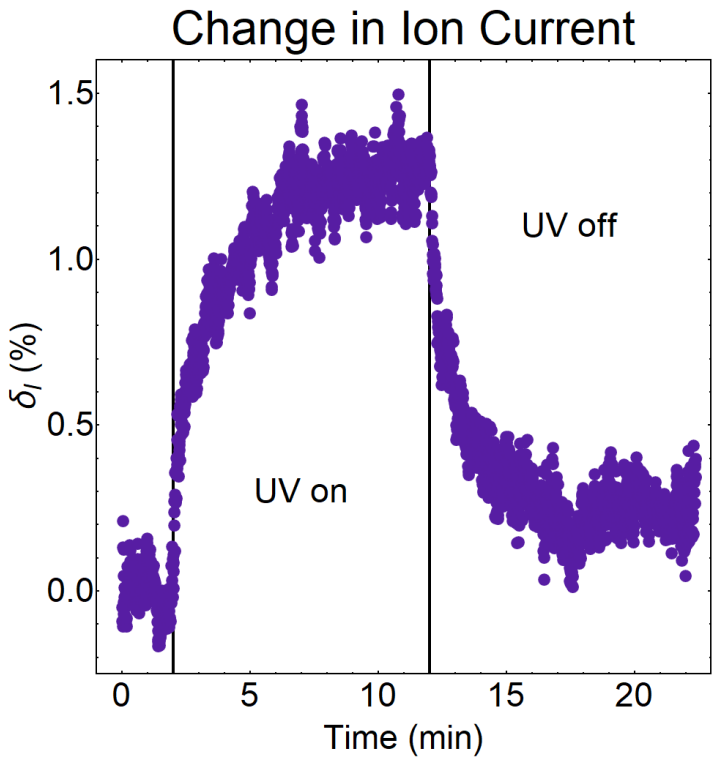

Figure 5.11: Relative difference in ion current, δ_I, measured by the Langmuir probe at a fixed bias voltage in response to long-term constant UV exposure. The black lines indicate when the UV source was turned on and turned off. Even with constant, maximum-intensity UV exposure over a period of 12 minutes, the relative difference in collected current was $< 1.5\%$. The change also drops off exponentially once exposure is terminated.

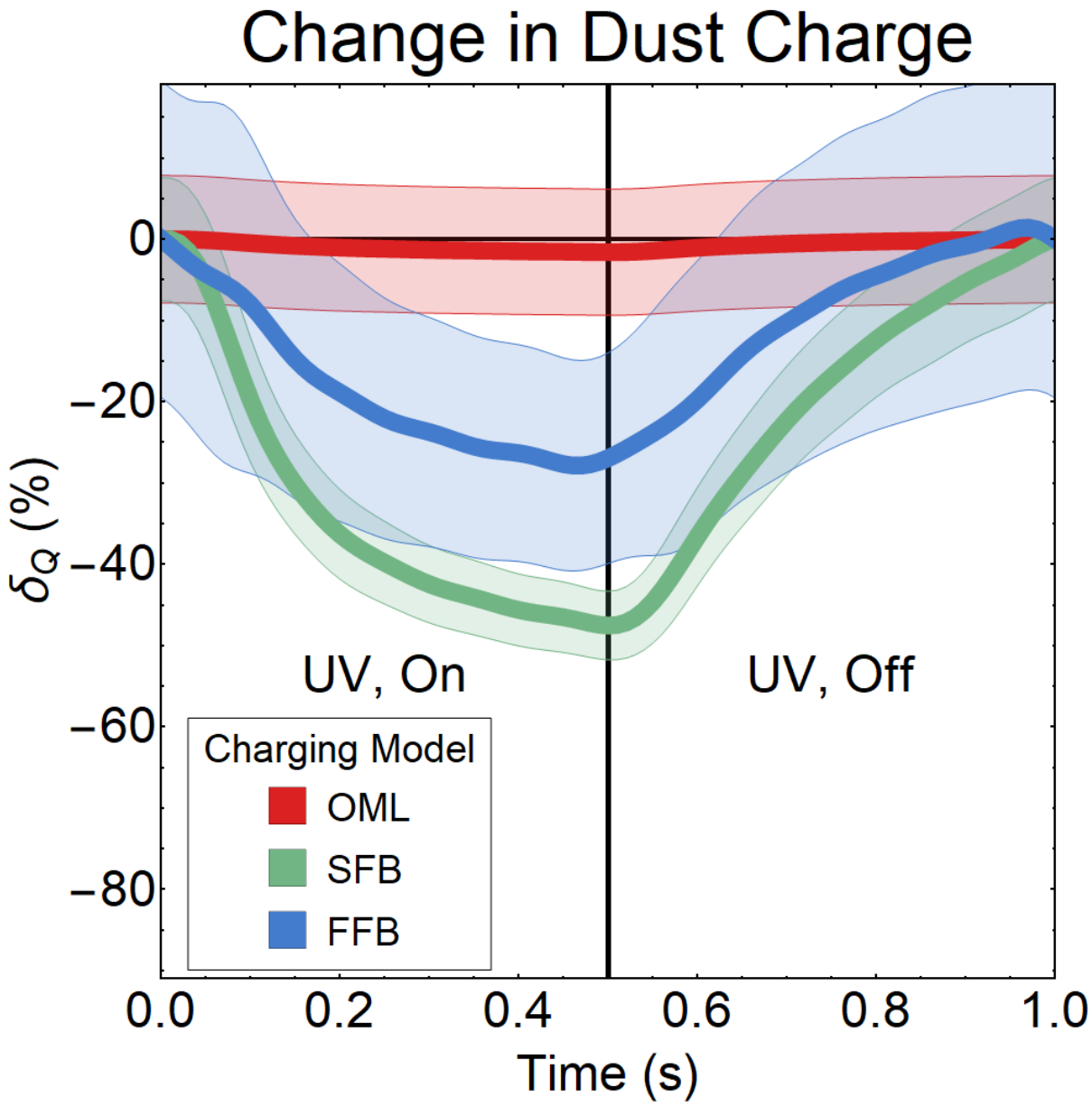

Figure 5.12: Relative difference in the dust charge, δ_Q, calculated using the orbital motion-limited charging (OML), simple force balance (SFB), and full force balance (FFB) methods described in Chapter 2. The different estimation methods produced three different discharge estimates: OML $\sim$ 2%, SFB $\sim$ 50%, and OML $\sim$ 30%. Note that the asymmetry in the discharging and recharging processes.

are the mean cross-length and deviation in cross-length found from the SEM data. Using these figures and based on the OML model the unperturbed dust charge of the ideal particle was estimated to be $Q_d \sim 17000 \pm 8500$ electron charges (the large error arising from the polydisperse nature of the LaB_6 particles). Given this large uncertainty in estimating the absolute charge, it was extremely beneficial to employ the relative change in charge as we did in Chapter 4, effectively removing dust size as a consideration in our models.

Figure 5.12 shows the relative discharge over the course of a pulse, using the position versus time data from Figure 5.9. The maximum discharge of the models varies from model to model (as expected), however they generally follow the same trend: When the UV pulse is on, the charge decreases exponentially, asymptoting to some maximum discharge. When the UV is turned off, the dust appears to gradually recharge, asymptotically returning to its original value. The exponential shapes of the charge difference during these two periods are qualitatively similar to what one would expect to see for a discharging and recharging capacitor. The maximum discharges were estimated to be $\sim 2\%$ for the OML charging model, $\sim 50\%$ for the SFB model, and $\sim 30\%$ for the FFB model.

5.4.3 Efficacy of Photo-discharging

Whereas the results of the controlled current fluctuation experiment in Chapter 4 were impacted by inconclusive probe results, the results of the photo-discharging experiment are clearer: A high-intensity UV source can produce a measurable discharge of particles in a dusty plasma, and there is abundant evidence that careful tuning of the experimental parameters can allow this discharge to be accomplished with no measurable alteration of the background plasma.

Chapter 6

The Effect of Particle Geometry on Photo-Discharging

One of the interesting research questions that emerged from the photo-discharging experiment described in Chapter 5 was the different behaviors displayed by different dust grains in response to the UV source. While some particles, like the ideal test particle selected for the analysis in that chapter, exhibited clear, highly periodic changes in position in response to the UV pulses, others exhibited chaotic and unpredictable changes in displacement and motion. Both types of behavior are correlated to exposure to the UV source, and since the pulses themselves are identical it is reasonable to infer that one or more properties of the dust particles themselves are responsible for the different behaviors. This chapter examines one possible explanation for this behavior and explores the question through computational simulation of dust charging. Section 1 introduces a hypothesis on the effect that the geometry of the dust particles, specifically with regards to asymmetry, has on the charging behavior. Section 2 outlines the construction and assumptions of the computational model used in the study. Section 3 examines the results of the simulations. Section 4 discusses the implications of these simulations and outlines possible experimental research that could followup this work.

6.1 Theory

The hypothesis examined in this chapter is that the geometry of the dust particles themselves is responsible for the tendency for some particles to respond to the UV pulses with periodic behavior while others respond with more chaotic behavior. Unlike the controlled current fluctuation experiment described in Chapter 4, which used highly monodisperse

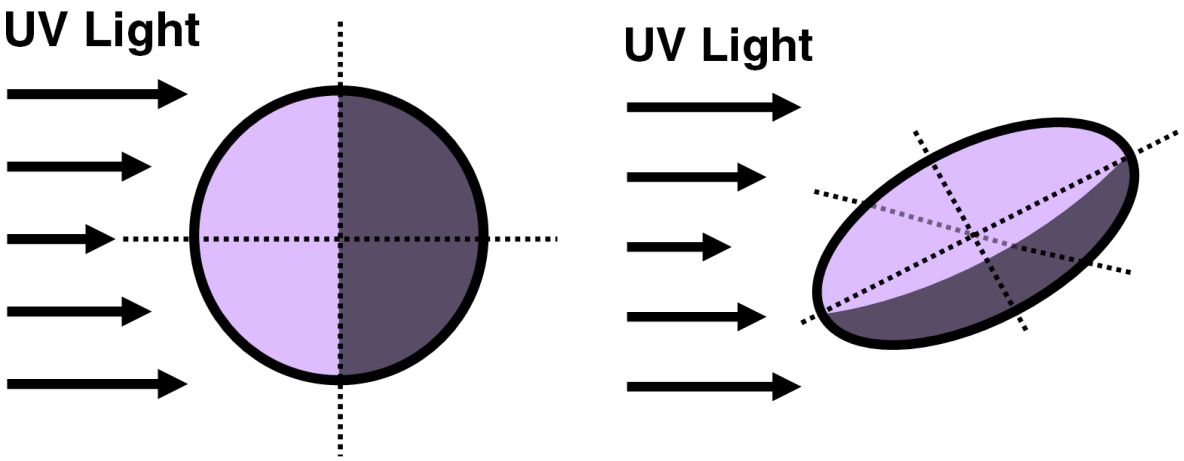

Figure 6.1: Simple illustration of the geometry hypothesis: A perfectly or nearly spherical particle (*left*) will have half of its surface area illuminated when the UV source is on, and the projected areas of the illuminated region remains constant regardless of the particle's orientation. For an ellipsoidal particle (*right*), which has some asymmetry, half of the surface is still illuminated, but the projected area of the illuminated region changes depending on the orientation of the particle (the dotted lines here show the particle's roll, pitch, and yaw axes). If the photocurrent, and therefore the scale of the photo-discharge, is proportional to the projected area, then the discharge is now a function of the particle's orientation.

microspheres, the photo-discharging experiment described in Chapter 5 used a highly polydisperse sample of particles with a wide range of irregular convex (and even concave) shapes, as shown in the SEM images in Figure 5.2.

Unlike the inherent charging currents which the dust collects from the surrounding plasmas, the photoelectric current which discharges the dust is directional - electrons are only discharged from the illuminated side of the dust, which is exposed to the UV photons. The total electric charge discharged from the illuminated parts of the dust is dependent on the projected area of the particle along the light's line of sight. As illustrated in Figure 6.1, for highly symmetric dust particles (like the silica microspheres), this projected area is a constant; each pulse should, in principle, produce an identical discharge each time. However, if the particles have some degree of asymmetry, then as the particles rotate about their various principal axes as they translate within the plasma, the projected area illuminated by the UV will change. This implies that the photoelectric current is now a function of the orientation of the individual particle, and that the discharge produced will change from pulse to pulse.

If the projected area along any given vector are varying with time, this would further imply that any forces dependent on such projections are also functions of time: The neutral drag force is generally taken to be proportional to the area projected along the direction of the particle's instantaneous velocity, and the ion drag force is generally taken to be proportional to the area projected along the direction of the local ion flow in the plasma (the direction of the local electric field), as well as depending on the instantaneous charge of the dust.

Thus, for any irregularly-shaped dust particle, their dynamics in response to the UV pulses is highly nonlinear and extremely sensitive to the specifics of the particle's geometry and initial conditions. This nonlinearity could explain the complex and chaotic behaviors observed in the photo-discharging experiment. To explore this hypothesis, a simple, single rigid body simulation was developed to explore the potential effects of particle asymmetry.

6.2 Computational Model

In this section we discuss and justify the primary conditions and models imposed for the simulation, beginning with the geometry of the simulated particles:

6.2.1 Conditions, Assumptions, and Approximations

In principle, we could try to simulate virtually any number of irregular particle shapes, even shapes as complicated as the actual particles seen in the SEM images in Chapter 5. However, allowing too many degrees of freedom in the particles' geometry could quickly send us plummeting down a rabbit hole of computational complexity; concave particles, in particular, would be virtually impossible to model without considering the effects of self-shadowing by the particle and integrating some type of ray-tracing process into the simulation. For this reason, we impose:

Condition 6.1 ***Let the simulated particles be ellipsoids of uniform density.***

Modelling the simulated particles as uniform ellipsoids is a compromise between too much complexity and too little; each particle has three degrees of freedom, its axial lengths,

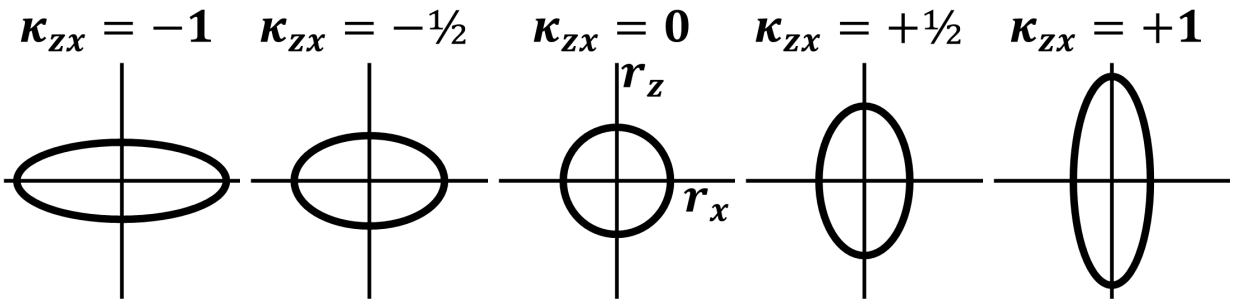

Figure 6.2: An example of how the appearance of ellipsoids can be connected to values in the κ-space. Here we can assume that the spheroids are symmetric about the r_z axis ($\kappa_{xy} = 0$). Negative values for κ_{zx} indicate squashing along the r_z axis (oblate spheroids), while positive values indicate stretching (prolate spheroids). The scale of r in these is taken to be arbitrary.

with the geometry of the particle ultimately being describable in terms of the amount of compression or elongation along these principal axes. We will, at this point, introduce a variable that we will describe as a 'shape parameter', κ_{ij}, which we will define as:

$$\kappa_{ij} = \ln\left(\frac{r_i}{r_j}\right) \tag{6.1}$$

Where r_i and r_j represent any pair of axial lengths of a particular ellipsoidal particle. This choice of coordinates comes with two distinct advantages: The first advantage is that we can now very easily interpret the shape of a particle based on these κ values: A point located at the origin of this 'κ-space' is a perfect sphere, any points located along any of the three κ axes is defined as a spheroid (an ellipsoid for which two of the three axial lengths are equal), with positive values of κ indicating stretched or prolate spheroids and negative values indicating squashed or oblate spheroids (as illustrated in Figure 6.2); and any off-axis points represent triaxial or scalene ellipsoids. The farther one moves on-axis in the positive or negative direction, the more rod-like or disk-like (respectively) the particles become; the farther away from the origin and the farther off-axis a particle lies, the more asymmetric its shape.

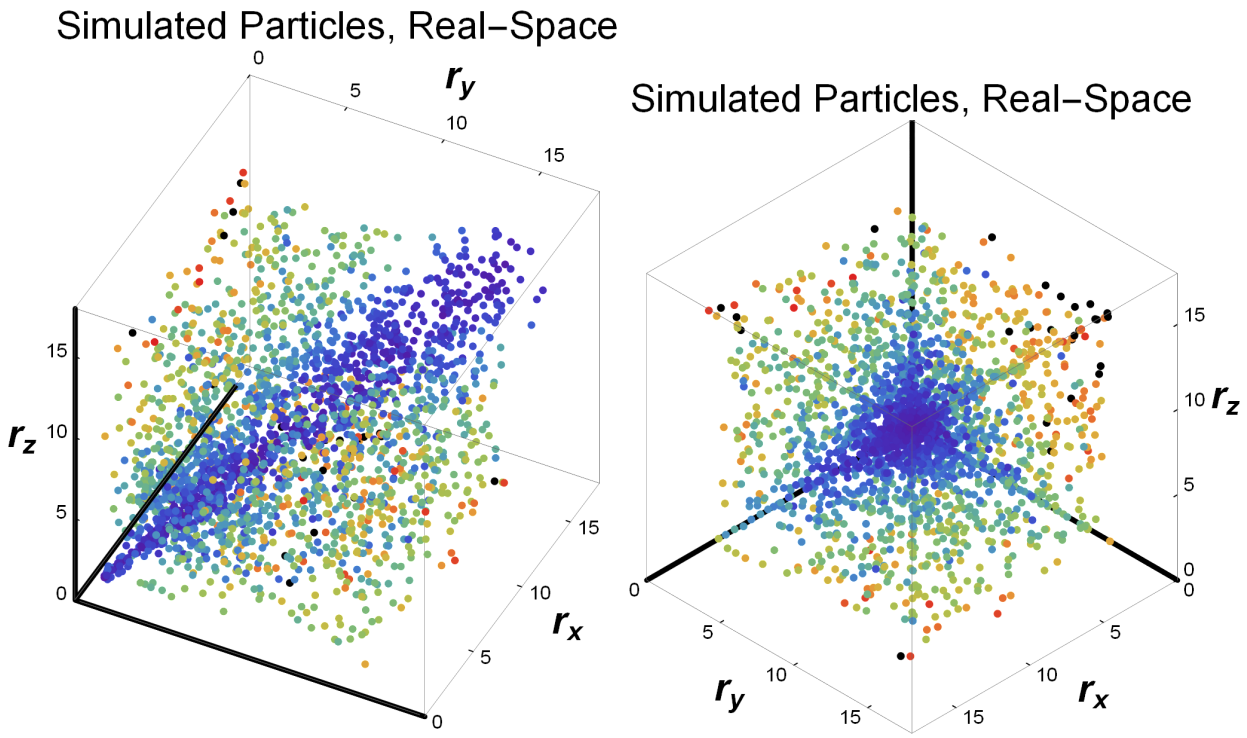

Figure 6.3: A visualization of where the simulated particles lie in real-space (with their axial lengths measured in microns). The color of the points is related to the periodicity of each particle's motion. This is elaborated on in Section 6.3, but in brief - bluer points correspond to more periodic particle motion, redder to more chaotic motion. Looking up along the $r_x = r_y = r_z$ line (*right*), we can already see indications that more symmetric particles yield more periodic motion.

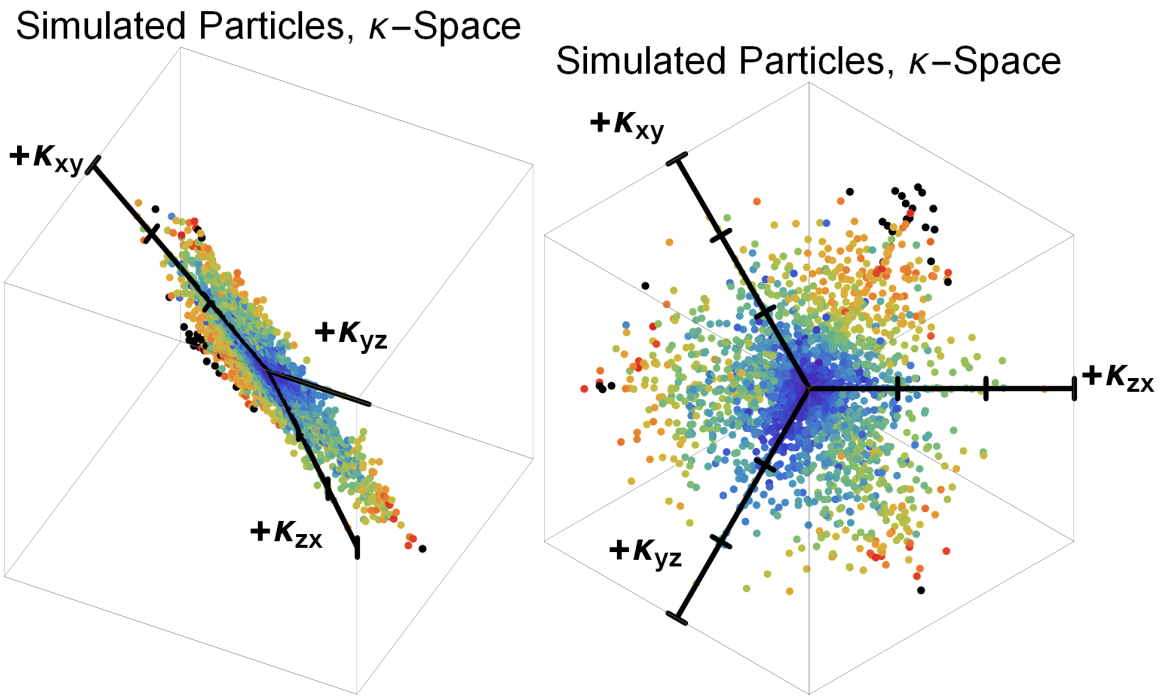

Figure 6.4: The same data from Figure 6.3 transformed into the κ-space. Information about the real-space dimensions of the particles are lost, but information about the shape is preserved and the data is condensed into a plane.

Second, as an additional feature of this coordinate system, one can take advantage of the inherent relationship between the different ratios of our three axial lengths:

$$\frac{r_x}{r_y}\frac{r_y}{r_z}\frac{r_z}{r_x} = 1 \tag{6.2}$$

As a consequence of this geometric condition, we see that the logarithmic shape parameters themselves must obey the relationship:

$$\kappa_{xy} + \kappa_{yz} + \kappa_{zx} = 0 \tag{6.3}$$

Which describes a plane in κ-space, centered at the origin (the difference between the real-space that the particles live in, and the κ-space we have created is shown in Figures 6.3 and 6.4). This implies that there is there is some principal axis we can rotate our κ-space to align with which will project all of our data into a symmetric, two-dimensional space.

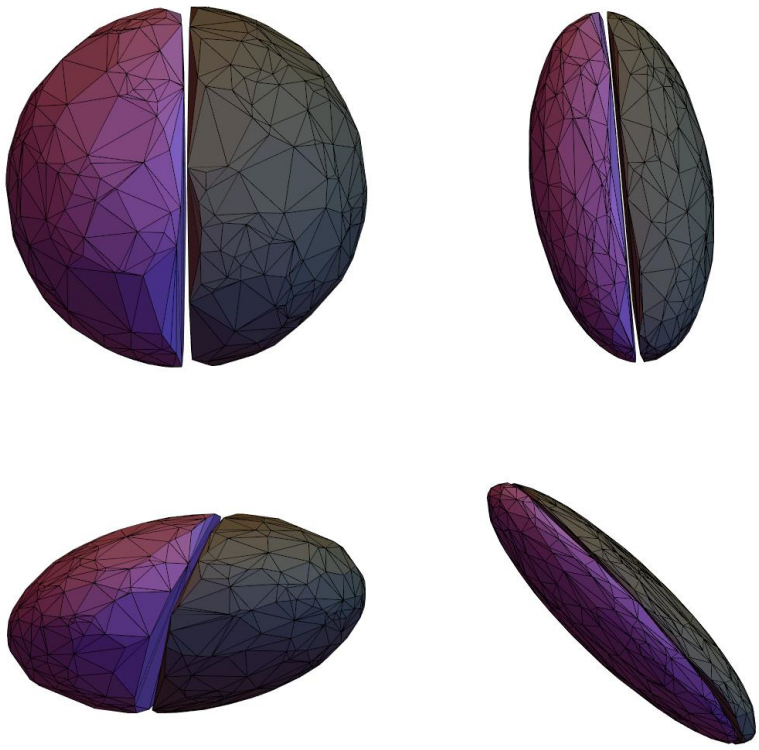

Figure 6.5: Visual depiction of the simulated examples of the spherical (*top-left*), prolate, (*top-right*), oblate (*bottom-left*), and scalene (*bottom-right*) ellipsoid dust particles described in Table 6.1, as "viewed" from the position of the camera in the experiments described in Chapters 4 and 5. In each image, the illumination of the UV source originates from the left. The purple and dark gray coloring indicate the surface of each particle which is illuminated and in shadow (respectively) at its pictured orientation.

This rotation will make the data discussed later in this chapter much simpler to display and interpret.

Table 6.1 shows how the results of several different ellipsoids - a simulated sphere, a prolate spheroid of aspect ratio 2, an oblate ellipsoid of aspect ratio 2, and a scalene ellipsoid are projected into this κ-space. Figure 6.5 shows a visual depiction of the four simulated dust particles generated using the r and κ values described in Table 6.1. This illustrates some of the different geometries that result from the different stretchings and flattenings along each principal axis, as well as showing how the UV source (the images can be thought

of as being 'viewed' from the same camera position as the experiment, therefore the light is coming from the left side of the image) illuminates the dust.

Description of Dust Shapes in κ-Space						
Description of Ellipsoid	r_x	r_y	r_z	κ_{xy}	κ_{yz}	κ_{zx}
Sphere	5.835	5.835	5.835	0	0	0
Prolate	4.764	2.382	2.382	$+\ln 2$	0	$-\ln 2$
Oblate	1.945	3.890	3.890	$-\ln 2$	0	$+\ln 2$
Scalene	1.273	2.547	5.093	$-\ln 2$	$-\ln 2$	$+2\ln 2$

Table 6.1: Examples of four simulated ellipsoids in physical space (axial lengths, r_x, r_y, and r_z, given in μm) and κ-space. In this formalism, we can consider 0 to indicate symmetry along an axis. Positive κ values indicate stretching along an axis while negative values imply squashing along that axis. Motion and phase space data for these four particular particles are examined in detail in later figures.

The behaviors we are attempting to simulate with this model are already nonlinear enough without taking fully three-dimensional dynamics into consideration. Therefore, for the purposes of this simulation we impose:

Condition 6.2 ***Let all translational motion and forces be confined to the vertical axis.***

The decision to model this system as quasi-1D is not completely without basis supported by experimental results: We know that the potential, density, and temperature profiles in the plasma, at least in the central region where the dust is located, are predominantly oriented along the vertical axis. In principle, if we had a truly isolated particle in a large enough chamber that the horizontal gradients in the plasma parameters could be minimized, it is not unreasonable to infer that we would be able to limit the particle dynamics largely to a single axis.

This choice in symmetry also affects our modelling of the simple and collisional forces. In order to keep all of our particles in the same simulated region, the range of initial positions for the dust is limited to a range comparable to where we find the dust in our experiments, and an equilibrium charge is selected such that the simple force balance model is satisfied at

the particle's initial position (the introduction of the drag forces will modify its equilibrium slightly, but the particle will at least start near equilibrium).

We will use a simplified variation of the Epstein neutral drag model:

$$\mathbf{F_{nd}} \sim -\rho_n A_z v_{tn,av} \mathbf{v} \tag{6.4}$$

And a simplified version of the Hutchinson-Khrapak model will be used for the ion drag:

$$\mathbf{F_{id}} \sim \rho_i A_z v_{ti,av} \mathbf{v_{di}} (H + G \ln \Lambda) \tag{6.5}$$

Here ρ_n and ρ_i are the local mass densities of neutrals and ions in the plasma, A_z represents the projected area of the particle along the z-axis, and $v_{ts,av}$ is the average thermal speed for a Maxwellian distribution of neutrals or ions, $v_{ts,av} = \sqrt{8/\pi}\ v_{ts} = \sqrt{8k_B T_s/\pi m_s}$. The functions G, H, and $\ln \Lambda$ are as defined in (2.27) and (2.28) and are calculated using the radius of the equivalent sphere. These models are not a perfect physical replication of the forces that will be imparted on the dust, particularly for the ion drag, but they should produce forces that are of the correct order-of-magnitude, which will suffice for the goals of this computational research.

As discussed in Section 2.1, the charging behavior of the dust is incredibly complicated. The purpose of this computational research is not to test the specifics of a charging model, only to investigate the role that geometric asymmetry could play in determining the dynamic behavior of the dust when photo-discharging is introduced. Therefore, we will impose:

Condition 6.3 ***Let the discharge on the illuminated side of the dust be uniform, and proportional to the projected area along the light axis.***

It is already understood and accepted that the magnitude of a photoelectric current is dependent on the area illuminated by a light source. Therefore, for this simulation, we will assume that the fractional discharge of the illuminated side of the dust can be described as

follows:

$$\delta_Q \;=\; I_{UV}(t)\;\left(1\;-\;2\,\frac{A_x}{S_{tot}}\right) \tag{6.6}$$

Where A_x is the projected area along the light axis, S_{tot} is the total surface area of the ellipsoid, and $I_{UV}(t)$ is some function that describes the instantaneous intensity of the UV. For the purposes of the simulation, I_{UV} simply ranges from 0 (off) to 1 (on) and obeys an RC-like transition as it turns on or off with a gradient of 0.1 seconds. This is to let the simulation ease into the discharge and prevent the computational overshooting that may result from a sudden, discontinuous change, as well as to try and replicate the kind of discharging behavior seen in the experiment (see Figure 5.12).

If we assume that the unperturbed charge density on the dust surface is uniform, and that the discharging is uniform across the illuminated surface, then we can model the charge on the illuminated side of the dust as:

$$Q_1 \;=\; \delta_Q\;\frac{Q_{d,0}}{2} \tag{6.7}$$

And the charge on the unilluminated side of the dust as:

$$Q_2 \;=\; \frac{Q_{d,0}}{2} \tag{6.8}$$

Thus, the instantaneous total charge of the dust, Q_d is:

$$Q_{d,tot} \;=\; Q_1 \;+\; Q_2 \tag{6.9}$$

Note that this discharge produces difference in charge between the illuminated and unilluminated sides, this discharging behavior produces an electric dipole moment in the dust:

$$\mathbf{p_d} \;=\; (Q_1 \;-\; Q_2)\,\mathbf{d} \tag{6.10}$$

Where d is the displacement vector between the modelled locations of Q_1 and Q_2. For the sake of computational simplicity, we will model the charge on each side of the particle as being located at the centroid of each surface (the average position of all of the points facing towards or away from the UV source).

The creation of this dipole moment by the discharging is of special significance, because a dipole in an electric field will experience a torque:

$$\tau_{\mathbf{E}} = \mathbf{p_d} \times \mathbf{E} \tag{6.11}$$

In our theoretical hypothesis, and in our computational model, it is the dipole moment produced by the asymmetric discharge of the dust particle, and the resulting torque applied by the electric field which alters the orientation of the dust during the pulses and produces the changing projected areas that lead to chaotic behavior. In order to simplify the description of the dust's rotation we, finally, impose:

Condition 6.4 ***Let the rotational motion of the dust generated by the dipole torque from the electric field be mobility-limited by interactions with neutrals.***

This condition is imposed to simplify calculation of the particle's rotation and to limit any numerical instabilities. Starting from the simplified form of the Epstein drag for a low-velocity particle in a dilute gas we invoked in (6.4), we can define the differential torque exerted by the neutrals over the surface as

$$d\tau_{nd} = (\mathbf{r_s} \times \mathbf{dF_{nd}}) = -\rho_n v_{tn,av} \, (\mathbf{r_s} \times \mathbf{v}) \, dS \tag{6.12}$$

Where dS implies an integration over the dust's surface. Furthermore we will impose a 'no-slip' condition to the particle's rotation:

$$\mathbf{v} = \mathbf{\Omega} \times \mathbf{r_s} \tag{6.13}$$

The imposition of this no-slip condition forces the flow of neutrals to be parallel to the dust surface and, therefore, normal to r_s. From this condition, we can show that:

$$\mathbf{r_s} \times \mathbf{v} = \mathbf{r_s} \times (\mathbf{\Omega} \times \mathbf{r_s}) = \mathbf{\Omega}\,(\mathbf{r_s} \cdot \mathbf{r_s}) + \mathbf{r_s}\,(\mathbf{\Omega} \cdot \mathbf{r_s}) = \mathbf{\Omega} {r_s}^2 \tag{6.14}$$

The torque exerted by the neutrals, then, can be expressed as a surface integral, which we can convert to a discrete sum for our simulation:

$$\tau_{\mathbf{nd}} \;=\; -\iint \rho_n \; v_{tn,av} \; \mathbf{\Omega} \; {r_s}^2 \; dS \;=\; -\sum_i \rho_n \; v_{tn,av} \mathbf{\Omega} {r_s}^2 \Delta S_i \tag{6.15}$$

If the points are randomly and evenly distributed then we can describe the torque in terms of local plasma parameters, the total surface area, S_{tot}, and some numerically integrated sum, $\Sigma {r_s}^2$, which can be calculated when the particle is generated by the simulation (note, that since r_s only describes points along the dust surface it is not represent the same kind of integration/sum that would describe the particle's moment of inertia).

$$\tau_{\mathbf{nd}} \;=\; -\rho_n \; S_{tot} \; v_{tn,av} \; \Sigma {r_s}^2 \; \mathbf{\Omega} \tag{6.16}$$

Now, assuming the torque applied on our dust dipole is mobility-limited by the torque exerted by the neutrals, our particle is in a state of dynamic rotational equilibrium:

$$\tau_{\mathbf{nd}} \;=\; -\tau_{\mathbf{E}} \tag{6.17}$$

$$-\rho_n \; S_{tot} \; v_{tn,av} \; \Sigma {r_s}^2 \; \mathbf{\Omega} \;=\; -\mathbf{p_d} \;\times\; \mathbf{E} \tag{6.18}$$

And we can derive an expression for the angular velocity of the dust due to the dipole effect:

$$\mathbf{\Omega_E} \;=\; \frac{\mathbf{p_d} \;\times\; \mathbf{E}}{\rho_n \; S_{tot} \; v_{tn,av} \; \Sigma {r_s}^2} \tag{6.19}$$

There should, in principle, be some other term corresponding to the balance between the neutral and ion drag, but in the interests of keeping our model focused on the larger goal, we will just assume there is some inherent background rotation that this dipole twisting is overlaid on. The background rotation will be randomly generated for each particle and should average to zero with sufficient simulation statistics.

6.2.2 Simulation Procedure

The functional code is written and processed using Wolfram Mathematica[15]). The simulation runs through the following procedure: First, on initialization, a series of initial values are selected. A list of several thousand randomized axial lengths and initial positions, orientations, velocities, and angular velocities was generated for these simulations to draw from, along with several dozen special cases such as perfect spheres or spheroids to ensure that these cases were included in the simulation. Relevant dust parameters are calculated from the parameter list; the surface area, moment of inertia tensor, $\sum {r_s}^2$, etc., and a uniform distribution of 500 points is generated to represent the surface of the dust particle for the purposes of determining the illuminated surfaces.

As the iterative phase of the simulation begins, the current real-space positions of each of the 500 points comprising the dust surface are used to calculate the surface normal vectors $\hat{\mathbf{n}}$ of each position on the dust surface. A simple inner product is taken with the $\hat{\mathbf{x}}$ vector (the direction of the light source) and each point is evaluated to determine if it is facing toward ($\hat{\mathbf{x}} \cdot \hat{\mathbf{n}} < 0$) or away ($\hat{\mathbf{x}} \cdot \hat{\mathbf{n}} \leq 0$) from the UV source. The centroid or average position of all of the points contained in each half of the dust surface are calculated at this stage, as is the projected area of the ellipsoid along the x and z axes. At this stage the new instantaneous charges of each half, the dipole moment, and the net charge are also calculated, based on the dust's orientation, projected areas, and the instantaneous intensity of the simulated source.

Next, the relevant secondary parameters - the local ion density, electric field strength, and other various plasma parameters relevant for the calculation of the forces on the dust -

are calculated. At this stage the forces and torques on the particle are calculated from the present dust and plasma parameters. The linear acceleration is used to calculate the dust's instantaneous displacement and velocity via the kinematic equations, and the instantaneous angular velocity and angular displacement are determined.

At the conclusion of each step of the iterative process, the properties of interest (the position, velocity, projected areas, charge, orientation, etc.) are added to arrays and fed back into the next stage of the iteration.

6.3 Analyzing Simulation Results

The simulation outputs a great deal of data, but for the purposes of our discussion here, the properties of interest are the particle's position and velocity over time. Looking at the position of the particle over the length of many overlapping pulses (as we did in Figures 5.9) as well as the paths that the particles take through the v_z vs z phase space over many pulses, we can qualitatively judge the behavior of different particles to be more periodic or more chaotic. Figure 6.6 shows the resulting position versus pulse time results for each of the four simulated particles, and Figure 6.7 shows their orbits through phase space.

Qualitatively, looking at these figures we can make a broad correlation between symmetry and and periodicity of a particle's motion over time. Extremely symmetric particles like the sphere, exhibit virtually no deviation in their position vs time or velocity vs position behavior, and travel through nearly identical paths on each pulse. Prolate spheroids appear to undergo relatively periodic motion, while oblate spheroids and scalene ellipsoids appear to undergo varying degrees of chaotic motion.

Quantitatively, we can describe the regularity of each particle's motion by looking at the area, A, that the particle sweeps out through phase space on each orbit (each UV pulse). Here we define δ_A as the standard deviation in the phase space area over the course of 19

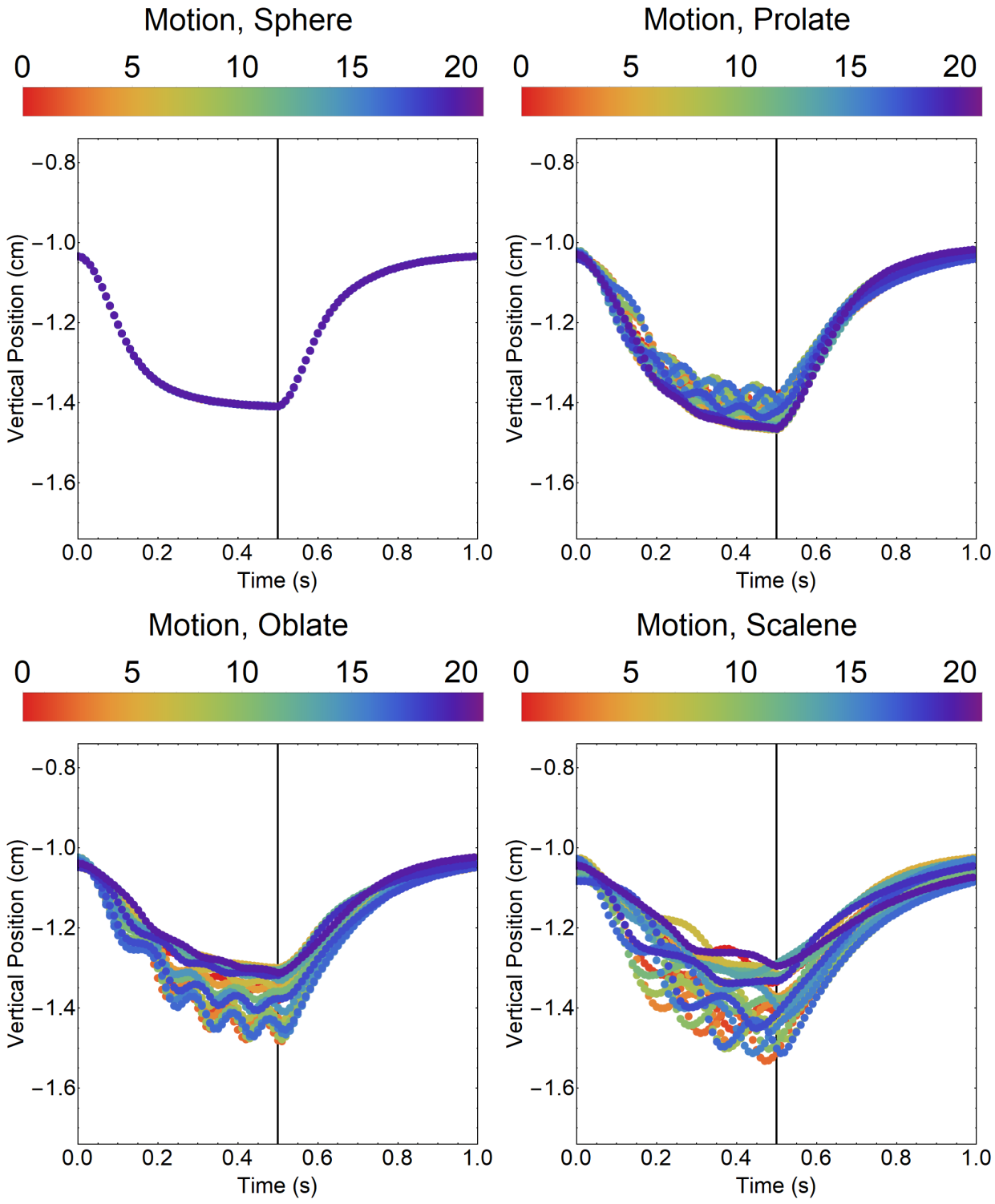

Figure 6.6: The position versus time data for the simulated particles shown in Figure 6.5, over the course of 19 simulated pulses.

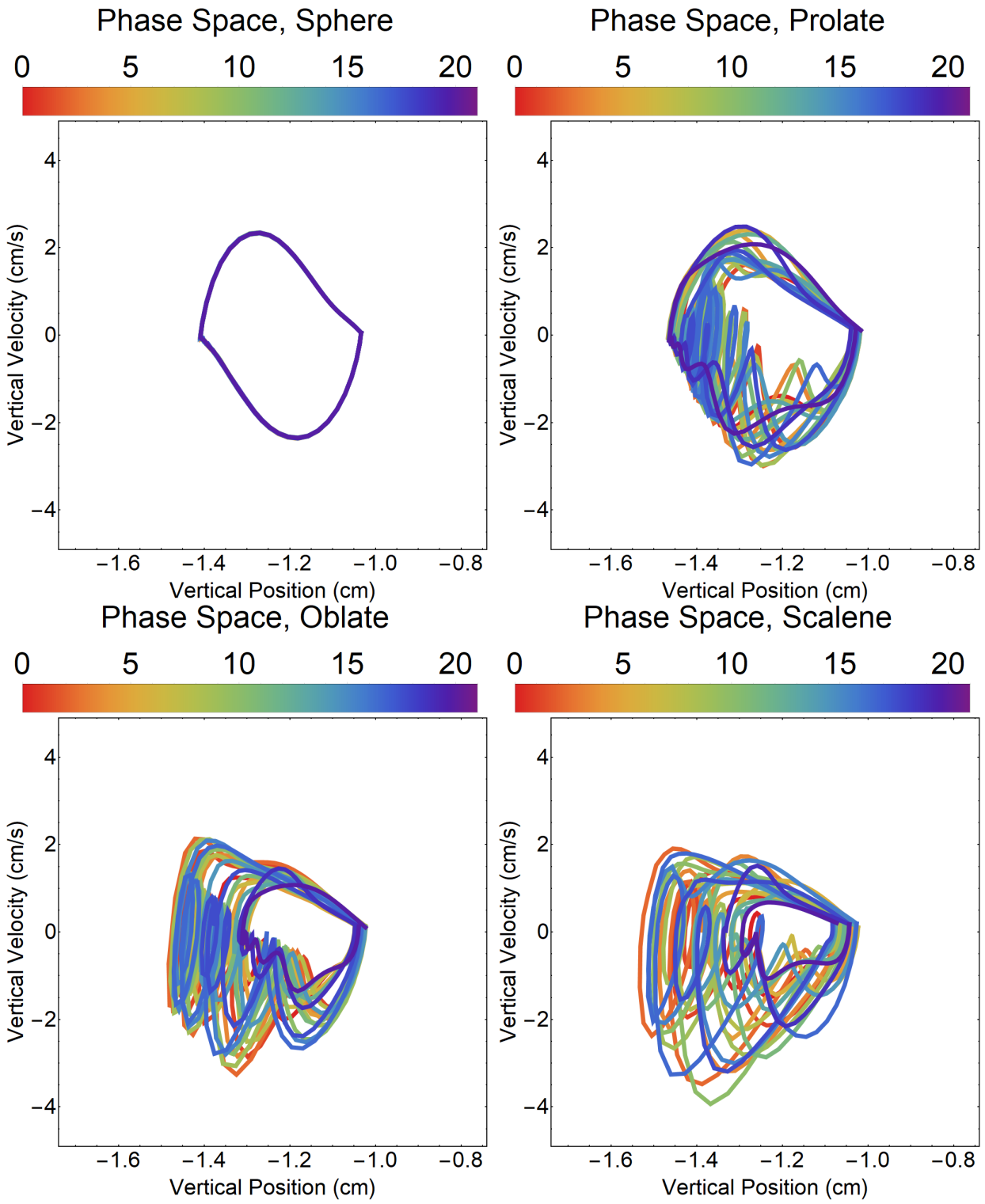

Figure 6.7: Phase space plots of the position and velocity data extracted from Figure 6.6, over the course of 19 simulated pulses. The color indicating the pulse number. The spherical particle undergoes super-periodic motion with almost no deviation, the prolate particle experiences periodic motion, while the oblate and scalene particles exhibit various degrees of chaotic motion

pulses worth of particle-data over the mean phase space area over the same dataset.

$$\delta_A = \frac{\sigma_A}{\mu_A} \tag{6.20}$$

Measuring the δ_A value of the four simulated examples yields the results shown in Table 6.2: Four particles, of course, is not a sufficiently large enough sample to draw any real conclusions

Deviation in Phase Space	
Case	δ_A
Sphere (sim.)	0.0013
Prolate (sim.)	0.0744
Oblate (sim.)	0.4550
Scalene (sim.)	0.5270

Table 6.2: The periodicity of the behavior of the simulated particles is quantified in terms of a deviation in phase space area, defined as $\delta_A = \sigma_A$ / μ_A, where μ_A is the average phase space area and σ_A is the standard deviation.

from. In order to fully understand the effects of the geometry on the dust dynamics, a total of 2500 particles were simulated and their results processed to produce the results seen in Figure 6.8. The figure shows the calculated δ_A, averaged over small interrogation regions, of all 2500 particles. As discussed in Section 6.1, the projection of the simulated data into the logarithmic κ-space collapses the data into a plane, which can be preferentially rotated into a 2D projection, which has been done for the figure. The positive κ_{xy}, κ_{yz}, and κ_{zx} axes in this space indicate the direction along which simulated prolate spheroids appear, with the particles becoming more and more elongated as one follows along any of these three axes. In the opposite direction, then, are the oblate spheroids, and in betwixt these intersecting lines fall the scalene ellipsoids. Taking the inverse of δ_A defines, effectively, a signal-to-noise ratio (SNR), essentially a description of how "noisy" the orbits of the dust in phase space are. Figure 6.9 shows this signal-to-noise ratio, plotting the results of $-\ln \delta_A$ instead of δ_A in the same projection of κ-space.

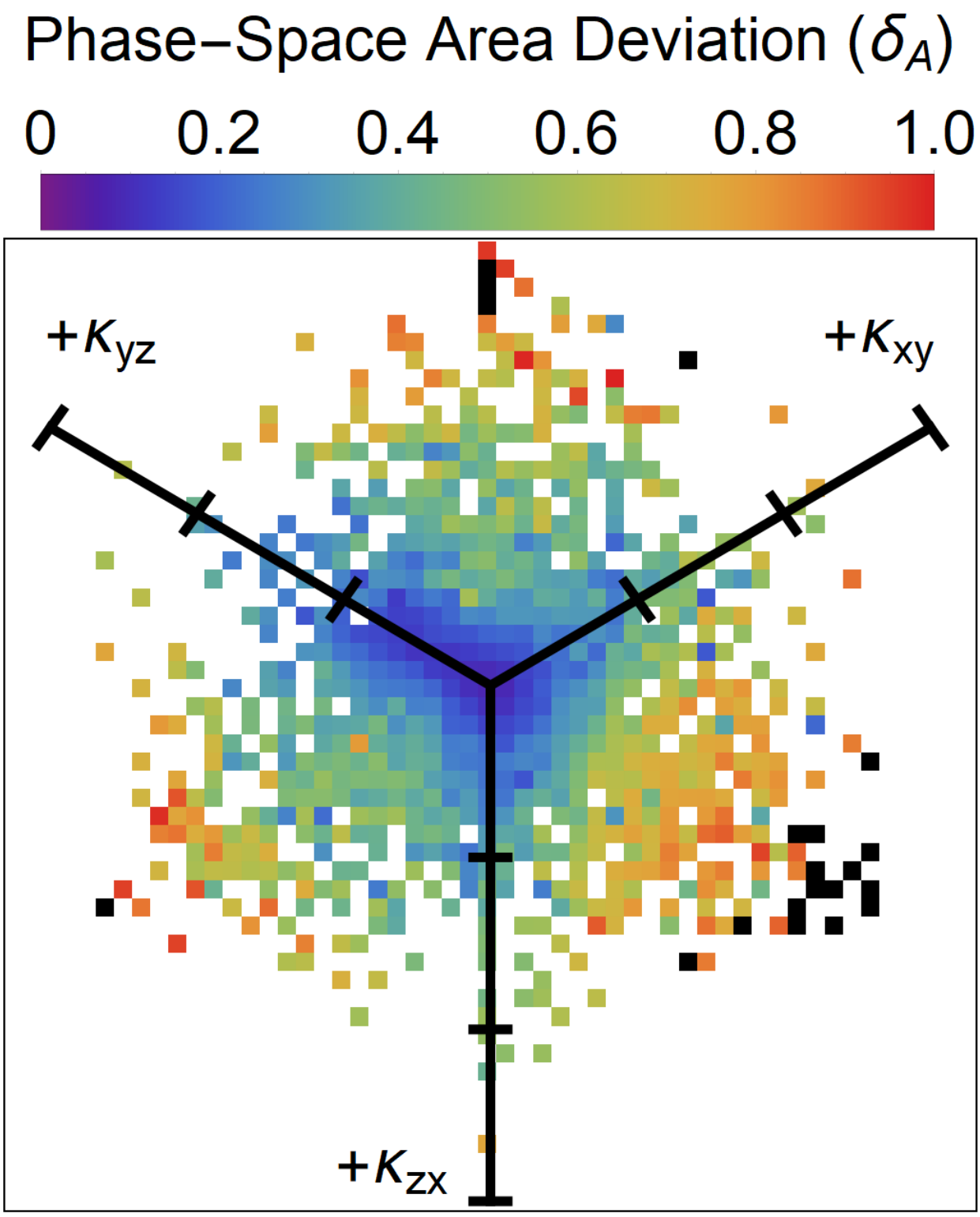

Figure 6.8: The κ-space projection of the deviation in the phase space areas of the simulated dust particles ($\delta_A = \sigma_A \ / \ \mu_A$). Each square indicates an average of δ_A values within some interrogation region. Bluer squares indicate periodic behavior, while redder squares indicate chaotic behavior. Black squares near the outskirts of data indicate 'super-chaotic' behavior.

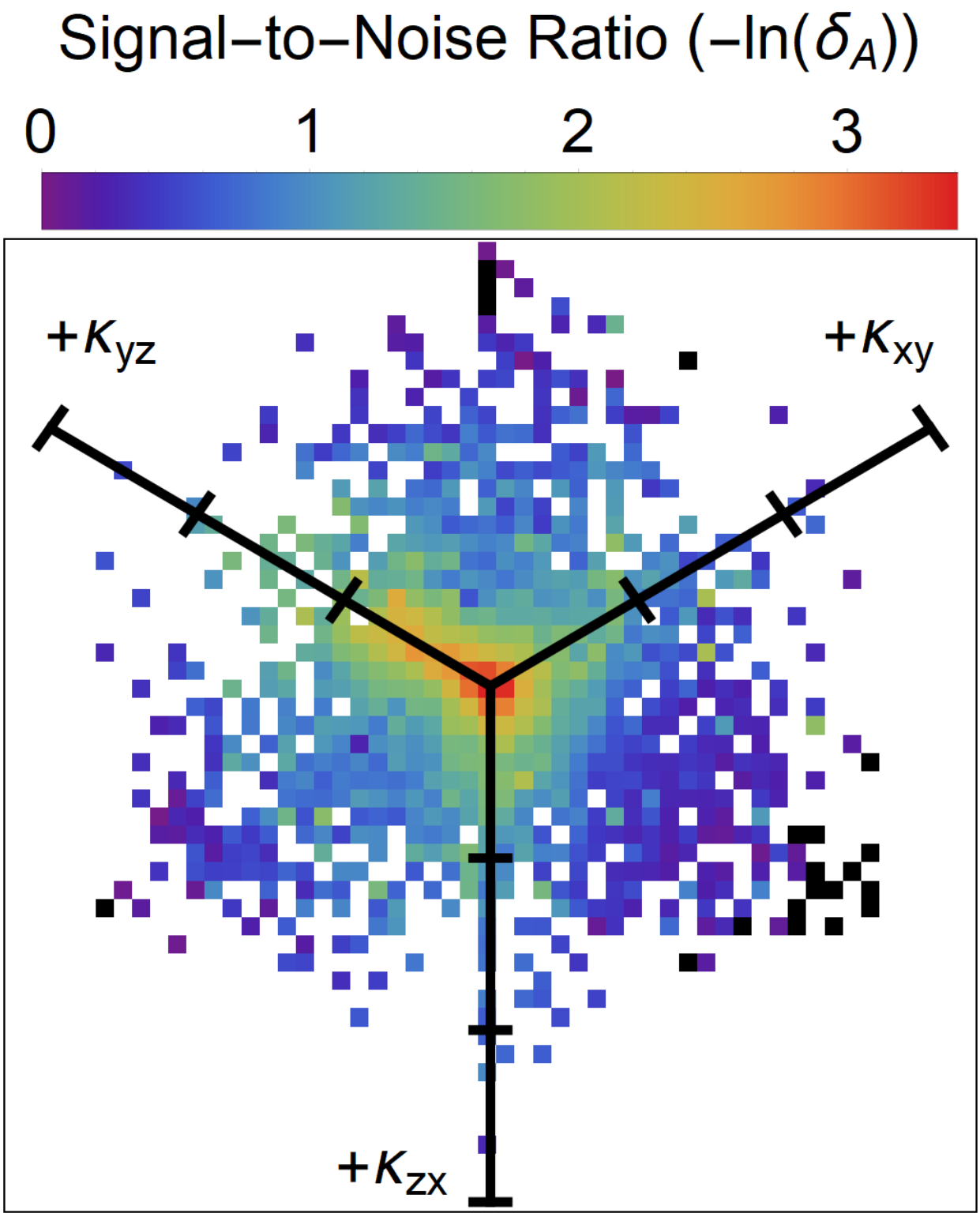

Figure 6.9: The κ-space projection of the deviation in the phase space areas of the dust particles ($SNR = -\ln \delta_A$). Each square indicates an average of δ_A values within some interrogation region. Bluer squares indicate periodic behavior, while redder squares indicate chaotic behavior. Black squares near the outskirts of data indicate 'super-chaotic' behavior.

Between the results of Figures 6.8 and 6.9, we can identify four qualitatively distinct behavioral regions within the data which can be roughly differentiated in terms of their respective deviations in phase space area. Here, we describe these dynamic regions as: Super-periodic, Quasi-periodic, Quasi-chaotic, and Super-chaotic. Super-periodic behavior describes orbits in phase space with almost no deviation from the average, each orbit sweeps out a nearly identical path through phase space (values of δ_A approaching 0, and typically less than $e^{-2.5} \sim 0.08$). Quasi-periodic behavior describes dust motion that is predominantly periodic, but has some noticeable deviation (values of δ_A which are much less than 1, typically less than $e^{-1.5} \sim 0.22$). Chaotic behavior describes dust motion that has transitioned into more random displacements and whose paths through phase space will become closed (values of δ_A approaching, but still less than ~ 1). Super-chaotic behavior describes those particles whose dynamics have transitioned into a regime that is essentially more 'noise' than 'signal', their orbits through phase space frequently loop back in on themselves, often many times in a single orbit, and they rarely return to the same equilibrium position between pulses (values of δ_A exceeding ~ 1). These approximate regions are listed in Table 6.3.

Description of Dust Behavior	
Super-periodic	$\ln \delta_A < -2.5$
Quasi-Periodic	$-2.5 < \ln \delta_A < -1.5$
Quasi-Chaotic	$-1.5 < \ln \delta_A < 0$
Super-chaotic	$\ln \delta_A > 0$

Table 6.3: Broad description of the periodicity of different dust behaviors in terms of $\ln \delta_A$. These ranges should be taken to be very approximate.

6.4 Discussion

If we examine where these regions actually fall on our map of κ-space, we see an interesting correlation: The super-periodic region is concentrated exclusively in the center of our κ-space, where the spherical or near-spherical particles reside. Quasi-periodic behavior is predominantly limited to cases very close to the principal axes where the prolate and

oblate spheroids reside, with more more periodic behavior appearing to favor prolates over oblates. The quasi-chaotic region is occupied by flatter oblates, longer prolates, and noticeably scalene ellipsoids (again, periodicity seems to favor prolates). The super-chaotic region appears to exist far from the center, typically with magnitudes of κ of 2-3 or greater. These computational results would appear to imply a strong correlation between particle geometry and periodic versus chaotic behavior.

These results can also be contrasted with experimental data from the photo-discharging experiment in Chapter 5. Figure 6.10 shows the position versus time and phase space data for two experimental particles, one exhibiting periodic-like behavior and one exhibiting chaotic-like behavior. A calculation of δ_A (Table 6.4) places the qualitatively periodic particle into what we have quantitatively defined as the super-periodic region, and the chaotic particle into the quasi-chaotic region.

Deviation in Phase Space	
Case	δ_A
Periodic (exp.)	0.0299
Chaotic (exp.)	0.3220

Table 6.4: The periodicity of the behavior of the experimental dust particles.

A certain level of caution should be taken when comparing the results of these simulations to our experimental data. As the SEM data in Figure 5.2 shows, few (if any), of these particles are what could be considered ellipsoidal. Many have sharp edges and concavities that would require a considerably more complex simulation in order to model. However we can, at least, draw a qualitative result from these simulations that supports our initial hypothesis: If the amount of surface charge removed from the illuminated side of the dust is proportional to the projected area, then a consequence of that assumption is that more symmetric particles will undergo more symmetric 'orbits' and more asymmetric particles will undergo more chaotic orbits.

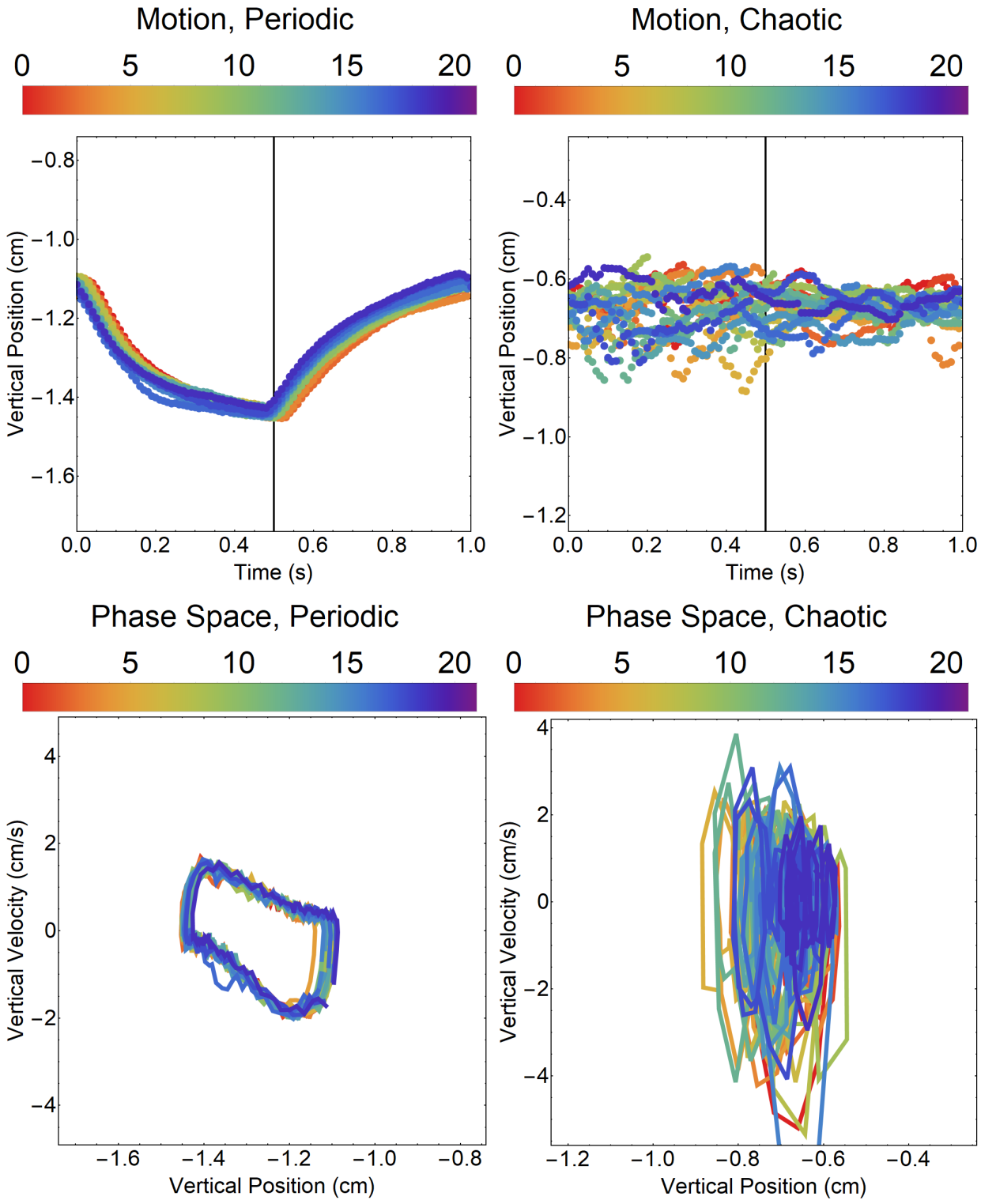

Figure 6.10: Position (*top*) and phase space plots (*bottom*) for real experimental examples from the photo-discharging experiment in Chapter 5.

Having only been experimentally validated within the last 18 months, there is still a great deal which is not understood about the dust dynamics observed under the effect of photo-discharging. However, this computational work offers some valuable insight to the role that the shape and monodispersivity of dust particles may play in determining these dynamics. These results may also help to inform future experimental results as well as theoretical and computational followups.

Chapter 7

Summary and Future Work

In the beginning of this work, the concept of a dusty plasma was introduced and their growing presence and influence in plasma physics and the applications of plasma technology was examined. We discussed the practical challenges posed by the inability to actively influence this most fundamental property of dusty plasma systems, and posited on what it would and could mean if we could start to exert some directed control over the charging behavior of the dust. We set for ourselves the ambitious goal of developing methods to control the charging behavior of the dust, and also insisted that these methods must minimize any impact on the background plasma. Two methods were investigated through experimental research - an attempt to alter the inherent charging currents through controlled fluctuations and the introduction of new charging currents using the photoelectric effect.

7.1 Controlling Dust Charge

While the attempts to use fluctuations in the ion current to control the dust charge was able to produce some interesting results, and while there was indeed strong evidence that the method succeeded in reducing the dust charge, the analysis of the effects on the plasma were ultimately inconclusive. The implications of the changes in the space potential are still unclear - is it merely an artifact picked up by the uncompensated Langmuir probe, or is there a change in the background conditions? While we believe that this method still has great potential as a mechanism for controlling dust behavior, it still has a great deal of investigation and refinement that must be pursued first.

The results and implications of the photo-discharging experiment are extremely promising; the attempt to use of photocurrents to generate measurable and significant discharge

in the dust was an irrefutable success. Not only did the experiment demonstrate a massive and easily reproducible discharge of the dust particles in the plasma, but it was able to demonstrate that careful tuning of the experimental parameters could allow the discharge to be accomplished with little to no effect on the background plasma.

The significant discharge, the clear lack of effect on the plasma, and the relative ease with which the apparatus can be modified to accommodate other experiments and apparatuses makes photo-discharging the clear favorite for future research pursuits into controlling dust charge and has already lead to the intriguing computational work discussed in Chapter 6. Photo-discharging not only offers the practical opportunity to control dust charge, but a wealth of new curiosities and physical effects to study.

7.2 Next Steps

Future continuations of this computational research might explore more complex models and geometry. The dipole model used in the simulation may be too much of an oversimplification, and more rigorous charge distribution models could be developed and included. The behavior of irregular geometries with more sharply defined faces and edges or concave shapes that can produce shadowing effects would require significantly more complicated modelling, but would be of interest in understanding the response of the dust to photo-discharging.

On the experimental front, photo-discharging clearly holds the most promise for future developments in manipulating dust charge; both because of the very clear discharge and because of the minimal effects on the background plasma. One can easily picture a multitude of interesting and exciting follow-up experiments: The intensity of the UV could be modulated to 'tune' the frequency of dust waves; the discharging could be applied to a dust crystal to induce an instantaneous change in phase by reducing the dust coupling parameter (a dusty plasma 'death-ray'); it could be applied to a dust void to examine the changes in void size and shape; or introduced into a magnetized plasma experiment to look at the effects on induced dust structures or the combination of directional plasma currents and discharging.

The first and most pressing follow-up proposed here is a broader study of the effects of the UV on conventional dust materials: Preliminary tests conducted at the time of this dissertation's publication indicate that silica dust particles also exhibit a response to the high intensity UV light. This suggests that the photon energy required for particle discharge may be well below the conventional work function of the dust material, and instead closer to the dust's equilibrium surface potential, the electron temperature, or some other energy or aggregate term. This may open up the possibility of applying photo-discharging to a wide range of common dust materials instead of being restricted to specialized materials like LaB_6. As discussed, other dust materials like silica are significantly easier to find in monodisperse, geometrically uniform samples, which would help to enable some of the more interesting experimental follow-up ideas listed above. The use of monodisperse microsphere samples also offers the possibility of experimentally validating the computational work outlined in Chapter 6.

Practical applications of this photo-discharging technique are also of significant interest; with high-intensity UV LEDs becoming more affordable, the concept of deploying an entire array of photo-discharging light sources inside something like a processing plasma apparatus is entirely feasible. One could quite easily test the efficacy of such an array at removing dust from the plasma environment and improving fabricated device yields.

External, independent control over the dust charging processes is a concept that has long been discussed and debated, and has now, finally, been demonstrated under practical experimental conditions. The realization of this technique, and other techniques for controlling dust behavior that it may inspire, opens up a tantalizing treasure trove of practical applications, novel experiments, new puzzles to solve, and new questions to ask.

Let's get started.

Bibliography

[1] Michael S. Barnes, John H. Keller, John C. Forster, James A. O'Neill, and D. Keith Coultas. Transport of dust particles in glow-discharge plasmas. *Physical Review Letters*, 68(3):313–316, 1992.

[2] F. Brochard, A. Shalpegin, S. Bardin, T. Lunt, V. Rohde, J.l. Briançon, G. Pautasso, C. Vorpahl, and R. Neu. Video analysis of dust events in full-tungsten ASDEX upgrade. *Nuclear Fusion*, 57(3):036002, 2016.

[3] Chunshi Cui and J. Goree. Fluctuations of the charge on a dust grain in a plasma. *IEEE Transactions on Plasma Science*, 22(2):151–158, 1994.

[4] P. S. Epstein. On the resistance experienced by spheres in their motion through gases. *Physical Review*, 23(6):710–733, 1924.

[5] Ross Fisher and Edward Thomas. Thermal properties of a dusty plasma in the presence of driven dust acoustic waves. *IEEE Transactions on Plasma Science*, 38(4):833–837, 2010.

[6] Institute for Plasma Physics. The COMPASS tokamak - pellet explosion. `https://www.youtube.com/watch?v=wDfJhaQ7JIc`, 2020.

[7] C. K. Goertz. Dusty plasmas in the solar system. *Reviews of Geophysics*, 27(2):271, 1989.

[8] J. Goree, G. E. Morfill, V. N. Tsytovich, and S. V. Vladimirov. Theory of dust voids in plasmas. *Physical Review E*, 59(6):7055–7067, 1999.

[9] Taylor Hall, Edward Thomas, Khare Avinash, Robert Merlino, and Marlene Rosenberg. Methods for the characterization of imposed, ordered structures in MDPX. *Physics of Plasmas*, 25(10):103702, 2018.

[10] Taylor H. Hall and Edward Thomas. A study of ion drag for ground and microgravity dusty plasma experiments. *IEEE Transactions on Plasma Science*, 44(4):463–468, 2016.

[11] M. Horányi. Dusty plasma effects in Saturn's magnetosphere. *Reviews of Geophysics*, 42(4), 2004.

[12] I H Hutchinson. Ion collection by a sphere in a flowing plasma: 2. non-zero debye length. *Plasma Physics and Controlled Fusion*, 45(8):1477–1500, 2003.

[13] I H Hutchinson. Ion collection by a sphere in a flowing plasma: 3. floating potential and drag force. *Plasma Physics and Controlled Fusion*, 47(1):71–87, 2004.

[14] I H Hutchinson. Collisionless ion drag force on a spherical grain. *Plasma Physics and Controlled Fusion*, 48(2):185–202, 2006.

[15] Wolfram Research, Inc. Mathematica, Version 13.0.0. Champaign, IL, 2021.

[16] Surabhi Jaiswal, P. Bandyopadhyay, and Abhijit Sen. Dusty plasma experimental (DPEx) device for complex plasma experiments with flow. *Review of Scientific Instruments*, 86, 07 2015.

[17] M. R. Jana, A. Sen, and P. K. Kaw. Collective effects due to charge-fluctuation dynamics in a dusty plasma. *Physical Review E*, 48(5):3930–3933, 1993.

[18] H Kersten, R Wiese, G Thieme, M Fr Hlich, A Kopitov, D Bojic, F Scholze, H Neumann, M Quaas, H Wulff, and et al. Examples for application and diagnostics in plasma–powder interaction. *New Journal of Physics*, 5:93–93, 2003.

[19] S. A. Khrapak, A. V. Ivlev, G. E. Morfill, and H. M. Thomas. Ion drag force in complex plasmas. *Physical Review E*, 66(4), 2002.

[20] Hiroshi Kimura. On the photoelectric quantum yield of small dust particles. *Monthly Notices of the Royal Astronomical Society*, 459(3):2751–2761, 2016.

[21] Michael A. Lieberman and Allan J. Lichtenberg. *Principles of plasma discharges and materials processing*. Wiley-Interscience, 2005.

[22] Brian Lynch, Uwe Konopka, and Edward Thomas. Real-time particle tracking in complex plasmas. *IEEE Transactions on Plasma Science*, 44(4):553–557, 2016.

[23] Michael McKinlay and Edward Thomas. Controlled photo-discharge of dust in a complex plasma. *Journal of Plasma Physics*, 87(2):905870223, 2021.

[24] Robert L. Merlino. Understanding langmuir probe current-voltage characteristics. *American Journal of Physics*, 75(12):1078–1085, 2007.

[25] M. W. Morooka, J.-E. Wahlund, A. I. Eriksson, W. M. Farrell, D. A. Gurnett, W. S. Kurth, A. M. Persoon, M. Shafiq, M. André, M. K. G. Holmberg, and et al. Dusty plasma in the vicinity of Enceladus. *Journal of Geophysical Research: Space Physics*, 116(A12), 2011.

[26] Los Alamos National Laboratory, n.d. The Periodic Table of Elements: LANL. `https://periodic.lanl.gov/18.shtml`.

[27] M. Rosenberg, D.A. Mendis, and D.P. Sheehan. UV-induced Coulomb crystallization of dust grains in high-pressure gas. *IEEE Transactions on Plasma Science*, 24(6):1422–1430, 1996.

[28] M. Rubel, A. Widdowson, J. Grzonka, E. Fortuna-Zalesna, Sunwoo Moon, P. Petersson, N. Ashikawa, N. Asakura, D. Hamaguchi, Y. Hatano, and et al. Dust generation in tokamaks: Overview of beryllium and tungsten dust characterisation in JET with the ITER-like wall. *Fusion Engineering and Design*, 136:579–586, 2018.

[29] Johannes Schindelin, Ignacio Arganda-Carreras, Erwin Frise, Verena Kaynig, Mark Longair, Tobias Pietzsch, Stephan Preibisch, Curtis Rueden, Stephan Saalfeld, Benjamin Schmid, and et al. Fiji: An open-source platform for biological-image analysis. *Nature Methods*, 9(7):676–682, 2012.

[30] G S Selwyn. Optical characterization of particle traps. *Plasma Sources Science and Technology*, 3(3):340–347, aug 1994.

[31] Muhammad Shafiq, J.-E. Wahlund, M.w. Morooka, W.s. Kurth, and W.m. Farrell. Characteristics of the dust–plasma interaction near Enceladus' south pole. *Planetary and Space Science*, 59(1):17–25, 2011.

[32] J P Sheehan and N Hershkowitz. Emissive probes. *Plasma Sources Science and Technology*, 20(6):063001, nov 2011.

[33] P. K. Shukla and A. A. Mamun. *Introduction to dusty plasma physics*. Institute of Physics Pub., 2002.

[34] V.v. Shumova, D.n. Polyakov, E.k. Mataybaeva, and L.m. Vasilyak. On the thermophoresis in dense dust structures in neon plasma. *Physics Letters A*, 383(27):125853, 2019.

[35] A. A. Sickafoose, J. E. Colwell, M. Horányi, and S. Robertson. Photoelectric charging of dust particles in vacuum. *Physical Review Letters*, 84(26):6034–6037, 2000.

[36] Lyman Spitzer. The Dynamics of the Interstellar Medium. I. Local Equilibrium. *The Astrophysical Journal*, 93:369, 1941.

[37] E. Thomas, K. Avinash, and R. L. Merlino. Probe induced voids in a dusty plasma. *Physics of Plasmas*, 11(5):1770–1774, 2004.

[38] Edward Thomas. Direct measurements of two-dimensional velocity profiles in direct current glow discharge dusty plasmas. *Physics of Plasmas*, 6(7):2672–2675, 1999.

[39] H M Thomas, M Schwabe, M Y Pustylnik, C A Knapek, V I Molotkov, A M Lipaev, O F Petrov, V E Fortov, and S A Khrapak. Complex plasma research on the International Space Station. *Plasma Physics and Controlled Fusion*, 61(1):014004, 2018.

[40] Hubertus M. Thomas and Gregor E. Morfill. Melting dynamics of a plasma crystal. *Nature*, 379(6568):806–809, 1996.

[41] K. Torgasin, K. Morita, H. Zen, K. Masuda, T. Katsurayama, T. Murata, S. Suphakul, H. Yamashita, T. Nogi, T. Kii, and et al. Thermally assisted photoemission effect on CeB6 and LaB6 for application as photocathodes. *Physical Review Accelerators and Beams*, 20(7), 2017.

[42] A. A. Uglov and A. G. Gnedovets. Effect of particle charging on momentum and heat transfer from rarefied plasma flow. *Plasma Chemistry and Plasma Processing*, 11(2):251–267, 1991.

[43] O. S. Vaulina, S. A. Khrapak, A. P. Nefedov, and O. F. Petrov. Charge-fluctuation-induced heating of dust particles in a plasma. *Physical Review E*, 60(5):5959–5964, 1999.

[44] Yukio Watanabe. Dust phenomena in processing plasmas. *Plasma Physics and Controlled Fusion*, 39(5A), 1997.

[45] J. Winter. Dust: A new challenge in nuclear fusion research? *Physics of Plasmas*, 7(10):3862, 2000.

[46] Chun-Shang Wong, J. Goree, Zach Haralson, and Bin Liu. Strongly coupled plasmas obey the fluctuation theorem for entropy production. *Nature Physics*, 14(1):21–24, 2017.

Appendices

Appendix A

Supplementary Theoretical Materials

This appendix discusses the derivation of the shifted-Maxwellian distribution shown in (2.24) and (4.5) and the derivation of the modified currents in (4.12) and (4.13).

A.1 Distribution Function

Let there be some plasma species, s, which is Maxwellian in its co-moving frame with a thermal velocity, ${v_{ts}}^2 = k_B\, T_s/m_s$. In the lab frame, assume that there is some drift velocity, v_{Ds}, oriented along the z-axis of the system. Take the non-normalized velocity distribution function of this species to have the form:

$$f(v_{s,x}, v_{s,x}, v_{s,x}) d^3 v_s = A \exp\left(- \frac{\left({v_{s,x}}^2 + {v_{s,y}}^2 + (v_{s,z} - v_{Ds})^2 \right)}{2\ {v_{ts}}^2} \right) dv_{s,x}\ dv_{s,y}\ dv_{s,z} \tag{A.1}$$

Define the velocities in spherical coordinates as usual:

$$v_{s,x} = v_s\ \sin\theta\ \cos\phi \tag{A.2}$$

$$v_{s,y} = v_s\ \sin\theta\ \sin\phi \tag{A.3}$$

$$v_{s,z} = v_s\ \cos\theta \tag{A.4}$$

The distribution function can then be written in spherical coordinates as:

$$f(v_s, \theta, \phi) d^3 v_s = A \exp\left(- \frac{\left({v_s}^2 \sin^2\theta + (v_s\ \cos\theta - v_{Ds})^2 \right)}{2\ {v_{ts}}^2} \right) {v_s}^2 \sin\theta\ dv_s\ d\theta\ d\phi \tag{A.5}$$

Make the substitution $\cos\theta = w$, $\sin\theta\, d\theta = -dw$, $\sin^2\theta = (1-w^2)$:

$$v_s{}^2 \sin^2\theta + (v_s\ \cos\theta - v_{Ds})^2 = v_s{}^2(1-w^2) + (wv_s - v_{Ds})^2 = v_s{}^2 - 2\ w\ v_s\ v_{Ds} + v_{Ds}{}^2 \quad \text{(A.6)}$$

Make the substitution $v_s/v_{ts} = M_s$ and $v_{Ds}/v_{ts} = M_{Ds}$. The expression reduces to:

$$f(M_s, w, \phi) d^3M_s = -A\ \exp\left(-\frac{1}{2}\left(M_s{}^2 - 2\ w\ M_s\ M_{Ds} + M_{Ds}{}^2\right)\right) M_s{}^2\ dM_s\ dw\ d\phi \quad \text{(A.7)}$$

Integrate over all angular values, ϕ from 0 to 2π, and w from 1 to -1:

$$f(M_s) dM_s = \frac{2\pi A}{M_{Ds}}\left[\exp\left(-\frac{(M_s + M_{Ds})^2}{2}\right) - \exp\left(-\frac{(M_s - M_{Ds})^2}{2}\right)\right] M_s\ dM_s \quad \text{(A.8)}$$

Integrating M_s from 0 to ∞ yields:

$$(2\pi)^{3/2} A = 1 \quad \text{(A.9)}$$

$$A = (2\pi)^{-3/2} \quad \text{(A.10)}$$

Substituting the normalization constant back into (A.8) gives a final form for the shifted Maxwellian distribution:

$$f_s{}'(v_s) d^3v_s = \frac{1}{\sqrt{2\pi}} \frac{M_s}{M_{Ds}}\left[e^{-\frac{(M_s - M_{Ds})^2}{2}} - e^{-\frac{(M_s + M_{Ds})^2}{2}}\right] dM_s \quad \text{(A.11)}$$

In contrast to the unshifted Maxwellian distribution function:

$$f_s(v_s)\ d^3v_s = \sqrt{\frac{2}{\pi}} M_s{}^2\ e^{-\frac{M_s{}^2}{2}}\ dM_s \quad \text{(A.12)}$$

A.2 Currents

As defined in (2.7), let the current collect by the dust for a given plasma species be:

$$I_{sd} = \langle q_s \; n_s \; v_s \; \sigma_{sd} \rangle = \int q_s \; n_s \; v_s \; \sigma_{sd} \; f_s(v_s) \; d^3 v_s \tag{A.13}$$

To simplify the integration and the series expansion that follows in this section, let us make the following substitutions: ${X_s}^2 = {M_s}^2/2 \; z_s$ and ${X_{Ds}}^2 = {M_{Ds}}^2/2 \; z_s$. This changes the expressions for the collisional cross sections, (2.5) and (2.6):

$$\sigma_{ed} = \pi {r_d}^2 \left(1 - 2 \frac{z_e}{{M_e}^2} \right) = \pi {r_d}^2 \left(1 - {X_e}^{-2} \right) \tag{A.14}$$

$$\sigma_{id} = \pi {r_d}^2 \left(1 + 2 \frac{z_i}{{M_i}^2} \right) = \pi {r_d}^2 \left(1 + {X_i}^{-2} \right) \tag{A.15}$$

The distribution function for the unshifted Maxwellian becomes:

$$f_s(v_s) \; d^3 v_s = \frac{4 \; {z_s}^{3/2}}{\sqrt{\pi}} {X_s}^2 \; e^{-z_s {X_s}^2} \; dX_s \tag{A.16}$$

The expression for the collected currents becomes:

$$I_{sd} = \int q_s \; n_s \; v_{ts} \sqrt{2 z_s} \; X_s \; \sigma_{sd} \; f_s(X_s) \; dX_s \tag{A.17}$$

This expression for the electrons is integrated over the bounds $X_e = 1$ to $X_e = \infty$, and the expression for the ions is integrated over the bounds $X_i = 0$ to $X_i = \infty$. This yields expressions from (2.9) and (2.10):

$$I_{ed} = -\sqrt{8\pi} \; e \; n_e \; v_{te} \; {r_d}^2 \; e^{-z_e} \tag{A.18}$$

$$I_{id} = +\sqrt{8\pi} \; e \; n_i \; v_{ti} \; {r_d}^2 \; (1 + z_i) \tag{A.19}$$

Meanwhile, the distribution function for the shifted Maxwellian becomes:

$$f_s{}'(v_s)\, d^3v_s = \sqrt{\frac{z_s}{\pi}} \frac{X_s}{X_{Ds}} \left(e^{-z_s(X_s - X_{Ds})^2} - e^{-z_s(X_s + X_{Ds})^2} \right)\, dX_s \tag{A.20}$$

This shifted Maxwellian can be expanded about X_{Ds} under the weak-field limit discussed in Section 4.1.2. Expanding to second-order yields the expression:

$$f_s{}'(v_s)\, d^3v_s \approx \frac{4\, {z_s}^{3/2}}{\sqrt{\pi}} {X_s}^2\, e^{-z_s {X_s}^2} \left(1 + z_s\, {X_s}^2 \left(2\, z_s\, {X_s}^2 - 1\right)\right)\, dX_s \tag{A.21}$$

Integrating with the same bounds and cross-sections yields the perturbed currents:

$$I'_{ed} = -\sqrt{8\pi}\, e\, n_e\, v_{te}\, {r_d}^2\, e^{-z_e} \left(1 + \frac{1}{3}\, z\, {X_{De}}^2\right) \tag{A.22}$$

$$I'_{id} = +\sqrt{8\pi}\, e\, n_i\, v_{ti}\, {r_d}^2\, (1 + z_i) \left(1 + \frac{1}{3}\, z\, {X_{Di}}^2 \left(\frac{z_i - 1}{z_i + 1}\right)\right) \tag{A.23}$$

Substituting for X_{Ds} and using the unperturbed current solutions gives us (4.10) and (4.11):

$$I'_{ed} = \left(1 + \frac{{M_{De}}^2}{6}\, (2z_e + 1)\right) I_{ed} \tag{A.24}$$

$$I'_{id} = \left(1 + \frac{{M_{Di}}^2}{6} \left(\frac{z_i - 1}{z_i + 1}\right)\right) I_{id} \tag{A.25}$$

Finally, recalling that the conditions satisfying the weak-field limit imply that $M_{De} \ll 1$, $z_e \sim 1$, $M_{Di} \gg 1$, and $z_i \gg 1$ reduces the expressions for the currents to their final forms:

$$I'_{ed} \approx I_{ed} \tag{A.26}$$

$$I'_{id} \approx \left(1 + \frac{{M_{Di}}^2}{6}\right) I_{id} \tag{A.27}$$

Appendix B

Simulation Code

This appendix includes a version of the simulation code described in Chapter 6. The code was originally written for Wolfram Mathematica, however the underlying modelling could be adapted to other programming languages.

SIMULATION OF AN IRREGULAR PARTICLE

GENERATING PARTICLE

```
SetDirectory[NotebookDirectory[]];

Table[
  conds = Import["Irregular_InitialConditions.txt", "TSV"][[TRIAL + 1]]; (* IMPORTING AND ASSIGNING INITIAL CONDITIONS FROM GENERATED LIST *)
  {ro, zio, zeq, viz, θi, Ωi} = {conds[[2 ;; 4]], conds[[5]], conds[[6]], conds[[7]], conds[[8 ;; 10]], conds[[11 ;; 13]]};
  R[{α_, β_, γ_}] = N[RollPitchYawMatrix[{α, β, γ}, {1, 2, 3}]]; (* ROTATIONAL TRANSFORM FUNCTION *)
  S = ShellRegion[ImplicitRegion[x^2 / ro[[1]]^2 + y^2 / ro[[2]]^2 + z^2 / ro[[3]]^2 == 1, {x, y, z}], (Total[ro]) / 3000]; (* DEFINES DUST SURFACE *)
  No = 500; (* NUMBER OF POINTS TO SIMULATE *)
  eo = 1*^-6 * RandomPoint[S, No]; (* CREATES SURFACE OF RANDOMLY DISTRIBUTED POINTS *)
  ro = ro * 1*^-6;
  w = 1.6075;
  SA = 4 π ((ro[[1]]^w ro[[2]]^w + ro[[2]]^w ro[[3]]^w + ro[[3]]^w ro[[1]]^w) / 3)^(1 / w); (* APPROXIMATING SURFACE AREA OF PARTICLE *)
  {k1, k2, k3} = {ro[[1]] / ro[[2]], ro[[2]] / ro[[3]], ro[[3]] / ro[[1]]};
  n[{x_, y_, z_}] = {x / Sqrt[x^2 + k1^4 y^2 + k3^-4 z^2], y / Sqrt[k1^-4 x^2 + y^2 + k2^4 z^2], z / Sqrt[k3^4 x^2 + k2^-4 y^2 + z^2]};
  no = Table[n[eo[[i]]], {i, 1, No}]; (* CREATES A LIST OF NORMAL VECTORS FOR THE SURFACE *)

  (***************** FIELDS AND PARAMETERS ********************)

  (*** CREATION OF SMOOTH, INTERPOLATED FUNCTIONS FROM PIECEWISE FITS USED IN PROBE ANALYSIS ***)
  efunc[z_] = Interpolation[Table[{z, -Piecewise[{
          {220.23608 (100 z + 0.87009878)^2 - 39.935225 (100 z + 0.87009878) + 220.23608, z ≤ -0.0087009878},
          {-39.935225 (100 z + 0.87009878) + 220.23608, z > -0.0087009878}}]},
      {z, -0.05, 0.05, 0.0005}], InterpolationOrder → 3][z];
  nifunc[z_] = Interpolation[Table[{z, Piecewise[{
         {1*^15 * 0.062506876 (ArcTan[2.5872337 (100 z + 1.6089512)] + π / 2), z ≤ -0.016089512},
         {1*^15 * 0.062506876 (2.5872337 (100 z + 1.6089512) + π / 2), z > -0.016089512}}]},
      {z, -0.05, 0.05, 0.0005}], InterpolationOrder → 3][z];
  tefunc[z_] = 1.8708798 + 2.4909803 z; (* Electron temperature in eV for position in m*)
  eafunc[z_] = -tefunc[z] * D[nifunc[z], z] / nifunc[z];

  (*** DECLARATION OF FUNDAMENTAL CONSTANTS AND PLASMA PARAMETERS ***)
  qe = 1.6*^-19; (* ELECTRON CHARGE *)
  εo = 8.854*^-12; (* VACCUUM PERMITIVITY *)
  ti = 0.025; (* ION TEMPERATURE (eV) *)
  mi = 6.6335*^-26; (* ARGON ATOM MASS *)
  nn = 4*^21; (* NEUTRAL GAS NUMBER DENSITY FOR 120 mTORR *)
  ρn = mi * nn; (* NEUTRAL GAS MASS DENSITY *)
  vti = Sqrt[qe ti / mi]; (* ION THERMAL VELOCITY *)
  vtiav = Sqrt[8 / π] * vti; (* AVERAGE ION THERMAL SPEED *)
  μo = .146; (* MOBILITY CONSTANT *)
  pop = 8.313; (* PRESSURE CONSTANT *)
  ρd = 4720; (* DENSITY OF LaB6 *)
  md = ρd (4 π / 3) ro[[1]] × ro[[2]] × ro[[3]]; (* DUST MASS *)
  r0 = (ro[[1]] × ro[[2]] × ro[[3]])^(1 / 3);
  Fg = md (-9.81); (* GRAVITATIONAL FORCE ON DUST *)
  Qo = Floor[(md 9.81) / (qe efunc[zeq]), 100] qe; (* ~Qo *)
  Σr2 = Total[Table[eo[[j]].eo[[j]], {j, 1, No}]]; (* DISCRETE SUM OF R^2 *)
  {I1, I2, I3} = {0.2 md (ro[[2]]^2 + ro[[3]]^2), 0.2 md (ro[[3]]^2 + ro[[1]]^2), 0.2 md (ro[[1]]^2 + ro[[2]]^2)};
  Io = {{I1, 0, 0}, {0, I2, 0}, {0, 0, I3}};
  Jo = Transpose[N[Inverse[Io]]];
```

```
(****************** SIMULATION ********************)
uvi = 2;
UVTEST = {"off", "on"}; (* WHETHER UV CONDITION IS ON OR OFF *)
δt = 0.01; (* TIME STEP - 4 ms *)
Lt = 2400; (* TOTAL ITERATIONS - 6000 - 24 s - 5s to settle, 19 pulses to track *)
LT = 1 / δt; (* PERIOD LENGTH *)
tpulse = 0.25; (* OFFSET START OF PULSE BY 0.25 SECONDS (FULLY OFF), SETTLING TIME, TRIAL WILL COVER 100 PULSES *)
fpulse = 0.5;
δo = 1;
tRC = 0.1; (* RC-LIKE TIME FOR UV SOURCE *)
Qi = Qo; (* DUST CHARGE *)
xi = zio; (* INITIAL POSITION *)
θi = θi; (* INITIAL ORIENTATION (ROLL(x), PITCH(y), YAW(z) *)
vi = viz; (* INITIAL VELOCITY *)
Ωi = Ωi; (* INITIAL ANGULAR VELOCITY *)
Ω0 = Ωi; (* BACKGROUND ANGULAR VELOCITY *)
t = 0;

zlist = N[ConstantArray[0, {Lt, 2}]]; (* TRACK VERTICAL POSITION VS TIME *)
perzlist = N[ConstantArray[0, {Lt, 2}]]; (* TRACK VERTICAL POSITION VS PER TIME *)
vlist = N[ConstantArray[0, {Lt, 2}]]; (* TRACK VERTICAL VELOCITY VS TIME *)
phaselist = N[ConstantArray[0, {Lt, 2}]]; (* TRACK VERTICAL VELOCITY VS VERTICAL POSITION *)
Axlist = N[ConstantArray[0, {Lt, 2}]]; (* TRACK X-AXIS AREA PROJECTION VS TIME *)
Azlist = N[ConstantArray[0, {Lt, 2}]]; (* TRACK Z-AXIS AREA PROJECTION VS TIME *)
Qlist = N[ConstantArray[0, {Lt, 2}]]; (* TRACK CHARGE VS TIME *)

Table[
 (*** BASIC PARAMETERS ***)
 ni = N[nifunc[xi]]; (* ION NUMBER DENSITY *)
 te = N[tefunc[xi]]; (* ELECTRON TEMPERATURE *)
 Eo = N[efunc[xi]]; (* SPACE POTENTIAL ELECTRIC FIELD *)
 Ea = N[eafunc[xi]]; (* AMBIPOLAR ELECTRIC FIELD *)

 (*** STEP 1 - EVALUATE CENTROIDS AND PROJECTED AREAS ***)
 Ro = N[R[θi]];
 Roi = N[Inverse[Ro]];
 Rt = N[Transpose[Ro]];
 {er, nr} = N[{Table[Ro.eo[[i]], {i, 1, No}], Table[Ro.no[[i]], {i, 1, No}]}];
 dot = Table[{1, 0, 0}.nr[[i]], {i, 1, No}]; (* DOT PRODUCTS BETWEEN SURFACE NORMALS OF ROTATED SPHEROID AND UV VECTOR *)
 projlist = Table[{er[[i, 1]], er[[i, 2]], er[[i, 3]], dot[[i]]}, {i, 1, No}]; (* COMBINED SPHEROID COORDINATES AND DOT PRODUCTS FOR SORTING *)
 splitlist = Select[projlist, #[[4]] < 0 &]; (* SPLITS ABOVE LIST INTO COORDINATES OF SURFACE POINTS FACING RELEVANT VECTOR *)
 scale = Abs[Mean[splitlist[[All, 4]]]]; (* AVERAGE DOT PRODUCT OF SIDE FACING UV *)
 rc = Mean[Drop[splitlist, None, {4}]]; (* CENTROID POSITIONS FOR EACH AREA SECTION *)
 rc = {rc, -rc};
 AX = 1*^-12 * Area[ConvexHullMesh[1*^6 * er[[All, {2, 3}]]]]; (* FLUX SURFACES FOR UV ILLUMINATION *)
 AZ = 1*^-12 * Area[ConvexHullMesh[1*^6 * er[[All, {1, 2}]]]]; (* FLUX SURFACES FOR NEUTRAL, ION DRAG *)

 (*** STEP 2 - EVALUATE PLASMA PARAMETERS, FORCES, AND TORQUES AT CURRENT POSITION ***)

 (** SECONDARY PARAMETERS **)
 ρi = mi ni; (* ION MASS DENSITY *)
 λde = N[Sqrt[(εo qe te) / (ni qe^2)]]; (* ELECTRON DEBYE LENGTH *)
 μi = N[μo * pop / Sqrt[1 + 0.002188 * Sqrt[Eo^2 + Ea^2]]]; (* ION MOBILITY *)
 vdi = N[μi Ea]; (* ION DRIFT VELOCITY *)
 Mdi = N[vdi / vti]; (* ION DRIFT THERMAL MACH NUMBER *)
 Mti = N[Sqrt[Mdi^2 + 8 / π]]; (* AVERAGE THERMAL MACH NUMBER *)
 zi = N[Abs[Qi / (4 π εo r0 ti)]]; (* RATIO OF ELECTROSTATIC POTENTIAL ENERGY TO ION KINETIC ENERGY *)
 b90 = N[r0 zi / Mti^2]; (* IMPACT PARAMETER *)
 bc = N[r0 Sqrt[1 + 2 zi / Mti^2]]; (* IMPACT PARAMETER *)
 G = N[(2 (zi / (Mdi^2)) (Erf[Abs[Mdi] / Sqrt[2]] - Sqrt[2 / π] Abs[Mdi] Exp[-(Mdi^2) / 2]))]; (* KHRAPAK, COULOMB COLLISION TERM *)
 H = N[(Sqrt[2 / π]) Abs[Mdi] (Mdi^2 + 1 + 2 zi) Exp[-(Mdi^2) / 2] + (((Mdi^2)^2 + 2 (Mdi^2) - 1 - 2 (1 - (Mdi^2)) zi) Erf[Abs[Mdi] / Sqrt[2]]) / (Mdi^2)];
 (* HUTCHINSON, COLLECTION TERM *)
 lnΛHK = N[Log[(b90 + Sqrt[λde^2 / (1 + 2 / Mti^2) + r0^2]) / (b90 + r0)]]; (* COULOMB LOGARITHM *)
```

```
(** EVALUATE NEW CHARGE **)
δ = If[UVTEST[[uvi]] == "off", 0, δo (0.5 ((2 / π) ArcTan[Sin[2 π (t - tpulse)] / fpulse] + 1))]; (* DISCHARGE FUNCTION, SIMPLIFIED, f = 1 kHz *)
δ = If[UVTEST[[uvi]] == "off", 0,
  δo Piecewise[{
     {(1 - Exp[-Mod[t, 1] / tRC]) / (1 - Exp[-0.5 / tRC]), Mod[t, 1] < 0.5},
     {(1 - Exp[(1 - Mod[t, 1]) / tRC]) / (1 - Exp[0.5 / tRC]), Mod[t, 1] ≥ 0.5}
    }]]; (* DISCHARGE FUNCTION, RC-LIKE *)
Q1 = 0.5 Qo (1 - 2 δ * AX / SA);
Q2 = 0.5 Qo;
Qi = Q1 + Q2;

(** FORCES, TORQUES, DYNAMICS **)
Fe = Qi Eo; (* ELECTROSTATIC FORCE *)
Fnd = N[- (10) ρn * AZ * vtiav * vi]; (* NEUTRAL DRAG FORCE *)
Fid = -Abs[N[ρi * AZ * vtiav * vdi * (H + G lnΛHK)]]; (* ION DRAG FORCE *)
Fnet = N[Fg + Fe + Fnd + Fid]; (* NET FORCE *)
p = N[Q1 * rc[[1]] + Q2 * rc[[2]]]; (* ELECTRIC DIPOLE *)
τe = N[Cross[p, {0, 0, Eo}]]; (* ELECTRIC DIPOLE TORQUE *)
τnd = N[-ρn SA Σr2 vtiav Ωi]; (* NEUTRAL DRAG FORCE *)
τnet = N[τe + τnd]; (* NET TORQUE *)
(*** STEP 3 - UPDATE KINEMATIC VARIABLES ***)
ai = Fnet / md;
vi = vi + ai * δt;
xi = xi + vi * δt + 0.5 ai * δt^2;
Ω1 = N[(τe) / (ρn SA Σr2 vtiav)]; (* ANGULAR VELOCITY FROM MOBILITY LIMITING ARGUMENT W/ CROSS TERM *)
Ωi = N[Ω0 + Ω1];
θi = N[Mod[θi + Ωi * δt, 2 π]]; (* ADJUST ORIENTATION *)

(*** STEP 4 - ADD DATA OF INTEREST TO TABLES ***)
If[l > 400,
 zlist[[l]] = {t, 100 xi};
 perzlist[[l]] = {Mod[t, 1], 100 xi};
 vlist[[l]] = {t, 100 vi};
 phaselist[[l]] = {100 xi, 100 vi};
 Axlist[[l]] = {t, AX * 1*^12};
 Azlist[[l]] = {t, AZ * 1*^12};
 Qlist[[l]] = {t, Abs[Qi / qe]};
];
t = t + δt;
, {l, 1, Lt}];

AxAVG = Mean[Axlist[[All, 2]]];
AxSTD = StandardDeviation[Axlist[[All, 2]]];
AzAVG = Mean[Azlist[[All, 2]]];
AzSTD = StandardDeviation[Azlist[[All, 2]]];
QdmaxAVG = Mean[Take[Qlist[[All, 2]], {1, Lt, LT}]];
QdmaxSTD = StandardDeviation[Take[Qlist[[All, 2]], {1, Lt, LT}]];
QdminAVG = Mean[Take[Qlist[[All, 2]], {0.5 LT + 1, Lt, LT}]];
QdminSTD = StandardDeviation[Take[Qlist[[All, 2]], {0.5 LT + 1, Lt, LT}]];
stats = Import[StringJoin["Irregular_SimulationStats_UV", UVTEST[[uvi]], ".txt"], "TSV"];
stats[[TRIAL + 1]] = {TRIAL, SA * 1*^12, AxAVG, AxSTD, AzAVG, AzSTD, QdmaxAVG, QdmaxSTD, QdminAVG, QdminSTD};
Export[StringJoin["Irregular_SimulationStats_UV", UVTEST[[uvi]], ".txt"], stats, "TSV"];
Export[StringJoin["Pos Data/Irregular_PosData_UV", UVTEST[[uvi]], "_Trial=", ToString[TRIAL], ".txt"],
 Join[{{"t (s)", "z (cm)"}}, zlist], "TSV"];
Export[StringJoin["Vel Data/Irregular_VelData_UV", UVTEST[[uvi]], "_Trial=", ToString[TRIAL], ".txt"],
 Join[{{"t (s)", "vz (cm/s)"}}, vlist], "TSV"];
Export[StringJoin["VvsZ Data/Irregular_VvsZData_UV", UVTEST[[uvi]], "_Trial=", ToString[TRIAL], ".txt"],
 Join[{{"z (cm)", "vz (cm/s)"}}, Drop[Partition[Riffle[zlist[[All, 2]], vlist[[All, 2]]], 2], 4 * LT]], "TSV"];
Export[StringJoin["AreaX Data/Irregular_AreaXData_UV", UVTEST[[uvi]], "_Trial=", ToString[TRIAL], ".txt"],
 Join[{{"t (s)", "Ax (μm^2)"}}, Axlist], "TSV"];
Export[StringJoin["AreaZ Data/Irregular_AreaZData_UV", UVTEST[[uvi]], "_Trial=", ToString[TRIAL], ".txt"],
 Join[{{"t (s)", "Az (μm^2)"}}, Azlist], "TSV"];
Export[StringJoin["Qd Data/Irregular_QdData_UV", UVTEST[[uvi]], "_Trial=", ToString[TRIAL], ".txt"],
 Join[{{"t (s)", "Qd (e)"}}, Qlist], "TSV"];
, {TRIAL, 2464, 2500}];
```